

1993

Freezing problem in pipe flows

Jong Suk Lee
Iowa State University

Follow this and additional works at: <https://lib.dr.iastate.edu/rtd>

 Part of the [Mechanical Engineering Commons](#)

Recommended Citation

Lee, Jong Suk, "Freezing problem in pipe flows " (1993). *Retrospective Theses and Dissertations*. 10471.
<https://lib.dr.iastate.edu/rtd/10471>

This Dissertation is brought to you for free and open access by the Iowa State University Capstones, Theses and Dissertations at Iowa State University Digital Repository. It has been accepted for inclusion in Retrospective Theses and Dissertations by an authorized administrator of Iowa State University Digital Repository. For more information, please contact digirep@iastate.edu.

INFORMATION TO USERS

This manuscript has been reproduced from the microfilm master. UMI films the text directly from the original or copy submitted. Thus, some thesis and dissertation copies are in typewriter face, while others may be from any type of computer printer.

The quality of this reproduction is dependent upon the quality of the copy submitted. Broken or indistinct print, colored or poor quality illustrations and photographs, print bleedthrough, substandard margins, and improper alignment can adversely affect reproduction.

In the unlikely event that the author did not send UMI a complete manuscript and there are missing pages, these will be noted. Also, if unauthorized copyright material had to be removed, a note will indicate the deletion.

Oversize materials (e.g., maps, drawings, charts) are reproduced by sectioning the original, beginning at the upper left-hand corner and continuing from left to right in equal sections with small overlaps. Each original is also photographed in one exposure and is included in reduced form at the back of the book.

Photographs included in the original manuscript have been reproduced xerographically in this copy. Higher quality 6" x 9" black and white photographic prints are available for any photographs or illustrations appearing in this copy for an additional charge. Contact UMI directly to order.

U·M·I

University Microfilms International
A Bell & Howell Information Company
300 North Zeeb Road, Ann Arbor, MI 48106-1346 USA
313/761-4700 800/521-0600



Order Number 9321188

Freezing problem in pipe flows

Lee, Jong Suk, Ph.D.
Iowa State University, 1993

U·M·I
300 N. Zeeb Rd.
Ann Arbor, MI 48106



Freezing problem in pipe flows

by

Jong Suk Lee

A Dissertation Submitted to the
Graduate Faculty in Partial Fulfillment of the
Requirements for the Degree of
DOCTOR OF PHILOSOPHY

Department: Mechanical Engineering

Major: Mechanical Engineering

Approved:

Signature was redacted for privacy.

In Charge of Major Work

Signature was redacted for privacy.

For the Major Department

Signature was redacted for privacy.

For the Graduate College

Iowa State University

Ames, Iowa

1993

TABLE OF CONTENTS

NOMENCLATURE	x
1. INTRODUCTION	1
1.1 Freezing and Melting Problems	1
1.1.1 Conduction-dominated phase change – The Stefan-Neumann problem	3
1.1.2 Thermally developing flow in a pipe – The Graetz problem . .	5
1.2 Literature Review	7
1.2.1 Freezing in a pipe with fluid flow	7
1.2.2 Flow instability and ice-band structure	24
1.3 Scope of the Present Study	33
2. MATHEMATICAL ANALYSIS	35
2.1 The Physical Model	35
2.2 The Dimensional Formulation	37
2.2.1 Governing equations in primitive variables	37
2.2.2 Boundary conditions	39
2.2.3 Initial conditions	40
2.2.4 Formulation using stream function and vorticity	43
2.3 The Dimensionless Formulation	45

2.3.1	Coordinate transformation	45
2.3.2	Governing equations	47
2.3.3	Boundary conditions	48
2.3.4	Initial conditions	49
3.	NUMERICAL ANALYSIS	54
3.1	Numerical Method of Solution	54
3.1.1	Clustered grid	54
3.1.2	Finite differencing	59
3.2	Computational Procedure	63
3.3	Dimensionless Parameters	65
4.	RESULTS AND DISCUSSION	68
4.1	Results Using Fully Developed Flow Initial Condition	69
4.1.1	Time for transient freezing	69
4.1.2	Final steady-state ice layer profile	73
4.1.3	Heat transfer	78
4.2	Results Using Developing Flow Initial Condition	84
4.2.1	Initial ice layer profile	84
4.2.2	Heat transfer	91
4.2.3	Disturbances and responses	93
4.3	Effects of Internal Freezing on the Hydrodynamic Field	99
4.3.1	Pressure drop	99
4.3.2	Velocity profile	106
5.	CONCLUSIONS	109

REFERENCES	115
ACKNOWLEDGMENTS	121
APPENDIX A. INITIAL STATES	122
A.1 General Governing Equations	122
A.1.1 Dimensional formulation	122
A.1.2 Scale analysis	123
A.1.3 Dimensionless formulation	124
A.2 Fully Developed Flow Initial State	124
A.2.1 Boundary conditions	124
A.2.2 Reduced form of governing equations	126
A.2.3 Analytical solution	126
A.2.4 Numerical solution	134
A.3 Developing Flow Initial State	136
A.3.1 Boundary layer formulation for small z	137
A.3.2 Asymptotic solution for small z	139
A.3.3 Numerical solution	148
APPENDIX B. TRANSFORMATION OF COORDINATES	152
B.1 Coordinates for Solid Phase Domain	153
B.2 Core Scale Coordinates for Liquid Phase Domain	154
B.3 Boundary Layer Scale Coordinates for Liquid Phase Domain	155
B.4 Stretched Coordinates for Computational Liquid Domain	157
APPENDIX C. PRESSURE DROP	159
C.1 Dimensional Formulation	159

C.1.1	Pressure gradient	160
C.1.2	Pressure drop	162
C.2	Dimensionless Formulation	163
C.2.1	Pressure gradient	163
C.2.2	Pressure drop	164
C.2.3	Normalized pressure drop	164
C.2.4	Numerical evaluations	166

LIST OF TABLES

Table 1.1:	Numerical parameters and results of transient freezing	22
Table 1.2:	Comparison of the onset Reynolds numbers	29
Table 3.1:	Maximum and minimum increments of nonuniform grids	57
Table 3.2:	Vorticity boundary condition at the pipe wall	66
Table 4.1:	Effects of λ on freezing time and final steady state	70
Table 4.2:	Self-similar ice layer profiles: Location of 40% ice layer thickness	77
Table 4.3:	Reduction of the flow passage for the fully developed flow	78
Table 4.4:	Maximum distance and ice thickness for the initial steady state	87
Table 4.5:	Centerline velocity increases and maximum deviations from the parabolic velocity	107
Table A.1:	Dimensionless liquid temperature for the thermally fully de- veloped flow	129
Table A.2:	Initial uniform radius of solid-liquid interface	134
Table A.3:	Effect of free parameter C upon the asymptotic liquid tem- perature	144

LIST OF FIGURES

Figure 1.1:	Thermal entrance of a tube with freezing	9
Figure 1.2:	Axial velocity distributions in a tube	10
Figure 1.3:	Schematic diagram of the ice-band structure	26
Figure 2.1:	Schematic diagram of the freezing in a pipe flow	36
Figure 2.2:	Coordinate transformation: Physical and transformed domains	46
Figure 3.1:	Grid clustering near the solid-liquid interface	56
Figure 3.2:	Nonuniform grid spacings for various stretching parameter β	58
Figure 4.1:	Freezing time (t_{95}) as a function of Ste	72
Figure 4.2:	Steady-state ice layer profiles (almost linear) from the fully developed flow initial condition ($z_{max} = 0.05$)	74
Figure 4.3:	Steady-state ice layer profiles from the fully developed flow initial condition ($z_{max} = 0.5$)	76
Figure 4.4:	Average values of ice thickness and the radius of solid-liquid interface at the final steady state and the percent reduction of the flow passage radius versus Su for short pipe lengths . .	79
Figure 4.5:	Dimensionless bulk mean temperature drop for the fully de- veloped flow	81

Figure 4.6:	Comparison of Nusselt numbers for the fully developed flow . . .	83
Figure 4.7:	Initial ice layer profiles for the developing flow ($z_{max} = 0.05$)	86
Figure 4.8:	Maximum distances for the converged steady-state initial condition and the characteristic change of ice layer profiles . . .	88
Figure 4.9:	Log-log plot of the characteristic change of ice layer profiles . . .	90
Figure 4.10:	Comparison of Nusselt numbers for the developing flow . . .	92
Figure 4.11:	Comparison of bulk mean temperatures for the developing flow	94
Figure 4.12:	Forms of disturbances and an example of implementation . . .	96
Figure 4.13:	Disturbances and responses: vorticity	97
Figure 4.14:	Disturbances and responses: stream function	98
Figure 4.15:	Relation between pressure drop and average flow passage radius for short pipe lengths	100
Figure 4.16:	Pressure drop through the pipe for the final steady-state ice layer profile ($z_{max} = 0.05$)	102
Figure 4.17:	Pressure drop through the pipe for the final steady-state ice layer profile ($z_{max} = 0.5$)	103
Figure 4.18:	Normalized pressure drop versus various measures of departure of the flow passage radius	105
Figure 4.19:	Velocity profiles at different axial locations ($Su = 2.0$)	108
Figure A.1:	Dimensionless liquid temperature profile for the thermally fully developed flow	130
Figure A.2:	Initial distributions of solid and liquid temperatures for the thermally fully developed flow	133

Figure A.3: Dimensionless liquid temperature profile in the boundary layer
as $z \rightarrow 0$ 145

Figure A.4: Asymptotic growth of the thermal boundary layer and ice
layer in the axial direction for small z 146

Figure A.5: Lagrangian interpolation of the liquid temperature from bound-
ary layer scale to core scale 151

NOMENCLATURE

a	pipe radius
c	specific heat
d	neck diameter
f	$\frac{\bar{f}}{Ga^4/4\mu}$, dimensionless stream function
g	acceleration of gravity
h	convection heat transfer coefficient
h_{sl}	latent heat of fusion
Δh	head difference, head loss
k	thermal conductivity
\dot{m}	mass flow rate
nr	number of radial nodes in liquid phase
ns	number of radial nodes in solid phase
nz	number of axial nodes
q	heat flux
r	dimensionless stretched radial coordinate
\bar{r}	dimensional radius coordinate
r_b	$\frac{\bar{R}-\bar{r}}{\delta}$, dimensionless radial coordinate for boundary layer scale
r_c	$\frac{\bar{r}}{R}$, dimensionless radial coordinate for core scale

r_s	$\frac{a-\bar{r}}{\epsilon}$, dimensionless radial coordinate for solid layer
t	$\frac{\bar{t}}{a^2/\alpha_s}$, dimensionless time
\bar{u}	radial velocity
\bar{w}	axial velocity
z	$\frac{\bar{z}}{aPe}$, dimensionless axial coordinate
z_{tr}	dimensionless transition point from small z to large z solution
B	$R\delta$, variable defined for boundary layer formulation
Bi	Biot number
C	free parameter in boundary layer thickness; constant
D	pipe diameter
F	$\frac{1}{R^2} \frac{\partial^2 f}{\partial r_c^2}$, variable defined for dimensionless pressure gradient
G	$\frac{8\nu\dot{m}}{\pi a^4}$, uniform pressure gradient
Gz	$\frac{Wc}{kL}$, Graetz number
J	transformation Jacobian
K	$\frac{k_l}{k_s}$, thermal conductivity ratio
L	pipe length
M, N	second order differential operators
Nu	Nusselt number
P	dimensionless pressure
ΔP	$\frac{\Delta \bar{P}}{GaPe/8}$, dimensionless pressure drop
ΔP_n	$\frac{\Delta \bar{P}}{G\bar{z}_{max}/R^*4}$, normalized pressure drop
Pe	$\frac{Ga^3}{4\mu\alpha_l}$, Peclet number
Pr	$\frac{\nu}{\alpha_l}$, Prandtl number

Q	$\frac{\dot{m}}{\rho}$, volume flow rate
R	$\frac{\bar{R}}{a}$, dimensionless radius of solid-liquid interface
R_o	initial uniform radius of solid-liquid interface , dimensionless
R^*	average radius of solid-liquid interface , dimensionless
Ra	$\frac{\beta g \Delta T D^3}{\mu \alpha}$, Rayleigh number
Re	$\frac{VD}{\mu}$, Reynolds number
ΔR	amount of reduction in the flow passage radius, dimensionless
ΔR^*	standard deviation of the flow passage radius, dimensionless
Sb	subcooling number
Ste	$\frac{c_s(T_o - T_{wo})}{h_{sl}}$, Stefan number
Su	$\frac{k_l (T_{io} - T_o)}{k_s (T_o - T_{wo})}$, superheat number
T^*	$\frac{\bar{T}_l - T_o}{T_m - T_o}$, dimensionless self-similar liquid temperature
T_c	coolant temperature
T_i	inlet water temperature
T_l	$\frac{\bar{T}_l - T_o}{T_{io} - T_o}$, dimensionless liquid temperature
T_m	$\frac{\bar{T}_m - T_o}{T_{io} - T_o}$, dimensionless bulk mean temperature
T_o	freezing temperature
T_s	$\frac{\bar{T}_s - T_{wo}}{T_o - T_{wo}}$, dimensionless solid temperature
T_w	pipe wall temperature
V	velocity
X, Y	metrics for the coordinate transformation
Z	$z - z_{tr}$, new dimensionless axial coordinate

Greek symbols

α	$\frac{k}{\rho c}$, thermal diffusivity
β	coefficient of thermal expansion; stretching parameter
δ	$\frac{\bar{\delta}}{R}$, dimensionless thermal boundary layer thickness
ϵ	$\frac{\bar{\epsilon}}{a}$, dimensionless ice layer thickness
ϵ^*	average dimensionless ice layer thickness
θ	$\frac{T_o - T_c}{T_i - T_o}$, temperature ratio
λ	$\frac{\alpha_l}{\alpha_s}$, thermal diffusivity ratio
μ	viscosity
ν	$\frac{\mu}{\rho}$, kinetic viscosity
ρ	density
ϕ	dummy variable
ω	$\frac{\bar{\omega}}{Ga/4\mu}$, dimensionless vorticity
Γ	$\frac{1}{R^2} \frac{\partial^2 F}{\partial r_c^2}$, variable defined for dimensionless pressure drop
Δ	$\frac{\rho_l}{\rho_s}$, density ratio

Subscripts

a	asymptotic solution for small z
bl	boundary layer region
co	core region
f	final; freezing
i	radial node index
j	axial node index

<i>l</i>	liquid phase
<i>m</i>	average, bulk mean
<i>max</i>	maximum
<i>o</i>	inlet; asymptotic initial condition for the fully developed flow
<i>s</i>	solid phase
<i>w</i>	pipe wall
<i>z</i>	local
∞	far downstream or free stream

Superscripts

-	dimensional variable
-	vector notation
.	$\frac{\partial}{\partial t}$ or $\frac{\partial}{\partial t}$, time derivative
'	$\frac{\partial}{\partial z}$ or $\frac{\partial}{\partial \bar{z}}$, first-order axial derivative
''	$\frac{\partial^2}{\partial z^2}$ or $\frac{\partial^2}{\partial \bar{z}^2}$, second-order axial derivative
+	limiting solution as $z \rightarrow 0$
<i>k</i>	iteration number
<i>n</i>	time level

1. INTRODUCTION

1.1 Freezing and Melting Problems

Freezing and melting problems take place commonly in a wide variety of processes and situations which involve water-freezing or ice-melting, casting of metals, freezing and thawing of foods, etc. While the freezing phenomenon is utilized in such ways, it is not always desirable. Frost formation on refrigeration coils or airplane wings, ice formation in water mains, and freezing of liquid metals in heat exchangers and associated piping, for example, have detrimental effects.

Basically, these problems with change of phase have in common a characteristic nonlinearity resulting from the moving boundary (solid-liquid interface), which complicates their analyses. Furthermore, several factors add to the complexity of the mathematical treatments. General solutions need a three-dimensional, transient analysis of the temperature distribution before, during, and after the change of phase in a body, whose physical properties are frequently temperature-dependent. In addition, sometimes complicated and often perplexing physical phenomena such as dendritic ice formation, supercooling, etc. take place in the freezing or melting process which invalidate conventional, general analyses [1].

The study on freezing and melting problems started more than a century ago. In 1891, a theory of the freezing of a liquid layer was set forth by Stefan to account

for observations made on the formation of sea ice. This pioneering work has become a standard reference in modern studies of freezing and melting problems, although it might be noted that it was not the first. A quite similar formulation was presented in 1831 by Lamé and Clapeyron for predicting freezing rates in moist soil. The first exact solution was obtained by Neumann and was presented in his lectures in the 1860's, which were not published until 1912 [2], however.

Since then, a great number of investigations dealing with the analytical, experimental, and numerical aspects of particular problems have been published. Extensive summaries of these literature have been compiled by Bankoff [3], Muehlbauer and Sunderland [4], Crank [5], Cheung and Epstein [6], and most recently by Yao and Prusa [2]. Some of these literature that relate to the present study are reviewed in the following section.

This study deals with the freezing of a liquid in pipe flows due to the step change in the pipe wall temperature along the test section. Mathematically this problem may have both spatial and temporal singularities. The spatial singularity occurs for an ice-free pipe whenever there is a step-change in the pipe wall temperature – then a thermal boundary layer starts to grow from zero thickness. The temporal singularity occurs due to the sudden appearance or disappearance of ice. These singularities may be understood individually by considering the limiting cases of the problem. When there is no fluid flow, the problem is reduced to a one-dimensional freezing problem, which is known as the Stefan-Neumann problem. When there is no freezing and there is a step-change in wall temperature, the problem is reduced to a thermally developing flow in a pipe, known as the Graetz problem. These two limiting problems, which are very relevant to the present study, will be addressed briefly.

1.1.1 Conduction-dominated phase change – The Stefan-Neumann problem

Stefan and Neumann independently solved the one-dimensional phase-change problems with isothermal boundary conditions. Three partial differential equations were required to be solved simultaneously: the heat diffusion equations for the solid and liquid phase-change material (PCM) and an equation derived from an energy balance at the solid-liquid interface. They solved this problem analytically and obtained the exact solutions. They determined that, for the case of isothermal cooling, the position of the solid-liquid interface varied as the square root of time. Even though Neumann's work was earlier, it was Stefan's contribution that was first recognized and that first developed a general awareness of phase-change problems. Phase-change problems have since been named "Stefan problems" in his honor. Since moving boundaries are the outstanding feature of phase-change problems, various other moving-boundary problems are frequently also referred to as Stefan problems [7] or "Stefan-like problems" [8]. In order to properly recognize Neumann's contribution, in this work the analytic one-dimensional, two phase, conduction-dominated problem will be referred to as the Stefan-Neumann problem.

Since these pioneering efforts of the previous century, a tremendous amount of work has occurred on Stefan problems. A large number of techniques have been developed in order to attack a wide variety of problems that are variations and generalizations of the elementary problems analyzed by these first investigators. Among some of the earlier researchers after them, Pekeris and Slichter [9] derived an approximate solution for the rate of ice formation on a long cylinder, and London and Seban [10] presented the general approximate method to solve ice formation at spherical,

cylindrical, and plane boundaries. Unfortunately, no single method appears to work best in all classes of problems [2].

Stefan problems in general have a few undesirable mathematical characteristics. First, they are nonlinear in nature in that the position of the solid-liquid interface is unknown *a priori* and must be determined as part of the solution. Secondly, they are singular whenever a phase suddenly appears or disappears. The nonlinearity and singularity of Stefan-Neumann problems together make these problems intrinsically difficult to solve. Even numerical methods that work well on many nonlinear problems often perform quite poorly on Stefan problems. Most often, the best method for solving a Stefan problem is a combination of analytical and numerical solutions [2].

Four dimensionless parameters appear in the Stefan-Neumann problem: Ste , Su (or Sb), λ , and Δ . The effects of these parameters are generally coupled with one another, however, the main effect of each parameter may be outlined briefly as followings. Ste (Stefan number), the ratio of the available sensible cooling (or heating) to the latent heat, is the most important factor in determining the rate of freezing or melting. Su (superheat number), the ratio of the sensible heating of liquid PCM to the sensible cooling of the liquid PCM, appears in a freezing problem, (whereas Sb , subcooling number, the ratio of the sensible cooling of solid PCM to the sensible heating of the liquid PCM, appears in a melting problem). Superheating means that the liquid is initially above the freezing temperature, (whereas subcooling means that the solid is initially below the melting temperature). If the system under study reaches a steady state other than complete freezing or melting, Su (or Sb) determines the amounts of solidification (or melting) at the steady state. λ is the ratio of thermal diffusivities of the two phases, and it generally enhances or diminishes

the effect of superheating (or subcooling). Δ is the ratio of densities of the two phases, and it has the effect of blowing or suction at the solid-liquid interface, hence enhancing or diminishing the rate of freezing (or melting). For a melting problem, the effects of subcooling and density change upon phase change can be found in literature [11, 12]. In summary of [11, 12], subcooling effects can be quite significant while those due to density change are negligible. The similarity between freezing and melting problems indicates that the effects of Su are important while those of Δ are unimportant in a freezing problem.

1.1.2 Thermally developing flow in a pipe – The Graetz problem

The study of heat transfer in laminar flow through a closed conduit was first made by Graetz in 1883 and independently by Nusselt in 1910 [13]. They considered an incompressible fluid flowing through a circular tube, with constant physical properties, having a fully developed laminar velocity profile and a developing temperature profile. The tube was maintained at a constant and uniform temperature different from the uniform temperature of the fluid at the entrance. Using these simplifying assumptions, this problem is reduced to a single liquid energy equation subject to initial and boundary conditions. This problem is now well-known as the “Graetz problem” but is sometimes also referred to as the “Graetz-Nusselt problem”. If the duct in study is not a circular tube, the problem is usually characterized as the “Graetz-type problem” [13].

The closed-form solution to the Graetz problem has been obtained primarily by two methods: the Graetz method and the Leveque method. The Graetz method uses the separation of variables technique, and as a result, the governing differential

equation is reduced to the Sturm-Liouville type. The solution is then obtained in the form of an infinite series expansion in terms of eigenvalues and eigenfunctions. This method has an unattractive feature in that the number of terms required for a desired accuracy increases sharply as the entrance is approached. Even the first 121 terms of the series are insufficient to accurately determine the Graetz solution for $z < 10^{-4}$. The Leveque method uses a similarity transformation technique to alleviate this difficulty. Leveque employed the “flat plate” solution as an asymptotic approximation near the duct entrance, where the series solution does not converge. The Leveque solution is valid only near the entrance, leading to significant errors far from $z = 0$. The Leveque method has been extended by a perturbation analysis to obtain an accurate solution for intermediate values of z . Shah [14] obtained a complete analytical solution for the Graetz problem, using the extended Leveque solution for $z \leq 10^{-4}$ and using the first 121 terms of the Graetz series for $z > 10^{-4}$. Nusselt numbers from the Graetz solution and the Leveque solution are identical up to five or more digits for $0.00002 < z < 0.005$ [13].

The Graetz problem is one of the fundamental problems for internal flow convection heat transfer. In addition to its great practical importance, it has induced many applied mathematicians to apply and test different mathematical methods and approaches to solve the same problem. The first numerical solution for the Graetz problem was reported by Kays [15] in 1955. Since then, many numerical solutions have been presented, and most of them have employed finite-difference methods. In general, numerical solutions have not given accurate results for Nusselt number in the entrance region of closed conduits. This is due to the fact that there exists a singularity at the duct entrance and most numerical solutions fail to accurately resolve

the sharp thermal gradients at the wall. Even the usual remedy of refining the axial and radial grid sizes near the entrance and near the duct wall may not yield accurate solutions.

Recently, Manglik and Prusa [16] presented a method of obtaining accurate numerical solutions for Graetz-type problems. Their key to an accurate solution was an understanding of the asymptotic nature of such problems. They rescaled the governing equations in order to bring out the singularity at the duct entrance and obtained a nonsingular form. The resulting equations were readily amenable to numerical solution by finite difference method. They employed two different length scales, one for the boundary-layer flow and another for the core flow. They used the boundary layer formulation in the entrance region close to $z = 0$ and the core formulation for far downstream. They matched two solutions at a region where the boundary layer thickness was of the same order of magnitude as the duct radius to provide the complete heat transfer solution to the Graetz problem. More recently, Prusa and Manglik [17] extended their technique to solutions for thermally developing flows of Newtonian and non-Newtonian fluids in circular tubes with uniform wall temperature. The strategic technique that they used in handling the singularity at the duct entrance has been employed in the present study. In particular, the Graetz problem has been solved as a part of the developing flow initial condition.

1.2 Literature Review

1.2.1 Freezing in a pipe with fluid flow

1.2.1.1 Framework of the analysis In 1968, Zerkle and Sunderland [18] published a paper which has served as the foundation of most analyses of freezing

in channel flows. They presented a theoretical analysis and experimental results for the study on the effects of a liquid-solid change of phase at the inner surface of a circular tube upon heat transfer and pressure drop. The schematic diagram of their analytical model is shown in Figure 1.1 and consists of the steady laminar flow of a liquid with constant physical properties through a tube of inside radius R . The flow first passes through a solidification-free zone, $z < 0$, where the tube wall temperature is maintained constant (T_i) and above the freezing temperature (T_0). In this region, the flow is at a uniform temperature (T_i), and the axial velocity profile is parabolic. At $z = 0$, the wall temperature undergoes a step reduction in temperature to a value T_w , which is below the freezing temperature. Beyond this location, the liquid is cooled as it flows through the tube by heat transfer to the frozen layer. Its mean temperature decreases toward the freezing temperature, and the thickness of the solid layer increases. In their analytical investigation, Zerkle and Sunderland employed the following assumptions: steady-state conditions prevail; the liquid is Newtonian and incompressible; axial heat conduction, viscous energy dissipation, radiant heat transfer, and natural convection are negligible; the temperature at the solid-liquid interface is constant and equal to the freezing temperature; and the solid-phase shell is smooth, homogeneous, and isotropic and has a monotonically increasing thickness beginning at the thermal entrance.

In their analysis, a parabolic velocity profile was employed throughout the cooling region. This assumption was based upon two effects. First, when a liquid is cooled as it flows through a tube, the velocity near the wall tends to decrease while the velocity in the central region increases. This effect produces an axial velocity profile of the form presented by curve A in Figure 1.2 and arises from the fact that

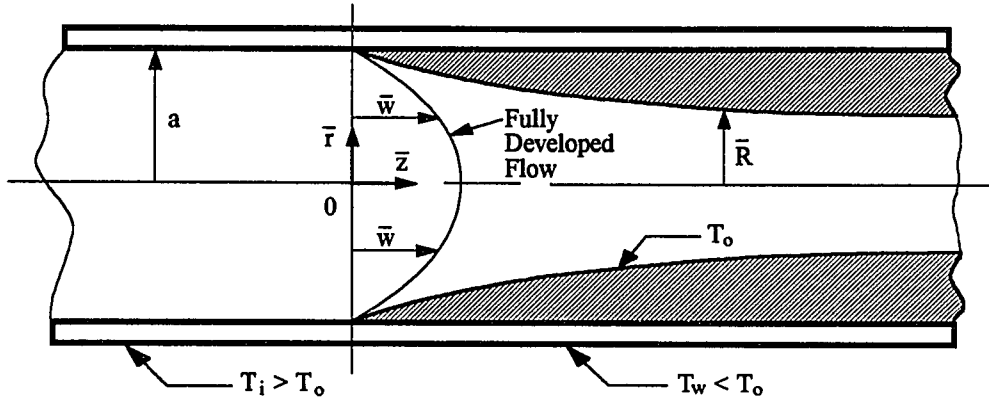


Figure 1.1: Thermal entrance of a tube with freezing

liquids are more viscous at lower temperatures [19]. Secondly, the axial velocity profile of a fluid flowing through a tube of decreasing diameter is flatter than a parabolic profile. This effect produces the profile presented by curve B. They assumed that the combination of these effects was sufficiently negligible or that they might even cancel one another. As a result, the axial velocity profile was assumed to remain parabolic, presented by curve C.

Using the parabolic velocity distribution, dimensionless variables, and transformation of radial coordinate, Zerkle and Sunderland reduced the liquid energy equation to the classical Graetz problem, which describes the temperature profiles in a pipe flow in the absence of a frozen shell along the pipe wall. The temperature distribution was expressed by an infinite series given by Sellars *et al.* [20]. Once the interface temperature gradient in the liquid was determined, the radial location of the frozen layer was obtained from the one-dimensional temperature distribution in the frozen crust combined with an energy balance at the solid-liquid interface. The

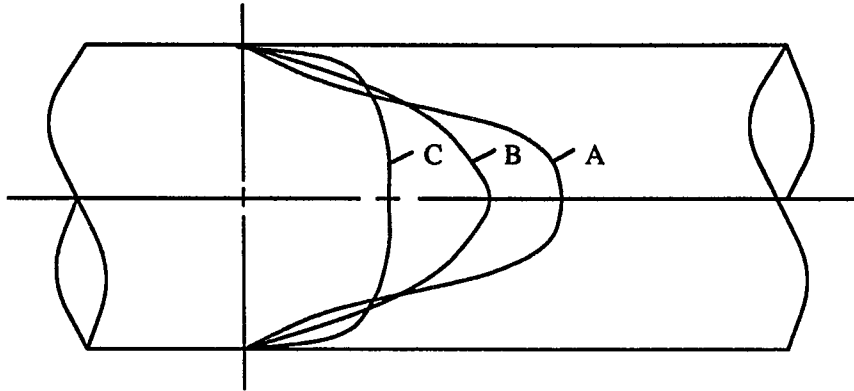


Figure 1.2: Axial velocity distributions in a tube

pressure drop was then obtained from an integrated form of the axial momentum equation. Zerkle and Sunderland's theoretical work was accompanied by two separate experiments. The first involved the visual observation of a liquid-to-solid change of phase with flow through a rectangular duct. The second experiment involved the measurement of pressure drop and rate of heat transfer with flow through a circular tube so that a comparison could be made between experimental and theoretical results.

By the observation of the ice crust that formed along the wall, Zerkle and Sunderland confirmed the validity of their model in that the ice crust gradually increased in thickness with axial distance, starting from zero thickness at the frozen-section inlet. Then, they compared the experimental heat transfer rates and pressure drops with theoretical predictions. The comparison revealed a considerable variance between theoretical predictions and experimental results. In general, experimental heat transfer rate and pressure drop were both greater than the predicted values. They

attributed this primarily to the effect of natural convection, which was not included in their theoretical analysis. They discussed the effect of natural convection upon the thickness of the ice layer using an equation

$$R^{Su} = \exp\left(\frac{-2}{\frac{dq}{dz}}\right) \quad (1.1)$$

where R is the radius of the solid-liquid interface and q is the dimensionless rate of heat transfer from the liquid for the given tube length. Near the thermal entrance, natural convection caused heat transfer to be greater than the theoretical prediction. Therefore, the heat transfer gradient and the radius of the solid-liquid interface were also greater than the theoretical prediction. Thus the overall effect of natural convection upon the ice layer made it thinner at small z than the theoretical predictions. Farther along the tube, however, natural convection became reduced due to the constriction of the flow area by the ice layer and the resultant fluid acceleration, and a position was reached where the heat transfer gradient was less than the theoretical prediction. Beyond this position, the radius of the solid-liquid interface was less than the theoretical result, which indicates that the thickness of the ice layer predicted by their theoretical model was low at large z .

Zerkle and Sunderland indicated that the ice layer profile could be determined through the use of Equation (1.1) if the heat transfer from a tube with internal freezing could be predicted or closely approximated. Since the theoretical solution for combined forced and natural convection was extremely difficult to obtain, they developed a semi-empirical method for obtaining solutions that accounted approximately for the effect of natural convection. As a method of solution, they approximated the heat transfer rate by empirical results for fluid flow without freezing. They employed

an empirical equation obtained by Oliver [21] for laminar, fully developed flow entering a horizontal circular tube. They concluded by carrying out a semi-empirical solution for a hypothetical problem in order to illustrate how natural convection affects the ice layer profile.

Oliver [21] presented experimental results about the effect of natural convection on heat transfer in horizontal tubes. Observing the variation of his results from previously predicted effects, he showed that when the group (RaD/L) was taken as the factor controlling natural convection, the information obtained in tubes of different dimensions was inconsistent. He found that better agreement was obtained when the ratio D/L was omitted from the group and further improvement resulted from the incorporation of the ratio L/D . He showed that all the data were adequately (within $\pm 20\%$) represented by the equation

$$Nu \left(\frac{\mu_w}{\mu_B} \right)^{0.14} = 1.75 \left(Gz + 5.6 \cdot 10^{-4} (Ra L/D)^{0.70} \right)^{1/3} \quad (1.2)$$

with the dimensionless groups defined as

$$Nu = \frac{hD}{k} \quad Gz = \frac{Wc}{kL} \quad Ra = \frac{\beta g \Delta T D^3}{\mu_B \alpha}$$

where the subscripts w and B refer to the tube wall temperature and the average bulk mean temperature, respectively. k , β , and α are thermal conductivity, coefficient of expansion, and thermal diffusivity of fluid measured at mean temperature, respectively. W appearing in the definition of Gz is the mass flow rate, denoted by \dot{m} in this study. ΔT is the temperature difference giving rise to natural convection. He mentioned that this equation became inaccurate when $Gz < \pi Nu$ and the power of L/D was only provisional.

1.2.1.2 Steady-state analysis Experimental studies of freezing on thermal entrance region laminar flow were also carried out by Depew and Zenter [22], Mulligan and Jones [23], and Hwang and Sheu [24]. The experimental systems used by these workers were similar to that of Zerkle and Sunderland [18], although the experiments were conducted under conditions of higher tube-wall temperatures and with tubes of smaller inside diameter. The inside diameters of the tubes were 2.00 cm (Depew and Zenter), 1.42 cm (Mulligan and Jones), and 0.95 cm (Hwang and Sheu), respectively, whereas that of Zerkle and Sunderland was 3.75 cm.

Depew and Zenter [22] did essentially the same experiments as those of Zerkle and Sunderland. They compared their experimental dimensionless heat transfer rate data with those of Zerkle and Sunderland and the Graetz solution on a semi-log plot versus dimensionless axial location. All of the experimental results were considerably above the Graetz solution. This was due to the effect of natural convection as had been pointed out by Zerkle and Sunderland. Moreover, their experimental data were plotted roughly in between the Graetz solution and Zerkle and Sunderland's results, which indicates that the effect of natural convection is less in a smaller diameter pipe. Depew and Zenter examined the applicability of the Oliver's correlation [21], Equation (1.2), by comparing the Nusselt number data measured by themselves and Zerkle and Sunderland and predicted by the equation. They observed that Oliver's correlation underestimated heat transfer when $L/D < 50$. Also they found that pressure drop was extremely sensitive to wall temperature and considerable variation might result from only negligible temperature changes.

Mulligan and Jones [23] also compared their experimental results with Oliver's correlation, which was previously used by Zerkle and Sunderland in their semi-

empirical analysis [18]. Mulligan and Jones showed that Oliver's correlation was applicable when tube length-diameter ratio was significantly greater than 50 and that the correlation very accurately predicted the Nusselt number for the case of flow with an internal frozen layer when it was formulated with actual internal dimensions. They also suggested that a parabolic velocity profile should not be used in the analytical prediction of pressure drop in the range where natural convection effects were significant. They conjectured that the underestimate in this procedure was of the order of the overestimate in neglecting natural convection effects altogether. Their conjecture was based on the observation that the experimental data agreed well with the theory of Zerkle and Sunderland wherein both assumptions were made.

Hwang and Sheu [24] presented a theoretical and experimental investigation of liquid solidification in the combined hydrodynamic and thermal entrance region of a circular tube with a uniform wall temperature. Their experiments yielded heat transfer data in close accord with their theoretical predictions. They attributed this to the fact that a tube with a smaller diameter was used in these experiments, and the effect of natural convection was suppressed. They showed that the theoretical result of Zerkle and Sunderland was in excellent agreement with their theory for $Pr = 7$ and 10 . They indicated that the parabolic velocity profile employed by Zerkle and Sunderland represented a limiting case of their study for large Prandtl number fluids. On the contrary, the slug flow result could not be realized in the combined hydrodynamic and thermal entrance regions for large Prandtl numbers. The Grashof number (Rayleigh number is more appropriate measure for $Pr > 1$), which indicates the natural convection effect, was of the order of 10^4 in their experiment, whereas it was of the order of 10^5 in Depew and Zenter's experiment and of the order of

10^6 in Zerkle and Sunderland's experiment. They added that the large discrepancy due to the effects of natural convection in previous works [18, 22] could be reduced drastically by using test sections with smaller diameter.

DesRuisseaux and Zerkle [25] presented a theoretical technique for predicting the conditions under which a hydraulic system freezes shut and provided experimental results for comparison. They considered laminar liquid flow through a tube between two reservoirs. The tube was divided into two sections: one is adiabatic section and the other freezing section. Freezing was assumed to occur within a short freezing section having a uniform wall temperature lower than the liquid freezing temperature. The main point of interest was the final condition of the system, either the existence of a steady-state flow or complete blockage within the freezing section. Their theoretical analysis resulted in an equation for the system pressure drop:

$$\rho g \Delta h = \frac{\rho V_{ad}^2}{2} \left(2.28 + \frac{64 L_{ad}}{Re_{ad} D} + \frac{4}{3 R_e^4} (1 - R_e^4) + 16 Pr \int_0^z \frac{dz}{R^4} \right)$$

where Δh is the head difference between inlet and discharge reservoirs, and g is the acceleration of gravity. The subscripts $_{ad}$ and $_e$ denote adiabatic tube section and freezing section exit, respectively. The integral is for the freezing section only. The first two terms within parenthesis represent the pressure drop from the inlet reservoir through the adiabatic tube section and the last two terms represent the pressure drop across the freezing section. The theoretical minimum pressure drops to prevent the system from freezing shut were taken from the plots of pressure drop neglecting and including natural convection versus steady-state Reynolds number. The experimental pressure drop data obtained with heat transfer and solidification were plotted versus Su^{-1} along with the minimum pressure drops to prevent the system from freezing shut, which were taken from the separate plots of pressure drop neglecting and in-

cluding natural convection versus steady-state Reynolds number. The experimental data were designated as either a steady-state with flow or freezing-shut of the tube. Then the plot was divided, by a curve separating the two distinct data points, into two regions: steady-state flow zone and freeze-up zone. It was evident from the plot that the theoretical analysis neglecting natural convection successfully predicted an upper bound for the pressure drop which should be maintained across the system to prevent it from freezing shut. They assumed that the axial velocity profile remained parabolic throughout the freezing section, which allowed a relatively simple analytical approach. For more accuracy, they suggested a finite-difference solution of the differential equations of motion and conservation of energy as an alternate approach.

Lock *et al.* [26] presented a theoretical analysis of ice formation in a convectively-cooled pipe. They adopted Zerkle and Sunderland's strategic methodology, even though their problem was different from that of Zerkle and Sunderland's in that preceding the region where freezing occurs, there must be an ice-free zone. The problem posed was that of convection in hydrodynamically fully developed flow within a circular tube which is suddenly and uniformly cooled by an external coolant: that is, the problem was of the Graetz type with a boundary condition of the third kind. In the ice-free zone, the wall temperature decreased from the inlet water temperature to the freezing temperature. Their analysis yielded the length of the ice-free zone and provided a description of the solid-liquid interface and its effect on pressure when the water flow rate was fixed. The steady-state ice thickness increased with increasing Biot number, and as $Bi \rightarrow \infty$, the curve tended toward the result of Zerkle and Sunderland [18], as expected. They also discussed transient results, which showed that the entry length of the freezing zone might or might not change with time and

was strongly affected by external conditions. They derived an equation for the overall pressure drop in the presence of ice layer:

$$\Delta\bar{P} = \frac{8\rho Pr Q^2}{\pi^2 a^4} \left(z_{ad} + \frac{1}{12Pr} \left(\frac{1}{R^4} - 1 \right) + \int_0^z \frac{dz}{R^4} \right) \quad \text{for } z \geq z_{ad}$$

where $\Delta\bar{P} = \bar{P}(0) - \bar{P}(z)$ and Q is the volume flow rate. The integral is for the freezing zone and z_{ad} is the length of the ice-free zone. The most significant feature of their analysis was the large number of variables and parameters which entered into the description of the ice-free thickness and pressure. For the most general description eight independent quantities had to be considered: z , t , Bi , Su^* , K , Re , Pr , and Ste . In their analysis, they divided Su into Su^* (only temperature ratio) and K (thermal conductivity ratio).

Hwang and Yih [27] resolved the problem considered by Lock *et al.* [26] by using a conventional power series solution and also by the Crank-Nicholson finite-difference method. They pointed out that it was inaccurate to use the first few eigenvalues obtained from the asymptotic solution (for the Graetz problem, a problem with boundary condition of the first kind) to compute the length of ice-free zone for the boundary condition of the second or third kind. They showed that their power series solution and numerical solution agreed excellently, and that the asymptotic solution of Lock *et al.* checked well with their solutions when the Biot number was large such as 5.0 or 10.0 whereas the discrepancy became more pronounced as the Biot number decreased. Comparison between the first eigenvalues obtained from their solution and those from the asymptotic solution revealed that for the case of $Bi \rightarrow \infty$ the error was found to be only 1.4% whereas the error increased as the Biot number decreased and a 60% error was found for the case of $Bi = 0.25$. They concluded that a large error in the length of ice-free zone resulted from employing

the eigenvalues computed from the asymptotic solution for the boundary condition of the second or third kind and that the conventional power series method should be used in calculating the first few eigenvalues.

All of the experimental studies [22, 23, 24, 25] reviewed in the foregoing have dealt with freezing in laminar flow. An investigation of the freezing in forced turbulent flow inside circular tubes was made by Arora and Howell [28] in 1973. They developed a mathematical model to predict the maximum supercooling that could be obtained in a liquid in forced flow inside a circular tube as a function of Reynolds number, tube inside diameter, and local tube wall temperature. Since supercooling (phenomenon whereby liquid may be cooled below its freezing temperature before it starts to freeze) is a nucleation or initiation phenomenon which is critically related to the purity of fluid and rate of heat transfer, it is most surprising that Arora and Howell made no attempts to account for these variables in their model.

Arora and Howell also carried out an experiment to record the maximum supercooling that could be obtained in water. Their experimental data did not consistently show specific relationships or agreement with their theory. More supercooling was obtained at higher Reynolds numbers as predicted; however, contrary to expectations, more supercooling was observed for a larger inside-diameter tube. Perhaps this discrepancy could have been resolved had the model taken the rate of heat transfer and fluid purity into account. It was found difficult to predict exactly when the flow of supercooled water would freeze, even from the experimental data obtained. Nonetheless, they showed that there was a distinct demarcation of the “may freeze” and “will always freeze” zones, by plotting the experimental data on a plot of Re versus ΔT_{sup} , which is the degree of the superheating. By drawing so-called limiting region curves

on the plot, by which the region of data points were separated from no data region, they could mark the region above the curve, where experimental data were plotted, as “may freeze” zone and the region below the curve as “will always freeze” zone.

Thomason *et al.* [29] considered the same kind of problem as Zerkle and Sunderland for the case of turbulent flow and employed many of the same assumptions. However, they did not use the assumption that the solid phase shell was smooth and had a monotonically increasing thickness beginning at the thermal entrance, which was employed by Zerkle and Sunderland. In their analysis, they adapted the expression for the Nusselt number given by Sparrow *et al.* [30]:

$$Nu_z = \left(\frac{1}{Nu_\infty} - \frac{1}{2} \sum \frac{\exp(-\gamma_m^2 z / Re Pr a)}{Am \gamma_m^4} \right)^{-1}$$

where Am and γ_m are the expansion coefficients and eigenvalues of the solution, both of which are functions of Re and Pr for turbulent flow. The asymptotic Nusselt number, Nu_∞ , was adapted from Kays [31]:

$$Nu_\infty = 0.0155 Re^{0.83} Pr^{0.5} / R^{0.83}$$

A Blasius type pressure drop expression was employed while neglecting second order interface curvature effects. Comparison between their experimental heat transfer and pressure drop data and their analytical predictions showed that there was a basic agreement between theory and experiment. It was also shown experimentally that small nonuniformities in wall temperature could produce wide variations in pressure drop when a frozen layer existed within a tube. One interesting characteristic of their analytical solutions was that a very peculiar crust profile occurred. A concave curvature was found to occur in the mid-range z . However, this result was not verified by their experiments.

Shibani and Ozisik [32] solved a steady-state freezing of liquids in turbulent flow inside a tube with its walls kept at a uniform temperature lower than the freezing temperature of the liquid. They established the effects of Re and Pr on the location of solid-liquid interface and on the heat transfer rate as a function of position along the tube. Their computation ranges were $10^4 \leq Re \leq 10^6$ and $0 \leq Pr \leq 10^3$. They showed the variation of the Reynolds number in the range considered had a negligible effect on the radius of the solid-liquid interface and the heat transfer rate. They showed that the radius of the solid-liquid interface was slightly larger with turbulent flow than with laminar flow for small values of z (dimensionless axial position), and this trend was reversed for the larger values of z . Increasing the Prandtl number decreased the value of z for the closure. They also showed that the heat transfer rates for a given value of z were larger with the turbulent flow than with the laminar flow, and increasing the Prandtl number increased the rate of heat transfer in turbulent flow. Shibani and Ozisik also solved a similar problem in turbulent flow between parallel plates [33]. Matched asymptotic technique was used to study the effects of liquid superheat (using the freezing parameter $\bar{\theta} = Su^{-1}$) on location of solid-liquid interface and heat transfer rate. Decreased value of Su resulted in increases of freeze layer and total heat transfer rate. The freezing problem in parallel plate channels were also analyzed by other researchers [34, 35], whose analyses were similar to that of Zerkle and Sunderland.

1.2.1.3 Transient analysis Ozisik and Mulligan [36] analytically investigated the transient freezing of a liquid flowing inside a circular tube. They assumed constant tube wall temperature below the freezing temperature, constant properties,

a slug-flow velocity profile, and quasisteady-state heat conduction in the solid phase. They determined the variation of the local heat flux and the profile of the solid-liquid interface during freezing as a function of time and position along the tube. Their analysis produced steady-state heat transfer rates and profiles for solid-liquid interface which agreed well with experimental data of Zerkle and Sunderland [18]. They restricted the range of applicability of their solution to regions where the rate of change of thickness of the frozen layer with both time and distance along the tube was small, due to the combined effect of the simplifying assumptions employed. Ozisik and Mulligan noted that blockage is important only in problems involving flows (with insufficient superheat) from a reservoir at constant pressure. The pressure gradient may then vanish when the flow passage freezes shut. In problems which deal with a mass flow rate that is approximately constant, blockage cannot occur. Their investigation dealt only with constant flow rate – thus complete freezing could not occur.

Bilenas and Jiji [37] reported solutions of transient solidification in tubes based on both numerical methods and approximate variational techniques. The model used in their study also assumed the constant flow rate condition. The variational solutions were based on laminar convection and a parabolic velocity profile. Bilenas and Jiji compared their solutions for the time history and axial distribution of the frozen layer thickness with those of Ozisik and Mulligan [36] and concluded that the assumed velocity distributions had a small effect on the interface position. They found that the choice of the temperature distributions was important for accurate prediction of the instantaneous thickness of the frozen layer.

Martinez and Beaubouef [38] presented a numerical model for treating transient

Table 1.1: Numerical parameters and results of transient freezing

Case	Su	P_C	transient result
A	5.0	50	steady-state
B	0.5	50	freeze-shut
C	0.5	1000	freeze-shut
D	0.5	10000	steady-state

freezing in laminar tube flow. Their numerical analysis allowed for a decrease in pressure drop across the freeze section with increasing flow rate to model the presence of a (linear) pump for moving the liquid through the system. The parabolic axial velocity distribution was assumed. The problem was formulated using six independent parameters: Ste , Su , λ , Pr , Gz , and P_C . P_C is the dimensionless pump characteristic parameter defined as

$$P_C = \frac{8SQ_0}{h_0} = \frac{8(h_0 - h_0)}{h_0} = \frac{\pi Sa^3 a}{\nu L}$$

where Q_0 and h_0 are initial flow rate and head loss, respectively, and $-S$ is the slope of the characteristic line of a linear pump on a head loss versus flow rate plot. P_C physically means pumping capacity to overcome the head loss through the pipe due to the friction. For a linear pump, they assumed the head loss in the freezing section to be a function of the liquid flow rate, as

$$h = h_0 - SQ$$

where h_0 is the pumping system shut-off head. They considered four combinations of only two independent parameters, Su and P_C , keeping the others the same. Their transient solutions are summarized in Table 1.1, as well as the parameters for the four cases.

Case A reached steady-state with a relatively thin ice layer because the liquid temperature was significantly above the freezing temperature. Case B and Case C reached complete occlusion of the tube with ice due to their reduced superheats. Case C took a longer time to freeze shut than Case B because of the greater pumping capability. Case D reached steady state because the increased pumping capability was sufficient to inhibit tube blockage by ice even at the reduced level of superheat. The steady state for Case D had a considerably thicker ice layer compared to that of Case A. This is due to the reduced level of superheat, which required less sensible cooling before the liquid was frozen so that more ice could grow. For the steady state of Case D, the diameter of the flow passage at the exit of the freezing region was less than 20% of the tube diameter. Martinez and Beaubouef concluded that Su and P_c were the determining factors whether the transient solidification would result in a steady state of equilibrium flow or a cessation of flow due to tube blockage by frozen material.

Cho and Ozisik [39] solved the transient problem of the freezing of a liquid in turbulent flow inside a circular tube whose wall was kept at a uniform temperature below the freezing temperature. The radius of the solid-liquid interface and the local wall heat flux were determined as a function of time and position along the tube for several different values of the Prandtl number and the freezing parameter, which was the reciprocal of the superheat number. In fact, they combined the transient problem of Ozisik and Mulligan [36] and the turbulent flow of Shibani and Ozisik [32].

Transient freezing of a liquid in a convectively cooled tube was investigated analytically by Sadeghipour *et al.* [40], who illustrated the effects of Biot number, fluid inlet temperature, and the external ambient temperature on the length of the

freeze-free zone. They determined the variation of the thickness of the freeze layer as a function of time and position along the tube. The test section was divided into two zones: (1) the “freeze-free” or “cooling” zone ($0 < z \leq z_f$), where z_f is the location where the wall temperature is equal to the freezing temperature and (2) the “freezing” zone ($z > z_f$), wherein the wall temperature is below the freezing temperature, and a frozen layer has formed at the inside tube surface. They analyzed each zone separately and coupled them at z_f .

1.2.2 Flow instability and ice-band structure

1.2.2.1 Initial observations In 1968, Stephan [41] investigated the influence of heat transfer on melting and freezing in a forced flow. He predicted the solidification of fluids flowing along a plane wall or through a pipe with the assumption of a finite ambient heat transfer and an imposed or known heat flux to the solid-liquid interface. In his investigation of solidification in pipe flow, he found an interesting phenomenon. If solidification comes to a stop, this critical point may represent a stable or an unstable state. A stable point is characterized by the fact that, following a small disturbance, by a change of heat flux at the phase interface for example, the solid layer returns to its original thickness as soon as the disturbance disappears. An unstable point is characterized by the fact that, after the disturbance disappears, the solid layer will continue to grow or to melt according to the sign of the disturbance. Whether the point that is reached is stable or unstable depends on preceding occurrences in the solidification process.

In 1979, Gilpin [42] made visual observations of the development of the ice structure in pipe flow. He found that the steady-state ice profile did not produce

a uniformly tapered flow passage as assumed in previous studies but rather a flow passage with a dramatic cyclical variation in cross-section along the length of the pipe. The schematic diagram of the steady-state ice profile is shown in Figure 1.3. He called this steady-state ice profile "ice-band structure," which was a dominant feature of the ice growth that occurred over the entire range of Reynolds numbers studied, from 370 to 3025. The apparatus used in his observation included the test section, a water reservoir, a flow meter, a gear pump, and a constant temperature bath. The test section consisted of two concentric glass tubes, in which the coolant (methanol and water) was circulated at a high velocity. The water being frozen was pumped from the constant temperature bath into the center tube of the test section, which had an inner diameter of 33 mm, a length of 1.5 m, and a wall thickness of 1 mm. The experiment was conducted with the test section in the vertical position to minimize the effect of natural convection. In the experiment, three independent variables could be controlled: the coolant temperature, the inlet water temperature, and the water flow rate. The growth of the ice was presented in photographs obtained from 35 mm time lapse photography, with food dye added to the water to distinguish it from the ice.

Early in the experiment, after the tube-wall temperature was lowered below 0°C , the thickness of the ice increased in the flow direction. Several hours after the initiation of ice growth, however, a most interesting phenomenon was observed. At the exit of the test section, where the ice layer abruptly ended and the flow cross section suddenly expanded, the downstream face of the ice layer began to melt away. This melt zone propagated slowly upstream, leaving behind a flow passage free of ice, until it reached some equilibrium position and stopped. Depending on the values of

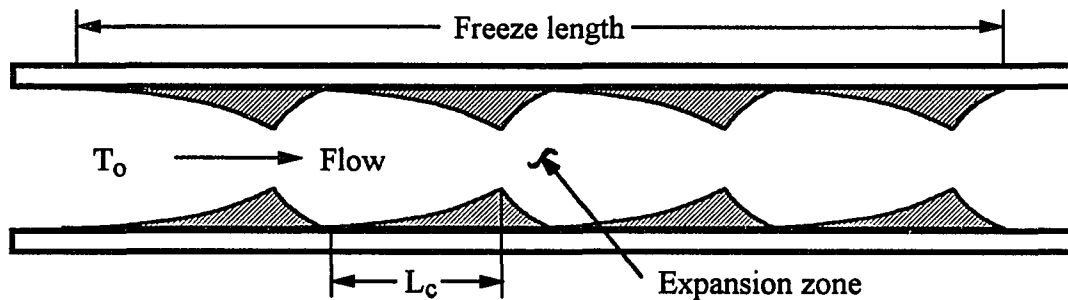


Figure 1.3: Schematic diagram of the ice-band structure

the water and coolant temperature, new ice growth might begin in the region between the melt zone and the test-section exit. This could be followed by the appearance of another melt zone that propagated upstream and came to rest at some equilibrium position downstream of the first melt zone.

1.2.2.2 Analysis of ice-band structure Gilpin explained the development of this ice-band structure as follows: "In the converging water passage that exists prior to the separation developing the flow is laminar. At the end of the cooled section, an increase in flow cross-section occurs which causes a flow separation and a transition to turbulent flow. The turbulent heat transfer downstream of the separation then melts away the ice on downstream face of the ice causing the separation point to move upstream. As the separation point moves upstream it moves into regions of a thinner ice annulus. For a thinner ice annulus the temperature gradient in the ice is larger and the change in ice thickness at the separation point is smaller. Further upstream migration presumably ceases when the change in convective heat transfer

rate between upstream and downstream of the separation just balances the change in conduction through the ice layer.” Gilpin attributed the enhanced heat transfer downstream of the separation point to the transition from laminar to turbulent flow; however, he did not include the possibility of the enhanced heat transfer due to flow separation even in laminar flow.

Gilpin observed that there was a good correlation between the distance to the first separation point and the temperature ratio θ , which was defined as

$$\theta = \frac{T_o - T_c}{T_i - T_o}$$

where T_c , T_o , and T_i are temperatures of the coolant, freezing point, and the water, respectively. The correlation was given by

$$\frac{L}{D} = \frac{80}{\theta^2} \quad (1.3)$$

where L is the length from the inlet to the first separation point, and D is the pipe diameter. The distances between subsequent separation points were more variable but were consistently 1.5 to 2.5 times the distance to the first separation. He also found a correlation for the diameter of the water passage (d , the “neck diameter”) immediately upstream of the separation point. A correlation for the equilibrium neck diameter was given by

$$\ln \frac{D}{d} = 33.2 / Re_D^{1/2}$$

where the neck diameter d is correlated with the pipe Reynolds number and is independent of θ .

In the second set of experiments, Gilpin [43] investigated the form of the ice growth in a pipe containing flows that were initially turbulent and determined the

effect of ice-band structure on pressure drop and pipe freeze-off. The transient development of the ice structure in this case was quite different from the behavior observed at low Reynolds numbers. The ice-band structure did not begin at the exit of the freeze section, but each band grew spontaneously from very small undulations in the flow passage diameter to its final steady-state size. Even though the transient growth phase was quite different, the final steady-state ice-band structure was very similar to that observed at lower Reynolds numbers. He also found that the ice-band structure was a feature that occurred predominantly at value a θ greater than one. For values of θ less than one, uniformly tapered flow passage was likely to be the more common ice configuration.

Gilpin pointed out that “it is the development of flow separation points that can migrate upstream that is the physical aspect of the problems not considered in most theories. These theories assume that the flow passage cross-section varies slowly with position along the pipe. The equation developed are then parabolic and thus do not allow any upstream migration of disturbances.” He indicated the resemblance of the behavior of the separation points in a pipe with the behavior of the “laminar to turbulent transition” observed during ice growth on a flat plate [44]. In his observation of upstream migration of disturbances, however, whether the flow was turbulent or still laminar with separation is not clear.

In two accompanying papers, Hirata *et al.* reported the steady-state ice layer profile on a constant temperature plate in a forced convection flow: I. Laminar regime [45] and II. Transition and turbulent regimes [44]. In the laminar regime, the ice layer thickness continually increases with distance from the leading edge of the plate due to the decrease of the heat transfer coefficient that occurs as a laminar boundary layer

Table 1.2: Comparison of the onset Reynolds numbers

Laminar theory	“smooth” transition mode	“step” transition mode
3×10^5	7×10^4 to 1×10^5	as low as 3.9×10^4

develops. In the transition from laminar to turbulent flow, the heat transfer coefficient undergoes a substantial increase, which results in a decrease in ice thickness through the transition regime. They observed that the process of transition from laminar to turbulent flow on an ice surface was very different from that on a flat plate. They attributed this to the fact that both phase change and convection were involved in the flow transition on the ice surface. Mutual interaction of the shape of the ice surface, the fluid flow over the surface, and the heat transfer to the surface, in the case of flow transition, resulted in two distinct transition modes: “smooth” transition and “step” transition.

For the “smooth” transition mode the ice thickness decreased smoothly and the flow remained attached to the ice surface, whereas in a second transition mode flow separation occurred and a “step” decrease in ice thickness resulted. Generally the “smooth” transition occurred on thin ice layer and the “step” transition occurred on thick ice layer. Hirata *et al.* observed the Reynolds numbers at which turbulence produced a measurable increase in heat transfer rates. They found that the onset Reynolds numbers on the ice surface were lower than those for a flat plate. Those onset Reynolds numbers they found for each mode are compared in Table 1.2. The deviation from the laminar theory was greater for the “step” transition. The transition point was found to migrate upstream on the ice surface to a final steady-state position which depended on an ice thickness parameter.

Epstein and Cheung [46] presented a study on the prediction of pipe freeze-shut

in turbulent flow. In order to identify the conditions for blockage of a pipe by freezing with a turbulent flow in it, they plotted the dimensionless pressure drop versus Su^{-1} for a different set of freeze section-to-pipe diameter z/D_o . The critical pressure drop below which freeze-shut occurs may be increased by either decreasing Su or increasing z/D_o . Physically, pipe blockage is more likely to occur in a longer pipe maintained at a lower wall temperature. From the observation that a more severe condition for pipe blockage may be expected when an ice-band structure exists in the pipe, they considered it important to determine the form of the crust structure before the conditions for pipe freeze-shut could be accurately predicted. They did this by dividing their plot into smooth crust structure and ice-band structure zones, by drawing Equation (1.3) on their plot. Using their analysis, they predicted that steady-state freezing is only possible for rather large cavity radii $R/R_o > 0.5$, for z/D_o and Su^{-1} as large as 10^3 and 1.0, respectively.

Cheung and Epstein [6] discussed the difference between Gilpin's study and previous pipe freezing studies in which ice band structure did not materialize. They approximated the smallest value of θ^{-1} in Zerkle and Sunderland's experiments to be 2.5 (3.13 is the correct value) and calculated the ice-band spacing for the work of Zerkle and Sunderland to be 500 (781 is the correct value) times the diameter, using Equation (1.3). Thus the ice-band length was very large compared to that of the test sections employed by Zerkle and Sunderland (pipe length-to-diameter ratios of 19 and 53.7). They mentioned that unless θ^{-1} was less than one, a smooth freeze cavity was likely to be the more common ice configuration in laboratory scale experiments, which is equivalent to Gilpin's conclusion [43].

Hirata and Ishihara [47] performed an experiment similar to Gilpin's experiment,

and they observed the same ice-band structure. They proposed correlation equations for the spacing of the ice bands, the heat transfer coefficient in the contraction region, and the friction factor in the pipe. They obtained the conditions for pipe freeze-off by introducing a modified Reynolds number based on a total pressure drop. Their cooling temperature ratio was defined slightly differently from that of Gilpin in that they used pipe wall temperature instead of coolant temperature and average value of water temperature at the inlet and outlet. The Reynolds number range in their experiments was $1600 \leq Re \leq 30000$.

1.2.2.3 Recent Developments It seems to be natural that recent developments in heat transfer and phase change areas are focused on the development of numerical models, which employ less simplifying assumptions to handle more complicated physical phenomena. Sparrow and Ohkubo [48] presented a methodology for the numerical solution of transient two-dimensional freezing of phase change medium contained within a closed vertical tube. Their numerical model took account of natural convection in the unfrozen liquid and heat conduction in the tube wall, as well as heat conduction in the frozen layer. The numerical solutions, which were presented in a companion paper [49], provided information on the responses of the freezing process to changes in the tube wall thickness and tube wall material and to changes in the convective heat transfer coefficient at the external surface of the tube.

Djilali *et al.* [50] used the turbulent flow about a two-dimensional blunt rectangular section as a test case to examine the performance of seven near-wall turbulence models. Their computation range was $20000 \leq Re \leq 75000$. They assessed the turbulence models by comparing resulting Nusselt number distributions and selected

fluid dynamic results with available experimental data. They concluded that a three-layer model of the wall region, applied to the k and ϵ equations, gave good agreement with the data, whereas the standard wall function treatment was not satisfactory at all for the flow considered.

A numerical method was presented by Albert and Olfe [51] to calculate freezing in forced laminar flow between parallel plates. Their purpose was to predict ice formation in the case of forced flow with the possibility of recirculation. Their numerical technique represented a coupled approach whereby the Navier-Stokes equations were solved in the fluid flow field, the heat conduction equation was solved in the solid region, and the interfacial boundary moved according to the latent heat condition and heat balance at the interface. They used a quasi-stationary method. Once the phase boundary was relocated, a new grid was generated for the region. Continuity, two momentum, and energy equations for liquid and energy equation for solid were solved for the fluid flow and temperature fields. The new location of the boundary was relocated, and the procedure repeated itself. They employed boundary-fitted orthogonal curvilinear coordinates and the stress-flux formulation modified to the finite volume procedure.

Most theoretical approaches so far have predicted monotonically increasing ice formation in forced flow. Albert and Olfe attributed this to the lack of details for the forced flow velocity field, thus not capturing much of the physics essential to the description of the irregular ice profiles that sometimes occur. They numerically investigated the possibility that disturbances large enough to cause recirculation might also allow irregular ice formation in laminar flow. In order to achieve an irregular ice profile, they assumed a step-like profile in the ice. In general, the step disappeared

as the ice melted or froze to its final configuration. A steady-state configuration was illustrated to be compared with the experimental ice profile result of Seki *et al.* [52]. They claimed that their numerical technique was able to simulate the behavior of non-uniform ice profiles in arbitrary geometries. They suggested that further work include turbulence and investigate the behavior of irregular ice profiles in the laminar and turbulent regimes, including wavy ice in pipes (ice-band structure).

1.3 Scope of the Present Study

This study solves the unsteady, axisymmetric freezing problem in pipe flows. Analytical analysis and numerical methods are used to determine solutions of the equations which govern the process. Two types of initial conditions are considered. The first is hydrodynamically and thermally fully developed flow, which has a uniform ice layer and exponentially varying temperature distributions. The second is the developing flow which has the monotonically increasing ice layer starting from zero thickness at the inlet along the axial direction. These initial conditions are not trivial and obtained by the analytical analysis of hydrodynamic and thermal fields. In order to study the transient ice layer growth in pipe flows, a numerical model is developed which can determine the evolution of the flow beyond its initial state. The numerical method employed in this study is the finite-difference method. The model first calculates initial conditions, and then transient calculation starts with the change of boundary conditions. For the fully developed initial condition, the wall temperature, which is initially exponentially increasing in the axial direction, is changed to a uniform temperature equal to the inlet value. Additional freezing occurs farther downstream of the inlet due to the lowered wall temperature. For the

developing initial condition, transient calculation begins with the onset of disturbance at the exit of the test section. The response to this disturbance is one of the foremost interests in the present study.

2. MATHEMATICAL ANALYSIS

2.1 The Physical Model

The schematic diagram of the freezing in a pipe flow is shown in Figure 2.1. The pipe wall temperature of the test section ($0 \leq \bar{z} \leq \bar{z}_{max}$) is prescribed as $T_w(\bar{z})$, which is below the freezing temperature of the phase-change material, T_o . A liquid PCM, whose temperature is prescribed as $T_i(\bar{r}) \geq T_o$ at the test section inlet ($\bar{z} = 0$), is flowing through the pipe with a constant mass flow rate. Because of the freezing of liquid PCM along the pipe wall, there exists an interface between the liquid phase and the solid phase which is, in general, a function of \bar{z} . The energy balance between the liquid phase and solid phase of the PCM gives a steady state, which becomes the initial state. A change in any of the boundary conditions upsets the energy balance and causes the interface shape and the flow pattern within the test section to change. Temperatures of the liquid and the solid regions and the flow velocity then vary with time. The radius of the solid-liquid interface varies as a function of time (\bar{t}) and axial location (\bar{z}) and is one of the unknowns that are determined as part of the solution.

Additional assumptions are:

- The model is unsteady and axisymmetric.
- The fluid is incompressible and Newtonian.

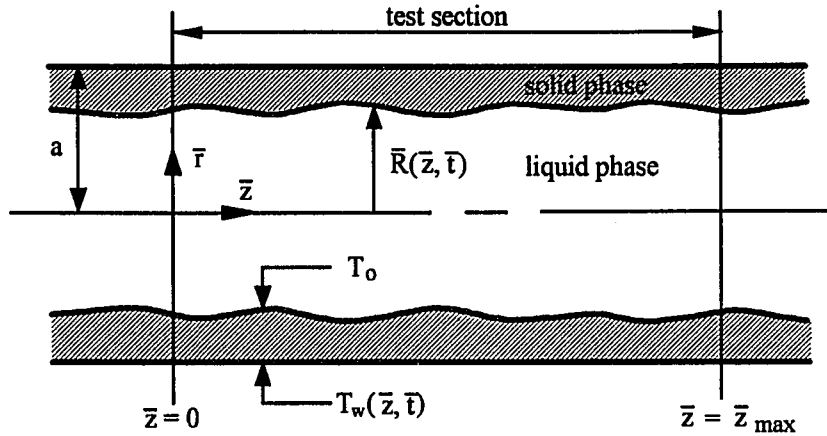


Figure 2.1: Schematic diagram of the freezing in a pipe flow

- The flow is laminar or weakly turbulent.
- All material properties are constant.
- The densities of the solid and liquid phases are the same.
- There exists a well-defined freezing temperature.
- Mass flow rates are constant.
- The Peclet number is very high.

These assumptions are made to reduce the complexity of the analysis, but they are reasonable approximations of the real freezing problem. The model is assumed to be axisymmetric because the natural convection effects are negligible for this kind of forced convection problem. Therefore the model becomes two-dimensional. Most fluids, especially water, are approximated as incompressible and Newtonian. The effects of density changes between solid and liquid are negligible [11, 12]. Sometimes

a freezing of a liquid does not take place even at a temperature lower than its freezing temperature [53], but this usually happens when the first layer of ice forms. Once it has formed, freezing becomes easier and takes place at the freezing temperature. The Peclet number, Pe , is a measure of the ratio of energy transport by convection to that by conduction. For a forced flow, convection heat transfer is generally much greater than conduction heat transfer. Therefore high Pe is assumed. A further discussion of this assumption can be found in Appendix A.

2.2 The Dimensional Formulation

2.2.1 Governing equations in primitive variables

Governing equations are obtained from basic conservations of mass, momentum, and energy. The equations are written in cylindrical coordinates. The independent variables are radial coordinate, \bar{r} , axial coordinate, \bar{z} , and time, \bar{t} . The bar over the variable indicates a dimensional variable. The dependent variables are radial velocity, \bar{u} , axial velocity, \bar{w} , pressure, \bar{P} , liquid temperature, \bar{T}_l , solid temperature, \bar{T}_s , and the radius of solid-liquid interface, \bar{R} .

The governing equations are:

$$\frac{\partial \bar{u}}{\partial \bar{r}} + \frac{\bar{u}}{\bar{r}} + \frac{\partial \bar{w}}{\partial \bar{z}} = 0 \quad (\text{continuity}) \quad (2.1)$$

$$\frac{\partial \bar{u}}{\partial \bar{t}} + \bar{u} \frac{\partial \bar{u}}{\partial \bar{r}} + \bar{w} \frac{\partial \bar{u}}{\partial \bar{z}} = -\frac{1}{\rho} \frac{\partial \bar{P}}{\partial \bar{r}} + \nu \left(\nabla^2 \bar{u} - \frac{\bar{u}}{\bar{r}^2} \right) \quad (\bar{r}\text{-momentum}) \quad (2.2)$$

$$\frac{\partial \bar{w}}{\partial \bar{t}} + \bar{u} \frac{\partial \bar{w}}{\partial \bar{r}} + \bar{w} \frac{\partial \bar{w}}{\partial \bar{z}} = -\frac{1}{\rho} \frac{\partial \bar{P}}{\partial \bar{z}} + \nu \nabla^2 \bar{w} \quad (\bar{z}\text{-momentum}) \quad (2.3)$$

$$\frac{\partial \bar{T}_l}{\partial \bar{t}} + \bar{u} \frac{\partial \bar{T}_l}{\partial \bar{r}} + \bar{w} \frac{\partial \bar{T}_l}{\partial \bar{z}} = \alpha_l \nabla^2 \bar{T}_l \quad (\text{liquid energy}) \quad (2.4)$$

$$\frac{\partial \bar{T}_s}{\partial t} = \alpha_s \nabla^2 \bar{T}_s \quad (\text{solid energy}) \quad (2.5)$$

$$\rho_s h_{sI} \dot{\bar{R}} = -k_l \left(\frac{\partial \bar{T}_l}{\partial \bar{r}} - \bar{R}' \frac{\partial \bar{T}_l}{\partial \bar{z}} \right) \Big|_{\bar{r}=\bar{R}} + k_s \left(\frac{\partial \bar{T}_s}{\partial \bar{r}} - \bar{R}' \frac{\partial \bar{T}_s}{\partial \bar{z}} \right) \Big|_{\bar{r}=\bar{R}} \quad (\text{interface}) \quad (2.6)$$

where $\nabla^2 = \frac{\partial^2}{\partial \bar{r}^2} + \frac{1}{\bar{r}} \frac{\partial}{\partial \bar{r}} + \frac{\partial^2}{\partial \bar{z}^2}$, $\dot{\bar{R}} = \frac{\partial \bar{R}}{\partial t}$ and $\bar{R}' = \frac{\partial \bar{R}}{\partial \bar{z}}$. ρ is the density, $\nu (= \frac{\mu}{\rho})$ is the momentum diffusivity, α is the thermal diffusivity, and k is the thermal conductivity. The subscripts l and s denote the properties of the liquid phase and solid phase, respectively.

The continuity equation is for the incompressible fluid flow. The left hand side of momentum equations has the unsteady term and the convection terms due to fluid flow. The right hand side contains the acceleration terms due to pressure gradient, diffusion, and source (only for \bar{r} -momentum equation). The energy equations contain the unsteady terms and the diffusion term, and the liquid energy equation has additionally the convection terms due to fluid flow. The interface equation can be derived by considering an energy balance on an infinitesimal control system located at the solid-liquid interface. The momentum and energy equations are coupled through the boundary conditions at the solid-liquid interface as well as through convective terms in the liquid energy equation.

Equations (2.1) - (2.6) constitute the set of governing equations to be solved for the freezing problem in the laminar pipe flow. These six equations can be reduced to five equations using stream function and vorticity, which are defined so as to automatically satisfy the continuity equation and eliminate pressure terms. This is presented in the following section, after boundary and initial conditions are addressed.

2.2.2 Boundary conditions

The momentum and energy equations are all elliptic partial differential equations in radial and axial coordinates. Therefore, two boundary conditions (in each spatial coordinate) for each dependent variable are needed to properly define a well-posed mathematical problem. The radial boundary conditions are (for all \bar{z}):

$$\bar{u} = 0 \quad \text{at } \bar{r} = 0 \quad \text{and} \quad \bar{u} = 0 \quad \text{at } \bar{r} = \bar{R} \quad (2.7)$$

$$\frac{\partial \bar{w}}{\partial \bar{r}} = 0 \quad \text{at } \bar{r} = 0 \quad \text{and} \quad \bar{w} = 0 \quad \text{at } \bar{r} = \bar{R} \quad (2.8)$$

$$\frac{\partial \bar{T}_l}{\partial \bar{r}} = 0 \quad \text{at } \bar{r} = 0 \quad \text{and} \quad \bar{T}_l = T_o \quad \text{at } \bar{r} = \bar{R} \quad (2.9)$$

$$\bar{T}_s = T_w(\bar{z}) \quad \text{at } \bar{r} = a \quad \text{and} \quad \bar{T}_s = T_o \quad \text{at } \bar{r} = \bar{R}. \quad (2.10)$$

Velocity boundary conditions are obtained from symmetry at the center and no-slip at the interface. Temperature boundary conditions at the interface are the freezing temperature, T_o . The liquid temperature boundary condition at the center is due to symmetry, while the solid temperature boundary condition at the pipe wall is specified, *a priori*. Boundary conditions for the pressure can be derived from the momentum equations by applying velocity boundary conditions at the boundaries, if needed.

Before the test section, the pipe wall temperature is at the liquid temperature above the freezing temperature; therefore, there is no ice, and the flow is hydrodynamically fully developed and thermally uniform. At the end of the test section, the freezing boundary condition is removed. Thus the flow approaches a fully developed, uniform temperature state, and the axial boundary conditions are:

$$\bar{u} = 0 \quad \text{for all } \bar{r}, \quad \bar{w} = \frac{Ga^2}{4\mu} \left(1 - \frac{\bar{r}^2}{a^2} \right) \quad \text{at } \bar{z} = 0 \quad \text{and as } \bar{z} \longrightarrow \infty \quad (2.11)$$

$$\bar{T}_l = T_i \quad \text{for all } \bar{r} \quad \text{at } \bar{z} = 0 \quad (2.12)$$

$$\bar{T}_l \longrightarrow \bar{T}_\infty > T_o \quad \text{for all } \bar{r} \quad \text{as } \bar{z} \longrightarrow \infty \quad (2.13)$$

where \bar{T}_∞ is the pipe wall temperature very far downstream from the test section. The axial velocity is parabolic with the maximum value at the center and is zero at the pipe wall. G is the uniform pressure gradient when the radius of the flow passage is uniformly a . For the constant mass flow rate, it can be derived as:

$$G = -\frac{\partial \bar{P}}{\partial \bar{z}} = \frac{8\nu \dot{m}}{\pi a^4}$$

where \dot{m} is the *given* mass flow rate.

2.2.3 Initial conditions

Two cases of initial conditions are considered for transient calculations: I. a hydrodynamically and thermally fully developed flow and II. a hydrodynamically and thermally developing flow.

2.2.3.1 Fully developed flow initial condition An initially uniform ice layer is assumed which is consistent with hydrodynamically and thermally fully developed flow. Compared to a case with the absence of ice layer, there is an increase in axial velocity because the mass flow rate is kept constant. Such an initial state requires a prescribed pipe wall temperature which increases exponentially to match energy balance at the solid-liquid interface. When the flow is thermally fully developed, the liquid temperature profile exhibits self similarity.

Velocity and temperature fields are given as:

$$\bar{u} = 0 \quad \text{for all } \bar{r} \text{ and } \bar{z} \quad (2.14)$$

$$\bar{w} = \frac{Ga^4}{4\mu\bar{R}_o^2} \left(1 - \frac{\bar{r}^2}{\bar{R}_o^2} \right) \quad \text{for all } \bar{z} \quad (2.15)$$

$$\bar{T}_l = T_o + (\bar{T}_{li} - T_o) \exp\left(-\frac{2\pi\bar{R}_oh}{\dot{m}\rho c} \bar{z}\right) \quad (2.16)$$

$$\bar{T}_s = T_o + \frac{k_l}{k_s} \bar{R}_o \left. \frac{\partial \bar{T}_l}{\partial \bar{r}} \right|_{\bar{r}=\bar{R}_o} \ln\left(\frac{\bar{r}}{\bar{R}_o}\right) \quad (2.17)$$

where \bar{T}_{li} is the liquid temperature at the inlet ($\bar{z} = 0$). \bar{T}_l and \bar{T}_s vary in radial coordinate in terms of \bar{T}_{li} and $\ln\left(\frac{\bar{r}}{\bar{R}_o}\right)$. Their variations in \bar{z} -coordinate are in the terms of $\exp\left(-\frac{2\pi\bar{R}_oh}{\dot{m}\rho c} \bar{z}\right)$ and $\left. \frac{\partial \bar{T}_l}{\partial \bar{r}} \right|_{\bar{r}=\bar{R}_o}$, respectively.

The uniform radius of the solid-liquid interface \bar{R}_o can be calculated from the solid temperature using the wall boundary condition: $\bar{T}_s = T_{wo}$ at $\bar{z} = 0$ and $\bar{r} = a$. The following equation results:

$$\frac{\bar{R}_o}{a} = \exp\left(\frac{k_s T_o - T_{wo}}{k_l \bar{T}_{mo} - T_o} \frac{1}{\left. \frac{\partial \bar{T}_l}{\partial \bar{r}} \right|_{\bar{r}=\bar{R}_o}}\right) \quad (2.18)$$

where \bar{T}_{mo} is the bulk mean temperature of the liquid at the inlet. This equation can be used to determine the fraction of the flow passage radius for the fully developed flow. All that is needed is the ratio of liquid to solid temperatures at the inlet.

2.2.3.2 Developing flow initial condition For an isothermal pipe wall boundary condition, an ice layer thickness which increases with axial location is a possible solution. In particular, when the wall temperature of an ice-free test section is suddenly dropped to $T_w(\bar{z}) = T_{wo} < T_o$, ice grows inwardly from the pipe wall along the test section. If the liquid possesses sufficient superheat, the ice layer asymptotically approaches a steady state characterized by a monotonically increasing

ice layer thickness. This steady state is considered as an initial condition for the full transient formulation.

The spatial domain for this initial condition is divided into two intervals. One in which the ice layer thickness is so thin that it has a negligible effect on the hydrodynamic field and the other in which the ice layer has some effect on it. A thin ice layer is assumed for the initial interval, $0 \leq \bar{z} \leq \bar{z}_{tr}$, in which equations for hydrodynamic and thermal fields are decoupled. Therefore, only equations for the thermal field are solved for $z \leq \bar{z}_{tr}$ whereas all the eqns must be solved simultaneously for $z > \bar{z}_{tr}$.

For the thin ice layer interval, velocity field is regarded as fully developed, and it is given by the inlet condition, Equation (2.11). The liquid temperature, the solid temperature, and the radius of the solid-liquid interface can be calculated from the following asymptotic equations (valid in the limits as $Pe \rightarrow \infty$ and $\bar{\epsilon} \rightarrow 0$):

$$\frac{Ga^2}{4\mu} \left(1 - \frac{\bar{r}^2}{a^2}\right) \frac{\partial \bar{T}_l}{\partial \bar{z}} = \alpha_l \frac{1}{\bar{r}} \frac{\partial}{\partial \bar{r}} \left(\bar{r} \frac{\partial \bar{T}_l}{\partial \bar{r}} \right) \quad (2.19)$$

$$\frac{\partial^2 \bar{T}_s}{\partial \bar{r}^2} + \frac{1}{\bar{r}} \frac{\partial \bar{T}_s}{\partial \bar{r}} = 0 \quad (2.20)$$

$$0 = -k_l \left(\frac{\partial \bar{T}_l}{\partial \bar{r}} - \bar{R}' \frac{\partial \bar{T}_l}{\partial \bar{z}} \right) \Big|_{\bar{r}=\bar{R}} + k_s \left(\frac{\partial \bar{T}_s}{\partial \bar{r}} - \bar{R}' \frac{\partial \bar{T}_s}{\partial \bar{z}} \right) \Big|_{\bar{r}=\bar{R}} \quad (2.21)$$

subject to boundary conditions:

$$\bar{T}_l = T_{io} \quad \text{for all } \bar{r} \quad \text{at } \bar{z} = 0$$

$$\frac{\partial \bar{T}_l}{\partial \bar{r}} = 0 \quad \text{for all } \bar{z} \quad \text{at } \bar{r} = 0$$

$$\bar{T}_l = T_o \quad \text{for } \bar{z} > 0 \quad \text{at } \bar{r} = \bar{R}$$

$$\bar{T}_s = T_o \quad \text{for } \bar{z} > 0 \quad \text{at } \bar{r} = \bar{R}$$

$$\bar{T}_s = T_{wo} \quad \text{for } \bar{z} > 0 \quad \text{at } \bar{r} = a.$$

Equations (2.19) and (2.20) are the reduced forms of Equations (2.4) and (2.5) using the scale analysis, as discussed in Appendix A (see Section A.1.2).

For the thick ice layer interval, the governing equations are the steady form of Equations (2.1) - (2.6) and the boundary conditions are exactly same as Equations (2.7) - (2.10). The initial conditions (*i.e.*, values of dependent variables at $\bar{z} = \bar{z}_{tr}$) are given by the solution from the thin ice layer interval.

2.2.4 Formulation using stream function and vorticity

A stream function, \bar{f} , is introduced such that continuity, Equation (2.1), is identically satisfied. The appropriate definitions are

$$\bar{u} = -\frac{1}{\bar{r}} \frac{\partial \bar{f}}{\partial \bar{z}} \quad \text{and} \quad \bar{w} = \frac{1}{\bar{r}} \frac{\partial \bar{f}}{\partial \bar{r}}. \quad (2.22)$$

Using the definition of vorticity ($\vec{\omega} = \text{curl } \vec{V}$), where \vec{V} is velocity vector, the vorticity vector can be expressed in terms of velocity components as:

$$\vec{\omega} = \vec{\nabla} \times \vec{V} = \left(\frac{\partial \bar{u}}{\partial \bar{z}} - \frac{\partial \bar{w}}{\partial \bar{r}} \right) \vec{e}_\theta.$$

Since the vorticity vector has only one component, it is regarded as a scalar quantity hereafter:

$$\bar{\omega} = \frac{\partial \bar{u}}{\partial \bar{z}} - \frac{\partial \bar{w}}{\partial \bar{r}}. \quad (2.23)$$

Now vorticity can be expressed in terms of stream function through the substitution of Equation (2.22) into Equation (2.23). Next, the velocities \bar{u} and \bar{w} are eliminated from the momentum equations using Equation (2.22). Then the pressure, \bar{P} , is eliminated from the momentum equations through cross-differentiation and subtraction. By introducing vorticity, the vorticity transport equation is obtained.

Finally the stream function, defined in Equation (2.22), is introduced into the liquid equation, Equation (2.4). Equations (2.1) - (2.4) are then replaced with the three equations:

$$\bar{\omega} = -\frac{1}{\bar{r}}\nabla^2\bar{f} + \frac{2}{\bar{r}^2}\frac{\partial\bar{f}}{\partial\bar{r}} \quad (2.24)$$

$$\frac{\partial\bar{\omega}}{\partial\bar{t}} + \frac{1}{\bar{r}}J(\bar{f},\bar{\omega}) + \frac{\bar{\omega}}{\bar{r}^2}\frac{\partial\bar{f}}{\partial\bar{z}} = \nu\left(\nabla^2\bar{\omega} - \frac{\bar{\omega}}{\bar{r}^2}\right) \quad (2.25)$$

$$\frac{\partial\bar{T}_l}{\partial\bar{t}} + \frac{1}{\bar{r}}J(\bar{f},\bar{T}_l) = \alpha_l\nabla^2\bar{T}_l \quad (2.26)$$

where $J(\bar{f},\phi) = \frac{\partial\bar{f}}{\partial\bar{r}}\frac{\partial\phi}{\partial\bar{z}} - \frac{\partial\bar{f}}{\partial\bar{z}}\frac{\partial\phi}{\partial\bar{r}}$ for $\phi = \bar{\omega}$ or \bar{T}_l .

Equations (2.24) - (2.26), (2.5), and (2.6) are now the governing equations for axisymmetric unsteady flow in cylindrical coordinates.

The corresponding boundary conditions follow from those of section 2.2 and the definitions of stream function and vorticity. For stream function, the first definition in Equation (2.22), coupled with boundary condition given by (2.7), indicates that the stream function is constant at the center and at the solid-liquid interface. Then integration of Equation (2.22) from 0 to \bar{r} gives

$$\bar{f}(\bar{r}) - \bar{f}(0) = \int_0^{\bar{r}} \bar{\omega}\bar{r}d\bar{r} = \int_0^{\bar{r}} \frac{Ga^2}{4\mu} \left(1 - \frac{\bar{r}^2}{a^2}\right) \bar{r}d\bar{r} = \frac{Ga^2}{4\mu} \left(\frac{\bar{r}^2}{2} - \frac{\bar{r}^4}{4a^2}\right) \quad (2.27)$$

where the fully developed velocity field is used because stream function values at the boundaries are constant for all \bar{z} for constant mass flow rate. Choosing $\bar{f} = 0$ at $\bar{r} = 0$ leads to

$$\bar{f} = \frac{Ga^4}{16\mu} \quad \text{at } \bar{r} = \bar{R}. \quad (2.28)$$

In two-dimensional flow, the difference between the values of stream function at two points is equal to the volume flow rate between the streamlines passing through

those points. In cylindrical coordinates, it is in fact a volume flow rate divided by 2π . Equation (2.28) can be rewritten using the constant mass flow rate as:

$$\bar{f} = \frac{\dot{m}}{2\pi\rho}.$$

Radial boundary conditions for vorticity are obtained from Equations (2.7), (2.8), (2.23), and (2.24). They are:

$$\bar{\omega} = 0 \quad \text{at } \bar{r} = 0 \quad \bar{\omega} = -\frac{1}{\bar{R}} \left(\frac{\partial^2 \bar{f}}{\partial \bar{r}^2} + \frac{\partial^2 \bar{f}}{\partial \bar{z}^2} \right) \Big|_{\bar{r}=\bar{R}} \quad \text{at } \bar{r} = \bar{R}. \quad (2.29)$$

Boundary conditions in the z -direction at the inlet and far downstream from the test section are hydrodynamically fully developed. Therefore,

$$\bar{f} = \frac{Ga^4}{16\mu} \left(2 - \frac{\bar{r}^2}{a^2} \right) \frac{\bar{r}^2}{a^2} \quad \text{and} \quad \bar{\omega} = \frac{G\bar{r}}{2\mu} \quad \text{at } \bar{z} = 0 \quad \text{and} \quad \bar{z} \rightarrow \infty. \quad (2.30)$$

2.3 The Dimensionless Formulation

2.3.1 Coordinate transformation

As the ice forms inside the pipe, the solid-liquid interface varies with time and axial location. This moving boundary complicates the calculation of dependent variables; therefore, it is good to immobilize the boundaries of solid and liquid regions. This is done by nondimensionalizing radial coordinates using proper characteristic length scale for each region. As a result, non-uniform and varying physical domains are transformed into uniform and fixed domains. Figure 2.2 shows the physical and transformed domains for the liquid and solid phases. The dimensional radius, \bar{r} , varies from 0 to \bar{R} in the liquid phase and from \bar{R} to a in the solid phase. The transformed radial coordinates vary from 0 (centerline or pipe wall) to 1 (interface), respectively.

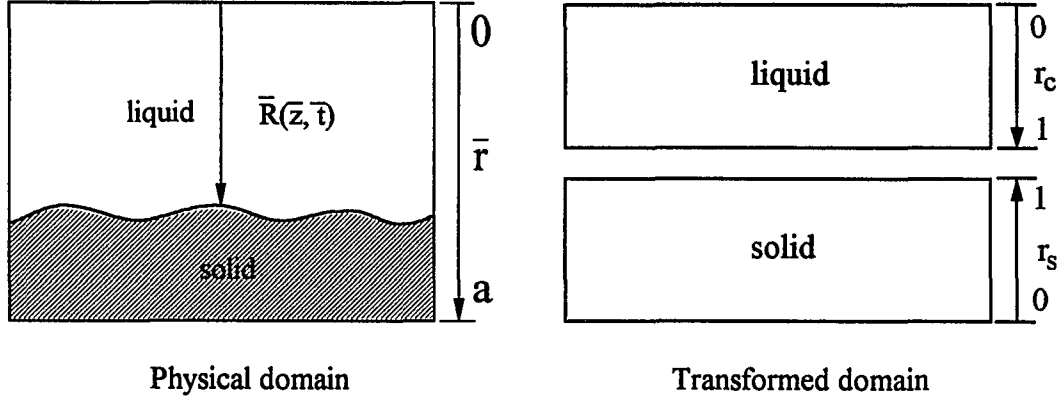


Figure 2.2: Coordinate transformation: Physical and transformed domains

The dimensionless variables are defined as:

$$\begin{aligned}
 t &= \frac{\bar{t}}{a^2/\alpha_s} & z &= \frac{\bar{z}}{aPe} & r_c &= \frac{\bar{r}}{\bar{R}} & r_s &= \frac{a - \bar{r}}{a - \bar{R}} \\
 f &= \frac{\bar{f}}{Ga^4/4\mu} & \omega &= \frac{\bar{\omega}}{Ga/4\mu} & T_l &= \frac{\bar{T}_l - T_o}{T_{io} - T_o} & T_s &= \frac{\bar{T}_s - T_{wo}}{T_o - T_{wo}} \\
 & & R &= \frac{\bar{R}}{a} & \epsilon &= \frac{\bar{\epsilon}}{a}
 \end{aligned}$$

where $\bar{\epsilon}$ is the ice layer thickness and $\bar{\epsilon} + \bar{R} = a$. Characteristic scales for time and axial coordinates are freezing time from the pipe wall into the center line and thermal entry length of the pipe flow, respectively. Pe is the the Peclet number and is defined in the next section (see Equation (2.36)). T_{io} is the inlet liquid PCM temperature at the center, and T_{wo} is the inlet wall temperature.

2.3.2 Governing equations

Dimensionless variables are substituted into equations (2.24) - (2.26), (2.5), and (2.6). After some algebraic simplification, the following dimensionless governing equations result:

$$\frac{\partial^2 f}{\partial r_c^2} - \frac{1}{r_c} \frac{\partial f}{\partial r_c} + R^3 r_c \omega + \frac{R^2}{Pe^2} \frac{\partial^2 f}{\partial z^2} - \frac{Mf}{Pe^2} = 0 \quad (\text{stream function}) \quad (2.31)$$

$$\begin{aligned} & -\frac{R^2}{\lambda Pr} \frac{\partial \omega}{\partial t} + \frac{\partial^2 \omega}{\partial r_c^2} + \left(\frac{1}{r_c} + \frac{1}{r_c Pr} \frac{\partial f}{\partial z} + \frac{r_c R \dot{R}}{\lambda Pr} \right) \frac{\partial \omega}{\partial r_c} - \frac{1}{r_c Pr} \frac{\partial f}{\partial r_c} \frac{\partial \omega}{\partial z} \\ & - \frac{\omega}{r_c^2 Pr} \left(\frac{\partial f}{\partial z} - r_c \frac{R'}{R} \frac{\partial f}{\partial r_c} \right) - \frac{\omega}{r_c^2} + \frac{R^2}{Pe^2} \frac{\partial^2 \omega}{\partial z^2} - \frac{M\omega}{Pe^2} = 0 \quad (\text{vorticity}) \end{aligned} \quad (2.32)$$

$$\begin{aligned} & -\frac{R^2}{\lambda} \frac{\partial T_l}{\partial t} + \frac{\partial^2 T_l}{\partial r_c^2} + \left(\frac{1}{r_c} + \frac{1}{r_c} \frac{\partial f}{\partial z} + \frac{r_c R \dot{R}}{\lambda} \right) \frac{\partial T_l}{\partial r_c} - \frac{1}{r_c} \frac{\partial f}{\partial r_c} \frac{\partial T_l}{\partial z} \\ & + \frac{R^2}{Pe^2} \frac{\partial^2 T_l}{\partial z^2} - \frac{MT_l}{Pe^2} = 0 \quad (\text{liquid energy}) \end{aligned} \quad (2.33)$$

$$-\epsilon^2 \frac{\partial T_s}{\partial t} + \frac{\partial^2 T_s}{\partial r_s^2} - \left(\frac{\epsilon}{1 - \epsilon r_s} - r_s \epsilon \dot{\epsilon} \right) \frac{\partial T_s}{\partial r_s} + \frac{\epsilon^2}{Pe^2} \frac{\partial^2 T_s}{\partial z^2} - \frac{NT_s}{Pe^2} = 0 \quad (\text{solid energy}) \quad (2.34)$$

$$\frac{\partial \epsilon}{\partial t} = Ste \left(\frac{Su}{1 - \epsilon} \frac{\partial T_l}{\partial r_c} \Big|_{r_c=1} + \frac{1}{\epsilon} \frac{\partial T_s}{\partial r_s} \Big|_{r_s=1} \right) \left(1 + \frac{\epsilon'^2}{Pe^2} \right) \quad (\text{interface}) \quad (2.35)$$

where

$$\begin{aligned} -M &= (r_c R')^2 \frac{\partial^2}{\partial r_c^2} - 2r_c R R' \frac{\partial^2}{\partial r_c \partial z} + \left(2r_c R'^2 - r_c R R'' \right) \frac{\partial}{\partial r_c} \\ -N &= (r_s \epsilon')^2 \frac{\partial^2}{\partial r_s^2} - 2r_s \epsilon \epsilon' \frac{\partial^2}{\partial r_s \partial z} + \left(2r_s \epsilon'^2 - r_s \epsilon \epsilon'' \right) \frac{\partial}{\partial r_s} \end{aligned}$$

and the additional dimensionless parameters are defined as

$$Pr = \frac{\nu}{\alpha_l} \quad \lambda = \frac{\alpha_l}{\alpha_s} \quad Pe = \frac{Ga^3}{4\mu\alpha_l} \quad Ste = \frac{c_s(T_o - T_{wo})}{h_{sl}} \quad Su = \frac{k_l (T_{io} - T_o)}{k_s (T_o - T_{wo})} \quad (2.36)$$

where c_s is the specific heat of the solid PCM, and h_{sl} is the latent heat of melting. λ is the ratio of liquid to solid thermal diffusivities, and Pe is the ratio of energy transport by convection to that by conduction. Ste is the ratio of the sensible heat in the solid phase to the latent heat of phase change, and it is important only in transient calculation. Su is the ratio of sensible heats in the liquid and solid phases, and it represents the radial temperature boundary condition of the problem.

Note the appearance of the differential operators, M and N . They represent the effects of the non-uniform radius of the solid-liquid interface and vanish if the interface is uniform along the axial coordinate. The use of the transformation also causes a second type of term to appear in the dimensionless equations. This is $\dot{R} \frac{\partial}{\partial r}$ term which appears in equations (2.32) - (2.34). This term introduces the effect of the temporal growth of the interface as a convection term into the dimensionless governing equations. The details of the chain rules of transformation and differential operators can be found in Appendix B.

2.3.3 Boundary conditions

The dimensionless boundary conditions are found by substituting dimensionless variables into the dimensional boundary conditions, (2.9) - (2.10) and (2.28) - (2.29). The radial conditions are (for all z):

$$f = 0 \quad \text{at } r_c = 0 \quad \text{and} \quad f = \frac{1}{4} \quad \text{at } r_c = 1 \quad (2.37)$$

$$\omega = 0 \quad \text{at } r_c = 0 \quad \text{and} \quad \omega = -\frac{1}{R^3} \frac{\partial^2 f}{\partial r_c^2} \left(1 + \frac{R'^2}{Pe^2} \right) \quad \text{at } r_c = 1 \quad (2.38)$$

$$\frac{\partial T_l}{\partial r_c} = 0 \quad \text{at } r_c = 0 \quad \text{and} \quad T_l = 0 \quad \text{at } r_c = 1 \quad (2.39)$$

$$T_s = 0 \quad \text{at } r_s = 0 \quad \text{and} \quad T_s = 1 \quad \text{at } r_s = 1. \quad (2.40)$$

The inlet and far field outlet conditions are:

$$f = \frac{1}{4}(2 - r_c^2)r_c^2 \quad \text{and} \quad \omega = \frac{2r_c}{R_o^3} \quad \text{at } z = 0 \text{ and } z \rightarrow \infty \quad (2.41)$$

$$T_l = 1 \quad \text{for all } r_c \quad \text{at } z = 0 \quad (2.42)$$

$$T_l \rightarrow T_\infty \quad \text{for all } r_c \quad \text{as } z \rightarrow \infty \quad (2.43)$$

where vorticity boundary condition becomes $\omega = 2r_c$ for the developing flow initial condition.

2.3.4 Initial conditions

2.3.4.1 Fully developed flow initial condition The analytical solution exists for the fully developed flow initial condition. The details can be found in Appendix A, and the results are given here. They are:

$$f_o = \frac{1}{4}(2r_c^2 - r_c^4) \quad (2.44)$$

$$\omega_o = \frac{2r_c}{R_o^3} \quad (2.45)$$

$$T_{lo} = \exp(-2Nu z) \frac{T^*(r_c)}{T^*(0)} \quad (2.46)$$

$$T_{so} = 1 - Su \frac{\exp(-2Nu z)}{T^*(0)} \left. \frac{dT^*}{dr_c} \right|_{r_c=1} \ln \left(\frac{1 - \epsilon_o}{1 - \epsilon_o r_s} \right) \quad (2.47)$$

$$\epsilon_o = 1 - \exp \left(\frac{1}{Su} \frac{T^*(0)}{\left. \frac{dT^*}{dr_c} \right|_{r_c=1}} \right) \quad (2.48)$$

where the subscript o indicates the analytical solution for the fully developed flow with the uniform ice layer. T^* is the temperature profile for the thermally fully developed flow and is the solution to the ordinary differential equation:

$$\frac{1}{r_c} \frac{d}{dr_c} \left(r_c \frac{dT^*}{dr_c} \right) = -2Nu(1 - r_c^2)T^* \quad (2.49)$$

subject to

$$\begin{aligned} \frac{dT^*}{dr_c} &= 0 \quad \text{at} \quad r_c = 0 \\ T^* &= 0 \quad \text{at} \quad r_c = 1. \end{aligned}$$

2.3.4.2 Developing flow initial condition The liquid temperature for the initial thin ice layer interval is nondimensionalized using boundary layer scale:

$$r_b = \frac{\bar{R} - \bar{r}}{\bar{\delta}} \quad \text{and} \quad \delta = \frac{\bar{\delta}}{\bar{R}}$$

where $\bar{\delta}$ is the thickness of the thermal boundary layer in the liquid phase. Boundary layer scale r_b varies from 0 at the solid-liquid interface to 1 at the thermal boundary layer edge. The dimensionless liquid temperature also varies from 0 to 1 within the boundary layer and is 1 in the core region, where liquid temperature is at the inlet temperature.

Since $\epsilon \rightarrow 0$ as $z \rightarrow 0$, the asymptotic solution for small z can be obtained by ignoring the effect of the thin ice layer. When the ice layer thickness is ignored, the hydrodynamic field can be assumed to be fully developed, and stream function and vorticity for small z can be approximated by the inlet condition. Also, the liquid temperature field becomes uncoupled from the solid temperature field and ice layer thickness and can be obtained simply by using the asymptotic stream function in boundary layer coordinates. This $z \rightarrow 0$ problem is the classical Graetz problem.

The solid temperature and the ice layer thickness for small z are obtained by solving solid energy equation and interface equation simultaneously using *a priori* asymptotic liquid temperature.

Asymptotic solution for small z The asymptotic solutions for dimensionless stream function and vorticity are (in core scale):

$$f_a = \frac{1}{4}(2r_c^2 - r_c^4) \quad (2.50)$$

$$\omega_a = 2r_c \quad (2.51)$$

where the subscript a indicates the asymptotic solution for small z . These solutions can be rewritten in boundary layer scale coordinates and they become

$$f_a(r_b, z) = \frac{1}{4} - \delta^2 r_b^2 \left(1 - \frac{1}{2}\delta r_b\right)^2 \quad (2.52)$$

$$\omega_a(r_b, z) = 2(1 - \delta r_b). \quad (2.53)$$

The z variation in boundary layer coordinates is implicit in dimensionless boundary layer thickness δ , which is given by:

$$\delta = (Cz)^{\frac{1}{3}}$$

where C is a free parameter.

The dimensionless liquid temperature is completely determined by:

$$\frac{\partial^2 T_{la}}{\partial r_b^2} - \left(\frac{\delta}{1 - \delta r_b} - r_b^2 \delta^2 \delta' (2 - \delta r_b) \right) \frac{\partial T_{la}}{\partial r_b} - r_b \delta^3 (2 - \delta r_b) \frac{\partial T_{la}}{\partial z} = 0 \quad (2.54)$$

subject to boundary condition:

$$T_{la} = 0 \text{ at } r_b = 0 \quad \text{and} \quad T_{la} \longrightarrow 1 \text{ as } r_b \longrightarrow \infty \quad (2.55)$$

and initial condition:

$$T_{la}^+(r_b) = 1.119847 \int_0^{\left(\frac{2}{9}C\right)^{\frac{1}{3}} r_b} \exp(-\zeta^3) d\zeta \quad (2.56)$$

where T_{la} indicates the asymptotic liquid temperature for small z . The superscript $+$ denotes that the solution is at $z = 0^+$. Equations (2.54) - (2.56) completely determine the asymptotic liquid temperature for small z .

The asymptotic solutions for dimensionless solid temperature and ice layer thickness are obtained from the following equations, using *a priori* asymptotic liquid temperature:

$$\frac{\partial^2 T_{sa}}{\partial r_s^2} - \frac{\epsilon_a}{1 - \epsilon_a} \frac{\partial T_{sa}}{\partial r_s} = 0 \quad (2.57)$$

$$\frac{\epsilon_a}{1 - \epsilon_a} = \frac{\left. \frac{\partial T_{sa}}{\partial r_s} \right|_{r_s=1}}{\left. \frac{\partial T_{la}}{\partial r_b} \right|_{r_b=0}} \frac{\delta}{Su}. \quad (2.58)$$

The boundary conditions are:

$$T_s = 0 \quad \text{at } r_s = 0 \quad \text{and} \quad T_s = 1 \quad \text{at } r_s = 1, \quad \text{for all } z \quad (2.59)$$

where the subscript a denotes the asymptotic solution. Equations (2.57) and (2.59) are solved simultaneously for T_{sa} and ϵ_a using previously calculated T_{la} . This concludes the determination of the asymptotic solution for small z .

Numerical solution for large z As z increases, ϵ increases as well. Ice layer grows to the same order of magnitude as the pipe radius. Then the effect of ice layer prevents the decoupling of hydrodynamic equations and energy equations. Therefore, for the thick ice layer interval, the solution must be obtained by solving all five governing equations simultaneously, and the solution can be obtained only by

using a numerical method. The governing equations and boundary conditions are the same as in Sections 2.3.2 and 2.3.3, except that all the unsteady terms are dropped. The initial condition for the thick ice layer interval at $z = z_{tr}$ is given by the solution from the thin ice layer interval.

3. NUMERICAL ANALYSIS

3.1 Numerical Method of Solution

Governing equations derived in Chapter 2 are discretized using a finite difference method. This converts the partial differential equations into a system of algebraic equations that is well-suited for computation on a computer. The coordinate transformation immobilizes the moving solid-liquid interface. This results in a rectangular computational domain. The computational domain is divided into a number of nodes or grid points. The dependent variables are calculated at each grid point, and collectively, the solution of the problem is obtained by solving the system of algebraic equations simultaneously. The high Pe assumption, as described in Chapter 2, is quite reasonable for the present study and greatly simplifies the resulting finite difference equations. The effects of keeping these terms are discussed later with numerical results. The essential features of the numerical method are adopted from Fant [54], as described in Section 3.1.2.

3.1.1 Clustered grid

The accuracy of the numerical solution depends on the spacing between grid points. When large gradients are present, it is essential that this spacing is kept sufficiently small to ensure a good approximation. However, the total number of grid

points are limited by the computational capacity. Consequently, the use of variable increment grids provides a means for minimizing the total number of grid points used and yet improving the overall accuracy of the method by locally clustering grid points where large gradients are expected to exist. However, it should be noted that the use of variable increments can result in a loss of formal truncation error in physical space [58].

For the liquid PCM region, the radial nodes are mildly clustered near the solid-liquid interface. This is done to provide increased resolution in the thermal and velocity boundary layers. The axial nodes are uniformly spaced. For the solid PCM region, both radial and axial nodes are uniformly spaced. Figure 3.1(a) shows a liquid PCM region mesh in which grid points are clustered near the solid-liquid interface in the radial direction while the spacing in the axial direction is uniform. There are 21 nodes in the axial direction with maximum and minimum spacings of 0.07185 and 0.02311, respectively (which corresponds to the case of $\beta = 1.2$ in Equation (3.1)). Because computation becomes more involved with the nonuniform grid spacings in the radial direction, it is more convenient to apply a transformation to the r_c -coordinate so that the governing equations can be solved on a uniformly-spaced grid in the computational plane (r, z) as seen in Figure 3.1(b).

The transformation for clustering nodes near the interface ($r_c = 1$) is obtained by setting $\alpha = 0$ in a general stretching transformation proposed by Roberts [55]. The radial transformation and its inverse are:

$$r = \frac{\ln\left(\frac{\beta+r_c}{\beta-r_c}\right)}{\ln\left(\frac{\beta+1}{\beta-1}\right)} \quad \text{and} \quad r_c = \frac{\beta\left(\frac{\beta+1}{\beta-1}\right)^r - \beta}{1 + \left(\frac{\beta+1}{\beta-1}\right)^r} \quad (3.1)$$

where r is the new stretched radial coordinate and β is the stretching parameter. As

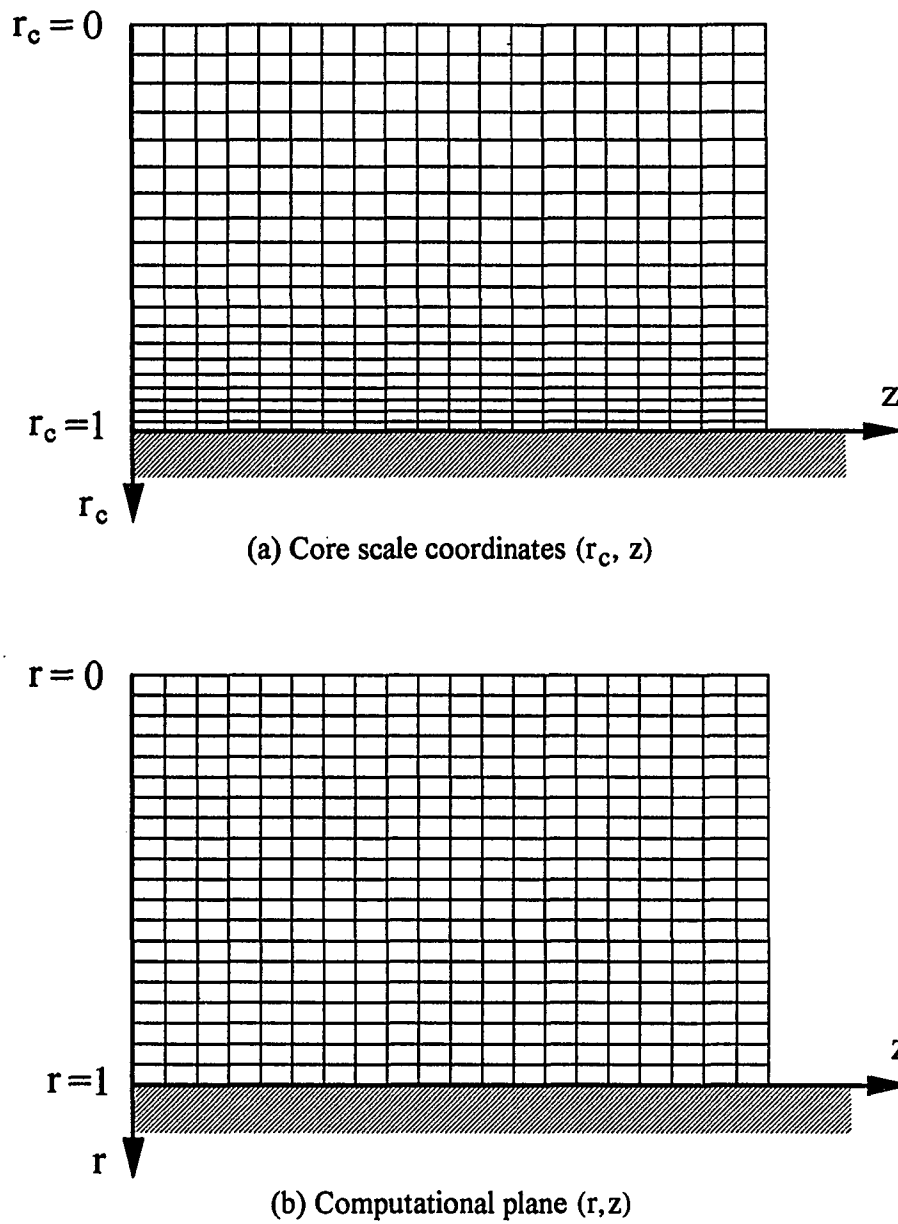


Figure 3.1: Grid clustering near the solid-liquid interface

Table 3.1: Maximum and minimum increments of nonuniform grids

β	Δr_{max}	Δr_{min}	$\frac{\Delta r_{max}}{\Delta r_{min}}$
100.00	0.025001 ^a	0.024998	1.0001
10.00	0.025084	0.024839	1.0098
2.00	0.027464	0.020740	1.3242
1.50	0.030173	0.016991	1.7759
1.20	0.035958	0.011268	3.1910
1.10	0.041842	0.007522	5.5627
1.05	0.048706	0.004737	10.2809

^aIncrement for the uniform grid is 0.025 for nr=40.

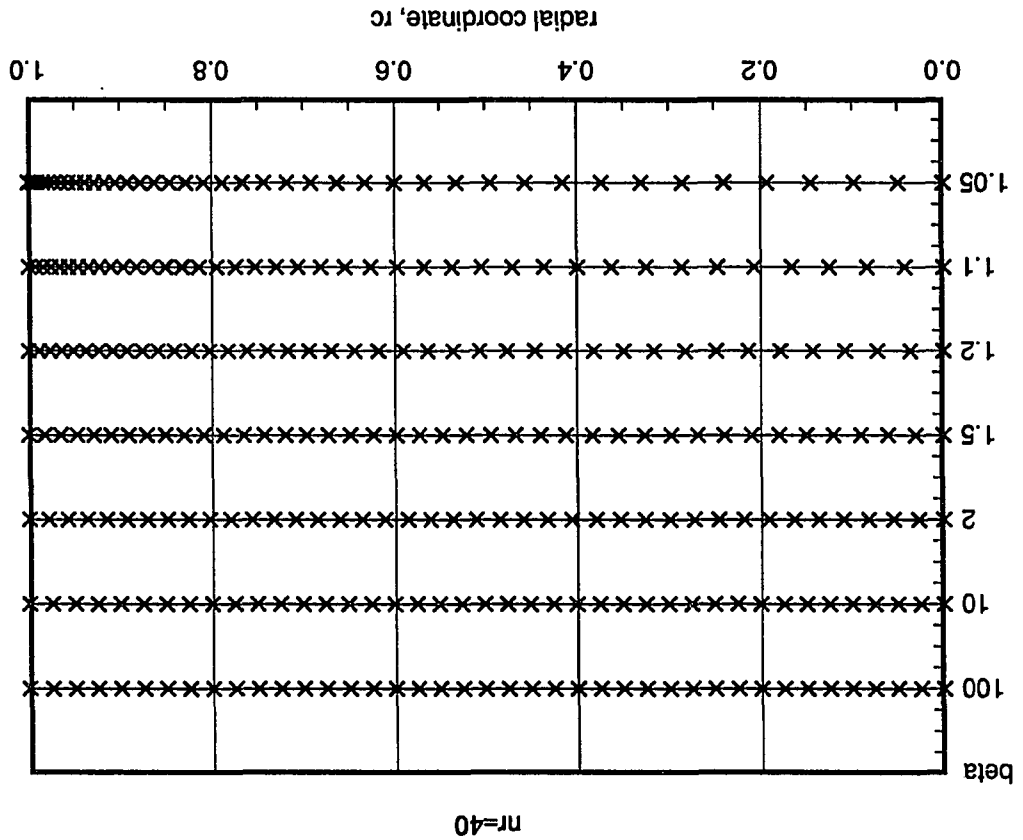
β approaches 1, a uniform grid in the stretched coordinate system r becomes highly clustered near the interface in the core coordinate system r_c . Figure 3.2 shows the nonuniform grid spacings for a number of values of the stretching parameter β . The number of grid points in this plot is 41. The maximum and minimum increments corresponding to β 's used in Figure 3.2 are listed in Table 3.1. For $\beta \geq 10.0$, the grids are almost uniform, whereas the ratio of maximum to minimum increment increases as β decreases, up to more than 10.0 for $\beta = 1.05$. As the grid is clustered near the wall, the grid spacings at the center increase; therefore, the optimum value of β should be chosen based on the overall performance of the grid. The effects of β upon the numerical solution will be discussed in Section 3.3.

Using this transformation, the governing equations are converted into

$$X^2 \frac{\partial^2 f}{\partial r^2} + \left(Y - \frac{1}{r_c} \right) X \frac{\partial f}{\partial r} + r_c R^3 \omega = 0 \quad (3.2)$$

$$-\frac{R^2}{\lambda Pr} \frac{\partial \omega}{\partial t} + X^2 \frac{\partial^2 \omega}{\partial r^2} + \left(Y + \frac{1}{r_c} + \frac{1}{r_c Pr} \frac{\partial f}{\partial z} + \frac{r_c R \dot{R}}{\lambda Pr} \right) X \frac{\partial \omega}{\partial r} - \frac{1}{r_c Pr} X \frac{\partial f}{\partial r} \frac{\partial \omega}{\partial z} - \frac{\omega}{r_c^2 Pr} \left(\frac{\partial f}{\partial z} - r_c \frac{R'}{R} X \frac{\partial f}{\partial r} \right) - \frac{\omega}{r_c^2} = 0 \quad (3.3)$$

Figure 3.2: Nonuniform grid spacings for various stretching parameter β



$$-\frac{R^2}{\lambda} \frac{\partial T_l}{\partial t} + X^2 \frac{\partial^2 T_l}{\partial r^2} + \left(Y + \frac{1}{r_c} + \frac{1}{r_c} \frac{\partial f}{\partial z} + \frac{r_c R \dot{R}}{\lambda} \right) X \frac{\partial T_l}{\partial r} - \frac{1}{r_c} X \frac{\partial f}{\partial r} \frac{\partial T_l}{\partial z} = 0 \quad (3.4)$$

$$-\epsilon^2 \frac{\partial T_s}{\partial t} + \frac{\partial^2 T_s}{\partial r_s^2} - \left(\frac{\epsilon}{1 - \epsilon r_s} - r_s \epsilon \dot{\epsilon} \right) \frac{\partial T_s}{\partial r_s} = 0 \quad (3.5)$$

$$\frac{\partial \epsilon}{\partial t} = Ste \left(\frac{Su}{1 - \epsilon} X \frac{\partial T_l}{\partial r} \Big|_{r=1} + \frac{1}{\epsilon} \frac{\partial T_s}{\partial r_s} \Big|_{r_s=1} \right) \quad (3.6)$$

where

$$X = \frac{2\beta}{(\beta^2 - r_c^2) \ln\left(\frac{\beta+1}{\beta-1}\right)} \quad \text{and} \quad Y = \frac{2r_c}{(\beta^2 - r_c^2)},$$

and they appear from the transformation of radial derivatives such as

$$\frac{\partial}{\partial r_c} = X \frac{\partial}{\partial r}$$

$$\frac{\partial^2}{\partial r_c^2} = X^2 \frac{\partial^2}{\partial r^2} + XY \frac{\partial}{\partial r}.$$

Here X is the metric for the coordinate transformation. Y , appearing in the second-order derivative, has no physical meaning, and it is just a term defined so for convenience.

3.1.2 Finite differencing

A notable finite differencing is a corrected second-order difference scheme used for convective terms in the governing equations. It splits first-order partial derivatives into first-order upwind difference and correction terms which result in a second-order accurate central or upwind difference. If only the first terms are used, a first-order accurate upwind difference results. It has the advantages of the stability of an upwind difference method and the accuracy possessed by a central difference method when the resulting second-order difference is central. The technique has been adopted

successfully by Prusa [56] and others [57, 54]. A similar finite differencing is adopted in the present study.

The indices used for a finite difference formula are defined as follows: n designates the time level at which a dependent variable is evaluated, and i and j are indices for radial and axial coordinates that range from 0 to nr and nz , respectively. For solid phase region, i varies from 0 to ns .

The corrected second-order differencing used for convective terms are:

$$\text{one-sided: } 2D \frac{\partial \phi}{\partial z} = (D - |D|) \left\{ \frac{\phi_{i,j} - \phi_{i,j-1}}{\Delta z} + \frac{\phi_{i,j} - 2\phi_{i,j-1} + \phi_{i,j-2}}{2\Delta z} \right\} \\ + (D + |D|) \left\{ \frac{\phi_{i,j+1} - \phi_{i,j}}{\Delta z} - \frac{\phi_{i,j} - 2\phi_{i,j+1} + \phi_{i,j+2}}{2\Delta z} \right\}$$

$$\text{central: } 2C \frac{\partial \phi}{\partial r} = (C - |C|) \left\{ \frac{\phi_{i,j} - \phi_{i-1,j}}{\Delta r} + \frac{\phi_{i+1,j} - 2\phi_{i,j} + \phi_{i-1,j}}{2\Delta r} \right\} \\ + (C + |C|) \left\{ \frac{\phi_{i+1,j} - \phi_{i,j}}{\Delta r} - \frac{\phi_{i+1,j} - 2\phi_{i,j} + \phi_{i-1,j}}{2\Delta r} \right\}.$$

When only the first terms in the braces are used, they are first-order one-sided differences. However, when correction terms are added, the resulting differences are second-order central (for the radial coordinate) and second-order one-sided (for the axial coordinate), respectively.

The unsteady terms and diffusion terms are differenced using standard forward-difference and second-order central difference formulas, respectively. The derivatives appearing in the coefficients of convection terms are differenced using the standard second-order central difference formula for the radial coordinate, and one-sided (first or second order) difference formula for the axial coordinate.

3.1.2.1 Governing equations The governing equations for f , ω , T_l , and T_s in stretched coordinates are arranged in the following general form:

$$A \frac{\partial \phi}{\partial t} + B \frac{\partial^2 \phi}{\partial r^2} + 2C \frac{\partial \phi}{\partial r} + 2D \frac{\partial \phi}{\partial z} + E = 0 \quad (3.7)$$

where

$$A = \begin{cases} 0 & \text{for } \phi = f \\ -\frac{R^2}{\lambda Pr} & \text{for } \phi = \omega \\ -\frac{R^2}{\lambda} & \text{for } \phi = T_l \\ -\epsilon^2 & \text{for } \phi = T_s \end{cases}$$

$$B = \begin{cases} X^2 & \text{for } \phi = f, \omega, T_l \\ 1 & \text{for } \phi = T_s \end{cases}$$

$$2C = \begin{cases} (Y - \frac{1}{r_c})X & \text{for } \phi = f \\ (Y + \frac{1}{r_c} + \frac{1}{r_c Pr} \frac{\partial f}{\partial z} + \frac{r_c R \dot{R}}{\lambda Pr})X & \text{for } \phi = \omega \\ (Y + \frac{1}{r_c} + \frac{1}{r_c} \frac{\partial f}{\partial z} + \frac{r_c R \dot{R}}{\lambda})X & \text{for } \phi = T_l \\ -(\frac{\epsilon}{1 - \epsilon r_s} - r_s \epsilon \dot{\epsilon}) & \text{for } \phi = T_s \end{cases}$$

$$2D = \begin{cases} 0 & \text{for } \phi = f, T_s \\ -\frac{1}{r_c Pr} X \frac{\partial f}{\partial r} & \text{for } \phi = \omega \\ -\frac{1}{r_c} X \frac{\partial f}{\partial r} & \text{for } \phi = T_l \end{cases}$$

$$E = \begin{cases} r_c R^3 \omega & \text{for } \phi = f \\ -\frac{\omega}{r_c^2 Pr} (\frac{\partial f}{\partial z} - r_c \frac{R'}{R} X \frac{\partial f}{\partial r}) - \frac{\omega}{r_c^2} & \text{for } \phi = \omega \\ 0 & \text{for } \phi = T_l, T_s. \end{cases}$$

Applying the finite difference formulas, these equations are converted into finite difference equations of the form:

$$C_0\phi_{i,j}^{n+1} = \frac{A}{\Delta t}\phi_{i,j}^n + C_1\phi_{i+1,j}^{n+1} + C_2\phi_{i,j+1}^{n+1} + C_3\phi_{i-1,j}^{n+1} + C_4\phi_{i,j-1}^{n+1} - E + F + G \quad (3.8)$$

where

$$C_0 = \left(\frac{A}{\Delta t} - \frac{2B}{\Delta r^2} - \frac{2|C|}{\Delta r} - \frac{2|D|}{\Delta z} \right)$$

$$C_1 = - \left(\frac{B}{\Delta r^2} + \frac{C+|C|}{\Delta r} \right)$$

$$C_2 = - \left(\frac{D+|D|}{\Delta z} \right)$$

$$C_3 = - \left(\frac{B}{\Delta r^2} - \frac{C-|C|}{\Delta r} \right)$$

$$C_4 = \frac{D-|D|}{\Delta z}$$

$$F = |C| \frac{\phi_{i+1,j}^{n+1} - 2\phi_{i,j}^{n+1} + \phi_{i-1,j}^{n+1}}{\Delta r}$$

$$G = |D| \frac{\phi_{i,j}^{n+1}}{\Delta z} + (D-|D|) \left(\frac{\phi_{i,j-1}^{n+1}}{\Delta z} - \frac{\phi_{i,j-2}^{n+1}}{2\Delta z} \right) - (D+|D|) \left(\frac{\phi_{i,j+1}^{n+1}}{\Delta z} - \frac{\phi_{i,j+2}^{n+1}}{2\Delta z} \right).$$

The solid-liquid interface equation is differenced as:

$$\epsilon^{n+1} = \epsilon^n + \Delta t Ste \left(\frac{Su}{1-\epsilon} X \frac{3T_{lnr,j}^{n+1} - 4T_{lnr-1,j}^{n+1} + T_{lnr-2,j}^{n+1}}{2\Delta r} + \frac{1}{\epsilon} \frac{3T_{sns,j}^{n+1} - 4T_{sns-1,j}^{n+1} + T_{sns-2,j}^{n+1}}{2\Delta r_s} \right). \quad (3.9)$$

3.1.2.2 Boundary conditions The finite-difference form of the boundary conditions are obtained by the substitution of finite difference formulas into Equations (2.37) - (2.40). Thus, the radial boundary conditions are (for all j):

$$f_{0,j} = 0 \quad \text{and} \quad f_{nr,j} = \frac{1}{4} \quad (3.10)$$

$$\omega_{0,j} = 0 \quad \text{and} \quad \omega_{nr,j} = -\frac{1}{R^3} \frac{2(f_{nr-1,j} - f_{nr,j})}{\Delta r^2} X^2 \quad (3.11)$$

$$T_{l0,j} = \frac{4T_{l1,j} - T_{l2,j}}{3} \quad \text{and} \quad T_{lnr,j} = 0 \quad (3.12)$$

$$T_{s0,j} = 0 \quad \text{and} \quad T_{sns,j} = 1. \quad (3.13)$$

The vorticity boundary condition at the solid-liquid interface is a first-order, one-sided difference obtained from Taylor series expansions by using the no-slip boundary condition at the interface. Second-order differencing has also been derived similarly but proves less accurate (see Section 3.3). The liquid temperature boundary condition at the center is the standard second-order, one-sided differencing.

3.2 Computational Procedure

The finite difference equations in the preceding section are solved using the fully implicit, point iterative, Gauss-Seidel method. The dependent variables in a given time level are calculated by repeated iterations of the finite difference equations. Once the iterations at a given time level converge to a numerical solution, the time level is advanced, and the iterations begin anew for the new time level. All that is required are the values of the dependent variables at the old or preceding time level. For the first time level, at $t = \Delta t$, the old values of the dependent variables are the initial conditions.

The equations are numerically iterated in the following sequence:

1. solid-liquid interface equation
2. solid temperature equation
3. liquid temperature equation
4. vorticity equation
5. stream function equation.

This sequence is repeated until the iterations converge to within a prescribed tolerance. Iterations are considered to have converged to a numerical solution if the following conditions are satisfied throughout the computational domain.

For $\phi = \epsilon, T_s, T_l,$ and f :

$$|\phi^{k+1} - \phi^k| < \tau$$

For $\phi = \omega$:

$$\left| \frac{\phi^{k+1} - \phi^k}{\max(\phi^{k+1})} \right| < \tau$$

where k refers to the iteration number during one time step and τ is the prescribed tolerance.

During the freezing process, the solid and liquid temperature magnitudes range between zero and unity. The solid-liquid interface and stream function also take on values of order one. However, the vorticity varies in a wider range. To ensure that the solution converges to the same number of significant digits throughout the freezing process, the differences in the magnitude of vorticity between two consecutive iterations are normalized by the maximum values at that iteration level.

The computation for the present study consists of two steps: the initial steady state calculation and the transient calculation. The initial steady states are described in Appendix A. The numerical model first calculates initial conditions and then transient calculation starts with a change of boundary conditions. For the developed initial condition, the wall temperature which is initially exponentially increasing in the axial direction is changed to a uniform temperature. More freezing occurs in a farther axial location due to the lowered wall temperature. For the developing initial condition, transient calculation begins with the onset of disturbance at the exit of the test section.

3.3 Dimensionless Parameters

The dimensionless parameters that characterize the numerical solution of the present study can be separated into two different categories. The first category contains the physical parameters which are part of the problem: Pr , λ , Ste , Su , and z_{max} . The second category contains the computational parameters which are associated with the numerical formulation and solution of the problem: the number of radial nodes in solid and liquid regions, ns , nr ; number of axial nodes, nz ; the size of the time step, Δt ; stretching parameter, β ; and the convergence tolerance, τ . Additional parameters are relaxation parameters which usually underrelax dependent variables at iteration levels. All these parameters affect the numerical results more or less.

The effects of nr and β could be addressed briefly as an example. Table 3.2 lists the vorticity values at $r = 1$ for the fully developed flow using different computational parameters. Analytically, the vorticity at $r = 1$ is 2. A second-order ω boundary

Table 3.2: Vorticity boundary condition at the pipe wall

	first-order ω B.C.		second-order ω B.C.	
	$nr = 20$	$nr = 40$	$nr = 20$	$nr = 40$
$\beta = 100$	1.98756	1.99688	1.99740	1.99936
$\beta = 1.5$	1.99591	1.99898	1.99363	1.99836
$\beta = 1.2$	1.99645	1.99912	NA ^a	1.99740
$\beta = 1.1$	1.99300	1.99827	NA	NA
$\beta = 1.05$	1.98667	1.99669	NA	NA

^aNot available because solution did not converge.

condition gives the best result when $nr = 40$ and $\beta = 100$, which is almost a uniform grid. As the stretching increases, the vorticity value at the boundary first deteriorates and then finally diverges. On the other hand, a first-order ω boundary condition gives the best result when the stretching is moderate ($nr = 40$ and $\beta = 1.2$). For the clustered grid used in this study, the first-order boundary condition gives better results than the second-order boundary condition.

Computational parameters used for the present study vary depending on the simulation scenario. In particular, calculations using the fully developed initial condition and developing initial condition require different values for the various computational parameters. In general, the following computational parameters are used unless mentioned otherwise:

$$\begin{array}{lll}
 ns = 20 & nr = 30 & nz = 20 \\
 \Delta t = 0.05 & \beta = 1.2 & \tau = 10^{-6}.
 \end{array}$$

The study is essentially to investigate the effects of physical parameters in freezing problem in a pipe flow. In particular, Ste , Su , and z_{max} are varied to represent different freezing conditions, whereas λ and Pr are fixed for a specific fluid (*i.e.*,

water). The length of the pipe or test section, z_{max} , is associated with the initial condition. For a fully developed initial condition, a rather large value of z_{max} is used to represent a long pipe, whereas smaller value is generally used for a developing flow initial condition, which occurs near the inlet of the pipe. Typically, $z_{max} = 0.5$ is used for the simulation with the fully developed flow initial condition, and $z_{max} = 0.05$ is used for the developing flow initial condition. For the transient calculation with the developing flow initial condition, an even smaller value is used to simulate the experiments in the laboratory. In this case, $z_{max} = 0.005$ approximates the length of the pipe commonly used in real experiments found in literature [42, 43].

4. RESULTS AND DISCUSSION

Results obtained using the numerical model developed in this study are presented and discussed in this chapter. The study on the freezing problem in a pipe flow, in general, is interested in three major results: the steady or transient ice layer profile, its effects on heat transfer, and its effects upon hydrodynamic field, such as pressure drop. The growth of ice layer and its steady-state profile are affected mostly by the thermal field of the fluid flow. Therefore, this study considered two interesting flow conditions as initial conditions: fully developed flow and thermally developing flow. They are extreme cases for the thermal field in the pipe flow. These initial conditions are described in detail in Appendix A. The fully developed initial condition is appropriate far downstream from the thermal entrance, where the fluid flow approaches thermally fully developed flow. As a result, the fully developed initial condition is more appropriate for a long pipe, where thermal entrance region is not as important. For a short pipe, where the thermal entrance region is important, the developing initial condition is more appropriate. Results using two different initial conditions are presented separately. For both types of results, $Pr = 10$ and $\lambda = 1.0$ were used for all computations.

4.1 Results Using Fully Developed Flow Initial Condition

This initial condition has a uniform ice layer with hydrodynamic and thermal fields fully developed. The initially uniform ice layer thickness, ϵ_0 , can be calculated using Equation (A.30). The initial radius of the solid-liquid interface, $R_0 = 1 - \epsilon_0$, is tabulated for a range of Su in Table A.2. The solid and liquid temperatures vary exponentially along the axial direction (see Appendix A, Section A.2.3). During a ramping time of a few time steps, the wall temperature is changed to a uniform distribution equal to the wall temperature at the inlet. This decrease in the wall temperature leads to additional growth of the ice layer until a new final steady state is reached. Departures of the ice layer from a uniform thickness force the flow to become both hydrodynamically and thermally developing. Nevertheless, departures from fully developed flow in the final state are not large. Therefore, this case is more appropriate for a long pipe, where thermal entrance region is not as important. The range of the axial coordinate used in this initial condition is $0 \leq z \leq 0.05$ or 0.5 , representing a long pipe.

4.1.1 Time for transient freezing

Due to the change in pipe wall temperature, a new ice layer starts to grow on top of the initial one. The ice growth may or may not completely block the fluid flow. If there is no fluid flow, the freezing in a pipe is one-dimensional, and complete freezing to the center of the pipe occurs if the pipe wall is below the freezing temperature. When there is fluid flow, however, whether the ice grows to the center or not depends on the amount of superheat which the liquid at the inlet carries, as well as the flow rate. For a given flow rate, if a liquid has sufficient superheat, the ice layer will grow

Table 4.1: Effects of λ on freezing time and final steady state

λ	Ste	Su	t_{95}	ϵ_o	ϵ_f
0.1	0.100	1.0	4.5959	0.6272	0.7492
0.1	0.100	2.0	4.7224	0.3905	0.5054
0.1	0.100	5.0	2.3754	0.1798	0.2469
0.1	0.100	10.0	1.2818	0.0943	0.1324
0.1	0.100	20.0	0.7651	0.0483	0.0686
1.0	0.100	1.0	4.4285	0.6272	0.7493
1.0	0.100	2.0	4.1219	0.3905	0.5055
1.0	0.100	5.0	1.5900	0.1798	0.2470
1.0	0.100	10.0	0.5325	0.0943	0.1325
1.0	0.100	20.0	0.2060	0.0483	0.0686
10.0	0.100	1.0	4.0263	0.6272	0.7492
10.0	0.100	2.0	3.6661	0.3905	0.5054
10.0	0.100	5.0	1.3388	0.1798	0.2469
10.0	0.100	10.0	0.4621	0.0943	0.1325
10.0	0.100	20.0	0.1533	0.0483	0.0686

asymptotically into a new steady state with somewhat thicker ice. With insufficient superheat, the pipe will be frozen shut, however. The flow rate is represented in this study by pressure gradient, G . In the dimensionless formulation, it appears in the Pe and the characteristic scales for stream function and vorticity. Since all Pe terms are dropped, the flow rate does not appear explicitly.

The time scale for the asymptotic growth case (high Su) has been calculated by the time required to reach 95% of the total ice growth. This is because the final steady state is only approached asymptotically, which means it takes infinite time to reach the real steady state. The rate of the ice growth depends on λ , Ste , and Su ; however, the effect of λ is not as significant as those of Ste and Su . Table 4.1 shows the effect of λ on freezing time and final steady-state ice thickness. Ste was kept constant to focus on the effects of λ and Su . As λ decreased, the freezing time

increased. For $Su = 2.0$, two order of magnitude decrease in λ increased t_{95} by 28.8%, while a 177% increase resulted for $Su = 10.0$. Compared to this, a one order of magnitude change in the value of Su (from 10.0 to 1.0) resulted in a 259% increase for $\lambda = 0.1$ and a 771% increase for $\lambda = 10.0$. Therefore, λ has a much smaller effect than Su on the *rate* of freezing. The effects of λ upon the steady-steady ice layer profile is almost zero as shown in Table 4.1. Su solely determines the final amount of ice at steady state. This effect will be discussed in more detail in the following section. In this section, the time required to reach 95% of the total ice growth, t_{95} , is used to compare the effects of Ste and Su upon the freezing rate of a flowing liquid in a pipe.

Figure 4.1 shows the log-log plot of the freezing time (t_{95}) versus Ste for a range of Su . As Ste decreases, the curve becomes linear. A regression analysis for small Ste gives the following result

$$\lim_{Ste \rightarrow 0} t_{95} = C_1 \cdot Ste^{-0.98}$$

where C_1 is a function of Su . This correlation may be compared with

$$t_f = \frac{1}{4Ste} + \frac{1}{4}$$

which was determined by Riley *et al.* [59], using the method of matched asymptotic expansions, for the complete freezing time (t_f) of a non-flowing liquid in a circular cylinder initially at the freezing temperature. Despite the lack of fluid flow and liquid superheat, the correlations between the freezing time and Ste are similar to each other and suggest that the freezing time (t_{95}) is exactly inversely proportional to Ste in the limit $Ste \rightarrow 0$, indicating that a higher Ste results in a shorter freezing time.

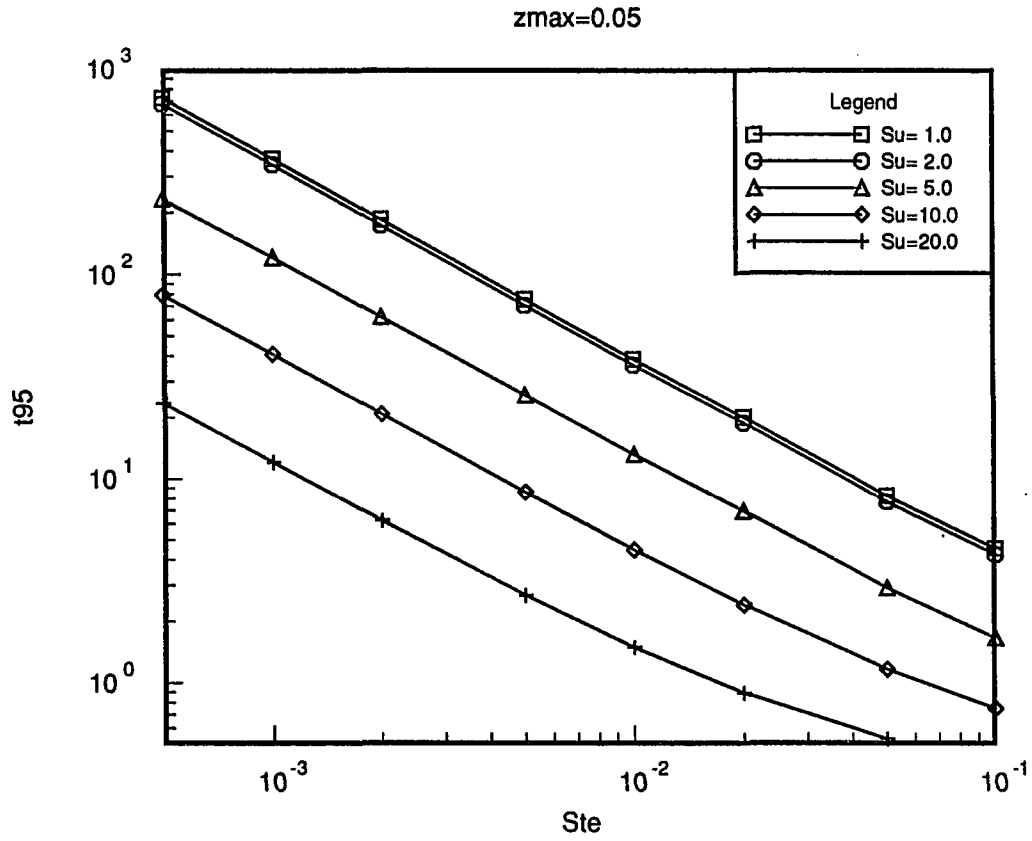


Figure 4.1: Freezing time (t_{95}) as a function of Ste

For a given Ste , a similar trend has been observed between t_{95} and Su but with different limiting conditions. The curve becomes linear as Su increases and Ste decreases. The slope of the line is steeper than that of t_{95} versus Ste . The relation can be given by

$$\lim_{Su \rightarrow \infty} \lim_{Ste \rightarrow 0} t_{95} = C_2 \cdot Su^n$$

where C_2 and n have been calculated to be $1.91 \times Ste^{-1.04}$ and -1.80 , respectively. Once again, this result suggests that t_{95} is exactly inversely proportional to Ste . This result contrasts with the conduction result in which it takes less time to freeze a liquid with a smaller Su . In such a case, a non-flowing liquid in a pipe with the isothermal wall below the freezing temperature is completely frozen up to the center. For the case of ice growth with fluid flow, however, it seems to take more time to reach the asymptotic steady state for smaller Su because the amount of ice growth is greater, thus requiring a greater amount of time to reach the asymptotic thickness. Hence longer time is required for the complete freezing case of the higher Su .

4.1.2 Final steady-state ice layer profile

The initially uniform ice layer grows asymptotically to a final steady state in time. Figure 4.2 shows these steady-state ice layer profiles for various Su 's. $z_{max} = 0.05$ was used for these results, in which the ice layer profiles are almost linear. These final ice layer profiles are independent of λ and Ste because these parameters affect the freezing rate or freezing time but do not change the steady-state ice layer thickness. In general, for smaller Su the ice layer thickness is greater. This occurs because for the smaller Su cases, less sensible cooling is needed to get the liquid down to the freezing temperature. It is shown that the amount of ice thickness increase

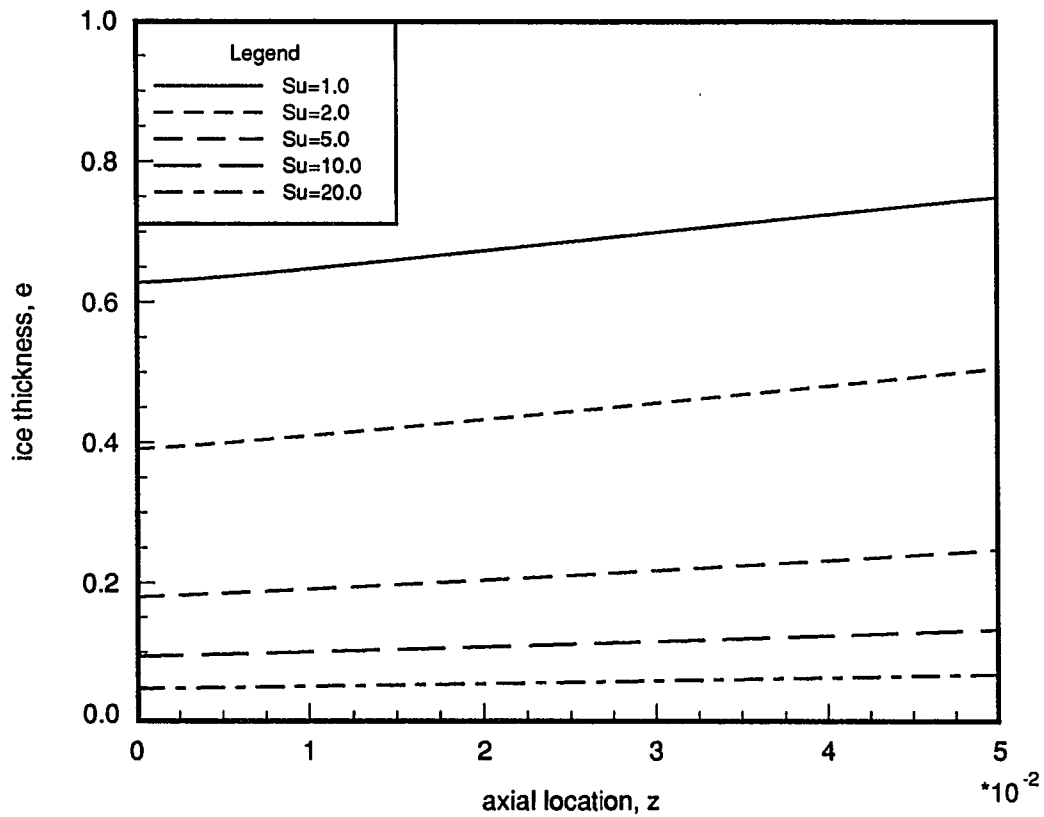


Figure 4.2: Steady-state ice layer profiles (almost linear) from the fully developed flow initial condition ($z_{max} = 0.05$)

along the test section is small when the ice layer is thin ($Su = 20.0$) and is larger when the ice layer is thicker (for smaller Su). This indicates that the local amount of ice growth may increase in the axial direction. This can be readily shown from the ice layer profiles in Figure 4.3, in which a longer test section was used ($z_{max} = 0.5$). For $Su = 20$, the local amount of ice growth is small for small z and it increases gradually in the axial direction making the ice layer profile concave. For larger z , the ice layer becomes almost linear in z , and the slope of the ice profile starts to decrease, making the profile convex as the ice layer grows very thick (large z for $Su = 5.0$). When the ice grows very thick, the ice growth is retarded, as shown in the upper right corner of Figure 4.3. It should be pointed out that this prediction is not physically valid where the ice grows so thick that the constant flow condition may not be maintained (recall the constant flow rate is assumed in the present model).

The ice layer profiles shown in Figure 4.3 appear self-similar to one another. If the ice layer profile of the $Su = 5.0$ case is translated to the right, on top of the other two profiles, they appear almost identical except for the very large z region. The self-similarity is greater for larger Su cases. In order to use only one ice-layer profile to represent all Su cases, the axial distance at which an ice layer thickness of $\epsilon = 0.40$ occurred was measured. The results are listed in Table 4.2 with corresponding Su 's. The distances between these locations are also listed and are found to be almost equidistant. The difference of the distances is only 1.4% within the accuracy of the measurement. An average axial displacement Δz of 0.095 becomes the measure of Su doubled (when moved to the right) or halved (when moved to the left). In general, using the $Su = 10$ profile in Figure 4.3 as the base case, other Su cases may be found

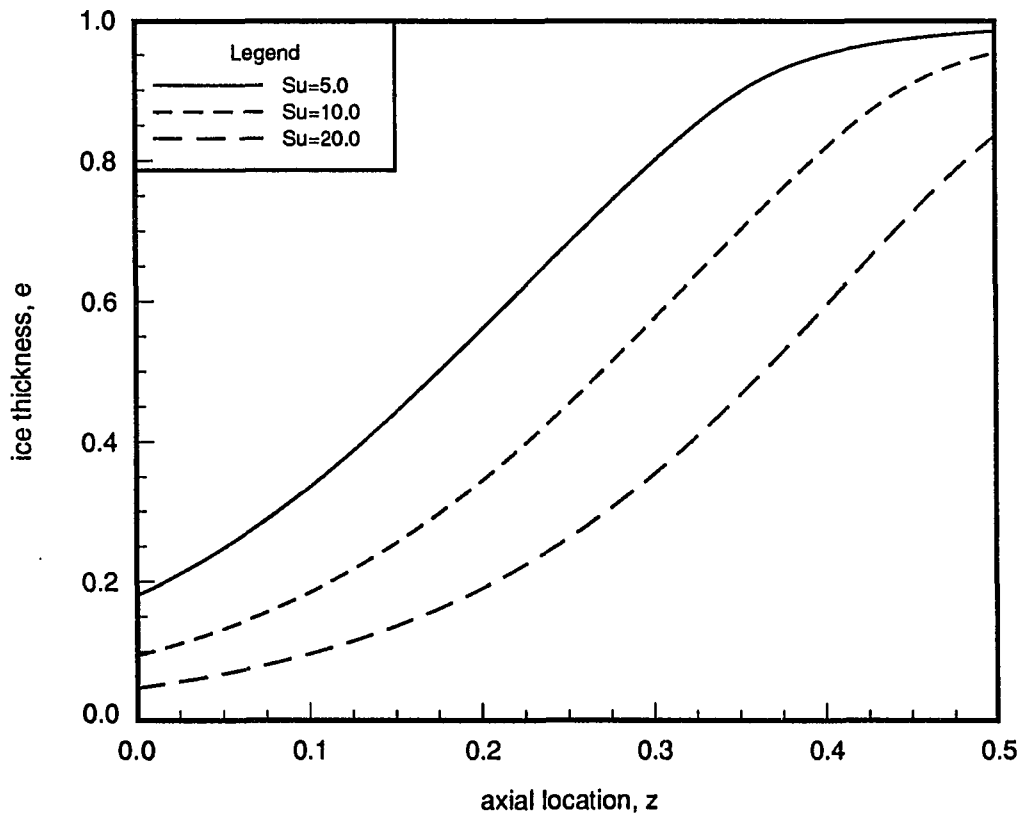


Figure 4.3: Steady-state ice layer profiles from the fully developed flow initial condition ($z_{max} = 0.5$)

Table 4.2: Self-similar ice layer profiles: Location of 40% ice layer thickness

$Su = 5$		$Su = 10$		$Su = 20$
$z = 0.1309$	distance	$z = 0.2253$	distance	$z = 0.3210$
	0.0944		0.0957	

by translating the $Su = 10$ profile by Δz units to the right, where

$$\Delta z = .095 \times \log_2(Su/10) = 0.137 \times \ln(Su/10).$$

In order to examine the effects of internal freezing on the ice layer profile upon a hydrodynamic field, some parameters are defined here. First, the average radius of the solid-liquid interface at the final steady state, R^* , is calculated on the basis of flow passage volume as follows. The average of the flow passage radius is calculated using the integral of cross-sectional area over the pipe length. It results in

$$R^* = \sqrt{\frac{1}{z_{max}} \int_0^{z_{max}} R^2 dz} \quad (4.1)$$

where the integral is evaluated using the trapezoidal rule. The average ice thickness of the final steady-state ice layer, ϵ^* , is then calculated from $\epsilon^* = 1 - R^*$, where 1 is the dimensionless pipe radius. The amount of reduction in the flow passage radius is denoted by ΔR and given as

$$\Delta R = R(z = 0) - R(z_{max}).$$

The percent reduction of the radius of the flow passage along the test section, ϕ_R , is defined as

$$\phi_R = \frac{\Delta R}{R^*}.$$

Table 4.3: Reduction of the flow passage for the fully developed flow

Su	R_o	R^*	ΔR	ϕ_R (%)	ΔR^*
1.0	0.3728	0.3161	0.1221	38.63	0.03818
2.0	0.6095	0.5559	0.1150	20.70	0.03542
5.0	0.8202	0.7888	0.0672	8.52	0.02048
10.0	0.9057	0.8878	0.0381	4.30	0.01158
20.0	0.9517	0.9421	0.0203	2.16	0.00616

Another parameter which indicates the variance of the radius from the average radius is defined similarly to standard deviation as

$$\Delta R^* = \sqrt{\frac{1}{nz+1} \sum_{j=0}^{nz} (R - R^*)^2} \quad (4.2)$$

where $nz + 1$ is the number of axial nodes along the pipe length. Some of these parameters are plotted versus Su on a log-log scale, as shown in Figure 4.4. It shows that the curve of the percent reduction versus Su on a log-log plot becomes linear as Su increases, which indicates that they are inversely proportional. This behavior can be expressed as follows:

$$\lim_{Su \rightarrow \infty} \phi_R = \frac{C}{Su}$$

where C is found to be 0.40 for the given length of the test section. Table 4.3 lists the initial radius (R_o), the amount of flow passage radius reduction (ΔR), the average radius (R^*), and the percent reduction (ϕ_R) for the Su cases shown in Figure 4.2 and Figure 4.4.

4.1.3 Heat transfer

It is interesting to look into the effect of the ice layer growth on heat transfer. This can be done easily by comparing Nusselt numbers between the uniform passage

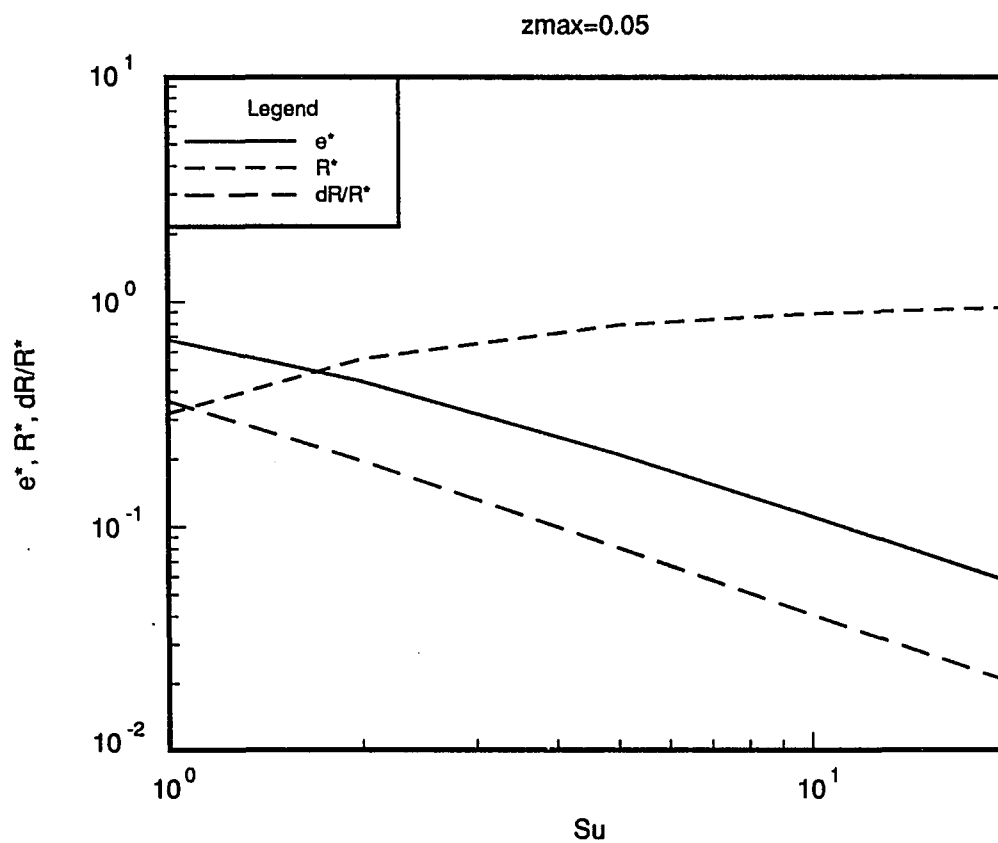


Figure 4.4: Average values of ice thickness and the radius of solid-liquid interface at the final steady state and the percent reduction of the flow passage radius versus Su for short pipe lengths

flow and converging passage flow due to the axial ice growth. The local Nusselt number has been defined in this study as

$$Nu_z = \frac{h_z (2\bar{R})}{k_l} = -\frac{2}{T_m} \left. \frac{\partial T_l}{\partial r_c} \right|_{r_c=1}$$

where h_z is the local convection heat transfer coefficient (see Appendix A, Equation (A.55)). The right side expression is used to calculate the local Nusselt number. Here T_m is the dimensionless bulk mean temperature, which is defined as

$$T_m = \frac{\bar{T}_m - T_o}{T_{io} - T_o} = 4 \int_0^1 T_l (1 - r_c^2) r_c dr_c$$

where \bar{T}_m is the bulk mean temperature of the liquid PCM (see Appendix A). The dimensionless bulk mean temperature decreases exponentially as shown in Figure 4.5. The inlet dimensionless bulk mean temperatures for all Su 's are the same as 0.5527. This is because the definition of Su is based on the inlet water temperature at the centerline, and the bulk mean temperature of the bell-shaped temperature profile is that fraction of the centerline temperature. Also shown in Figure 4.5, local liquid temperature drop is identical for all Su ($z \leq 0.2$), which indicates that the fluid flow is thermally fully developed even though the flow passage is converging, provided that the ice layer is thin. As mentioned in the previous section, it is shown that a 50% drop of inlet water temperature occurs just short of $z = 0.1$. This can be compared with the analytical solution for the bulk mean temperature of the thermally fully developed flow. From Appendix A, the dimensionless bulk mean temperature is given by

$$T_m = \frac{\exp(-2Nu z)}{1.8026}$$

where Nu is 3.6568 for the fully developed flow [13]. The axial distance at which

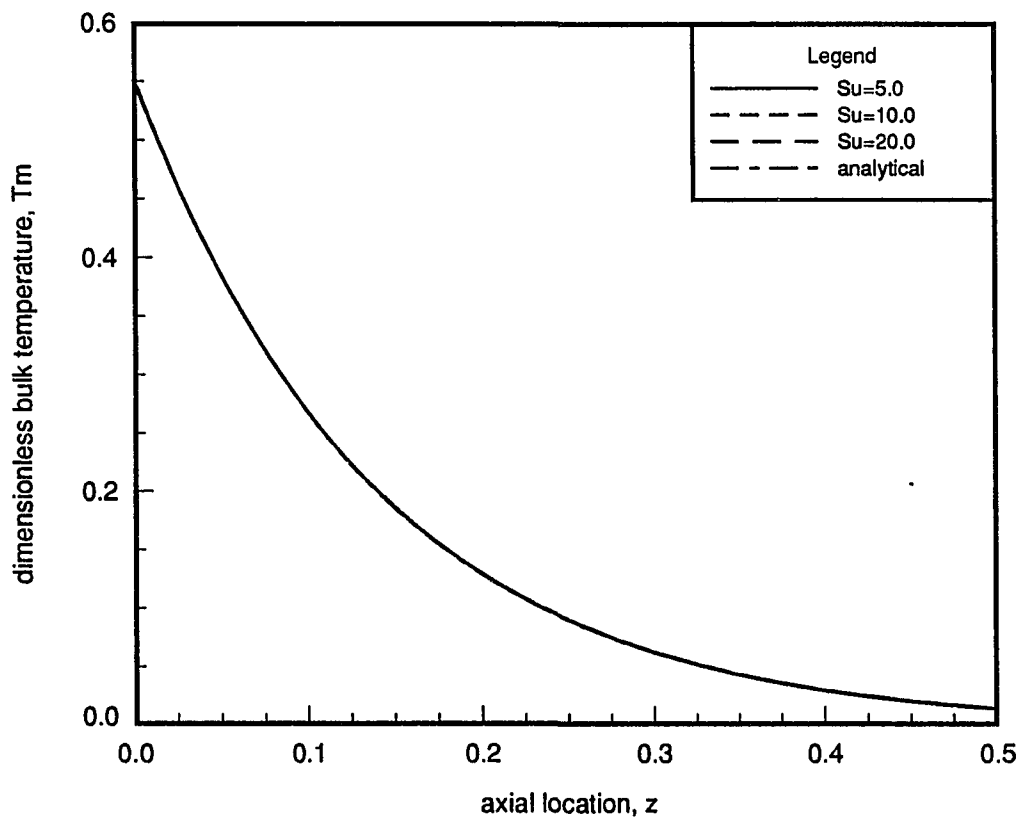


Figure 4.5: Dimensionless bulk mean temperature drop for the fully developed flow

T_m decreases by one-half can be calculated to be

$$\Delta z = \ln\left(\frac{1}{2}\right) / (-2 \times 3.6568) = 0.0948.$$

This distance agrees very well with that measured from Figure 4.2 ($\Delta z = .095$) in the previous section.

The Nusselt number in the uniform passage flow is given by the solution to the well known fully developed flow problem, in which Nusselt number is defined as

$$Nu_z = \frac{h_z (2a)}{k_l}$$

where a is the pipe radius. The radial length scales are different because the boundaries of the liquid phase are located at different radii. The local Nusselt number for the fully developed flow, in which the temperature profile is self-similar and independent of the z , is 3.6568 [13]. The local Nusselt numbers calculated from the steady-state ice layer profiles are shown in Figure 4.6. The numerically calculated Nusselt numbers at the inlet is 3.6519, which is 0.13% less than 3.6568 for the fully developed flow due to the truncation error. Figure 4.6 shows that the Nusselt number in converging passages increases initially. The reason for this is that the bulk temperature drops exponentially along the pipe axis (see Figure 4.5). But as z continues to increase, Nu reaches a peak, and then it starts to decrease. This decrease in Nu is due to the cooling of the liquid as it flows downstream. As z continues to increase, the radial temperature gradient at the wall eventually becomes small enough to offset the effect of decreasing T_m . In all cases, the maximum deviation of Nu from that of the fully developed flow is only 1.2%. The bulk mean temperature and Nusselt number both demonstrate that the flow is almost thermally fully developed at the final steady state.

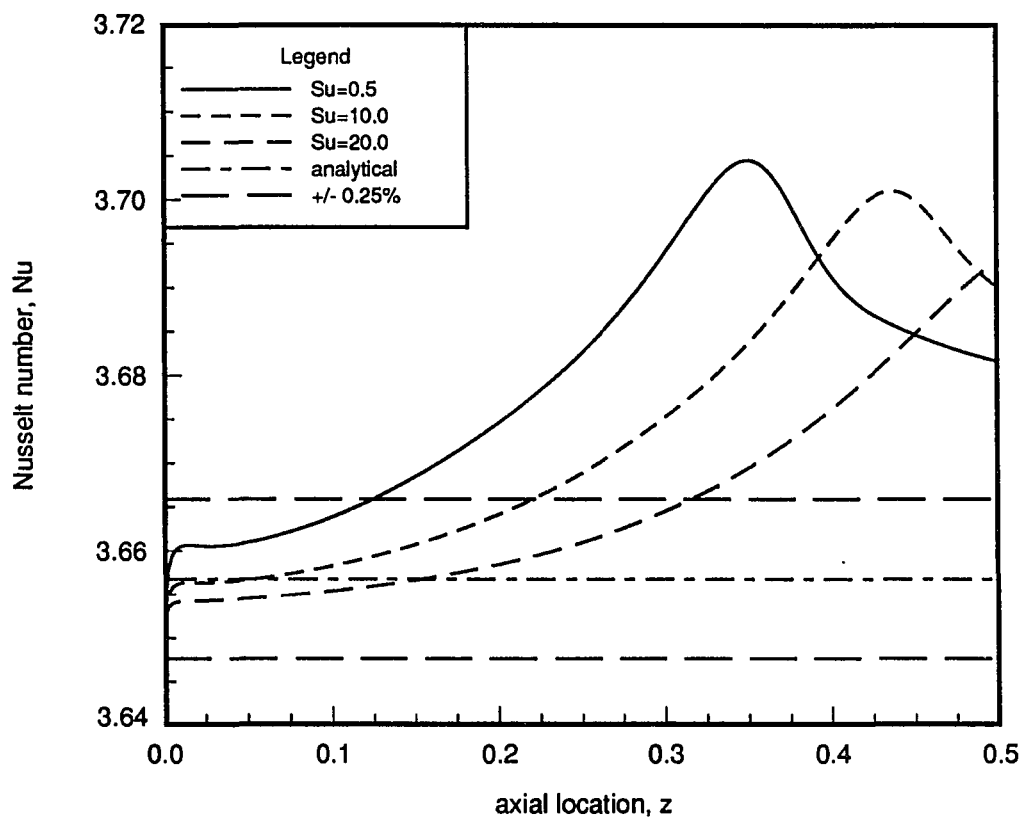


Figure 4.6: Comparison of Nusselt numbers for the fully developed flow

4.2 Results Using Developing Flow Initial Condition

When the wall temperature of the test section, which is initially filled with uniformly superheated liquid, is lowered to T_w , which is uniform along the pipe and below the freezing temperature, ice starts to grow inwardly from the pipe wall along the test section. Provided that the liquid is sufficiently superheated, the ice layer grows asymptotically to a steady state, in which the ice layer thickness is increasing axially throughout the test section. In particular, the ice thickness starts from zero at the pipe inlet ($z = 0$). This steady state is considered to be the initial condition. This initial condition is especially appropriate for the thermally developing flows which characterize short lengths of pipe.

4.2.1 Initial ice layer profile

This initial condition has been divided into two intervals. One is for small z , where the ice layer thickness is assumed to be so thin that it has negligible effect on the hydrodynamic field. Therefore, the hydrodynamic field is assumed fully developed and the thermal field, developing — the Graetz problem. This thin ice layer limit is valid in the limits $z \rightarrow 0$ and $Su \rightarrow \infty$. The other interval is for large z , where the ice layer has a significant effect on the hydrodynamic field. Therefore, all five (steady) governing equations must be solved simultaneously in this interval. The thin ice layer is assumed up to a certain axial location $z = z_{tr}$, and after that point, ice thickness is not regarded as thin any more. For a small z interval, the asymptotic solution is obtained by first solving the Graetz problem using the boundary layer scale for the liquid phase region (see Appendix A, Section A.3) and then by solving the solid energy equation and the interface equation using *a priori* liquid temperature

field. In particular, the asymptotic ice thickness is given by Equation (A.54) as a function of z .

In the results presented in this section, the axial coordinate is slightly modified by $Z = z - z_{tr}$, in which coordinate system $Z = 0$ is the beginning of the large z interval, where all five (steady) governing equations are solved simultaneously. The initial condition at $Z = 0$ is given by the small z solution at $z = z_{tr}$, where the liquid temperature needs to be interpolated from the boundary layer scale for small z solution into the core scale used in large z formulation. The initial ice layer profile depends most on Su and is independent of Ste , which only affects the rate of ice growth. The effect of λ is very minor because it also is essentially a rate parameter, as being the ratio of thermal diffusivities. Figure 4.7 shows the significant effect of Su on the initial ice layer profile. As Su decreases, the ice grows thicker at the given axial location. This is the same behavior as observed for the fully developed flow initial condition. However, the ice layer profiles look quite different from those of the fully developed flow case in that the slope of ice layer here is very steep near the inlet and gradually decreases along the test section, whereas that of the fully developed flow case is almost linear along the test section.

For this steady-state initial condition, the ice layer may grow very thick in a short distance from the inlet, as shown in Figure 4.7. A difficulty in getting this initial condition has been observed, especially for small Su 's, in which the initial condition cannot be obtained for the whole test section when ϵ is larger than about 0.55 for the given Su . Figure 4.8 shows the maximum distance where the steady-state ice layer profile could be obtained. The maximum ice thickness and corresponding axial locations are shown in Figure 4.8 and are also listed in Table 4.4. The step size for

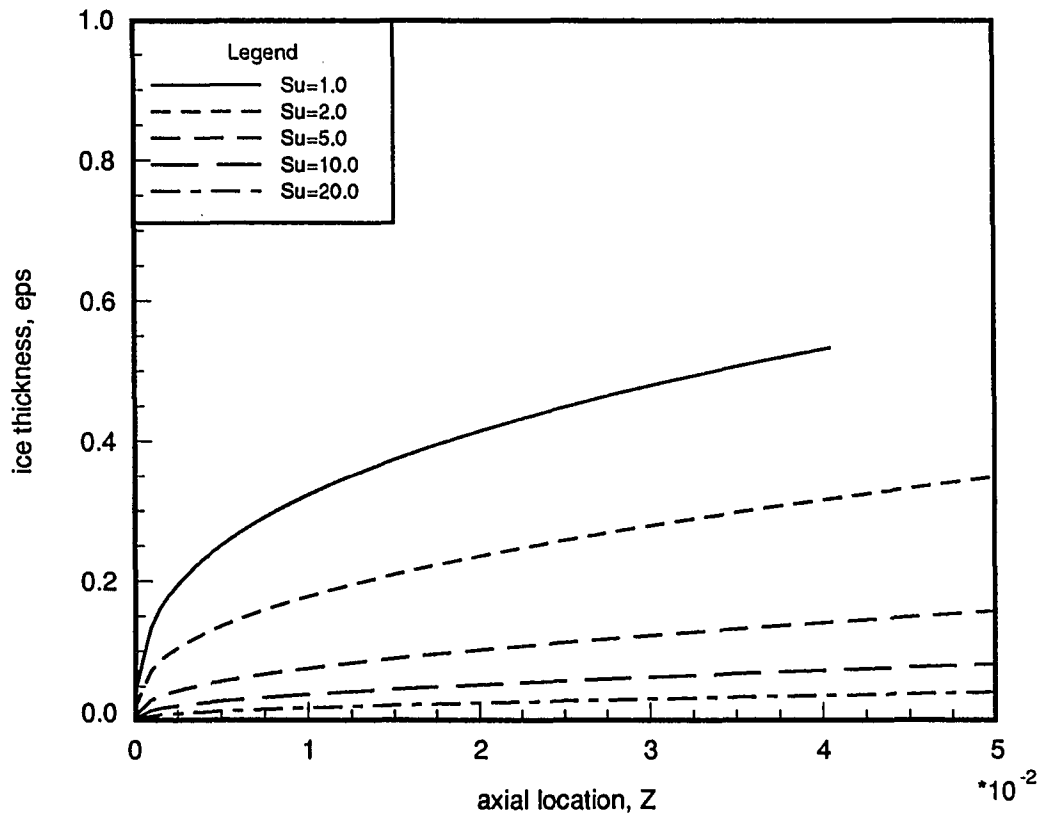


Figure 4.7: Initial ice layer profiles for the developing flow ($z_{max} = 0.05$)

Table 4.4: Maximum distance and ice thickness for the initial steady state

Su	Maximum distance, z	Maximum ice thickness, ϵ
0.2	0.0015	0.5456
0.4	0.0075	0.5667
0.5	0.0120	0.5659
0.6	0.0175	0.5649
0.8	0.0310	0.5631
1.0	0.0470	0.5631
2.0	0.1255	0.5624
5.0	0.2500	0.5625
10.0	0.3445	0.5618
20.0	0.4395	0.5624

the axial distance used in this result is $\Delta z = 5 \cdot 10^{-5}$. These maximum values can be increased somewhat by decreasing the step size, but qualitatively similar results are obtained. The reason for this behavior is not clear; however, an idea is suggested by the experimental results of Hirata and Ishihara [47]. In their experiments, the minimum value of diameter ratio ($B =$ ratio of minimum flow passage to pipe diameter) for an ice-band structure was about 0.5. When the diameter ratio decreased below this limit, the flow passage kept on decreasing until it finally froze shut. Also, according to their analysis, this minimum value of B increases slightly with the increasing temperature ratio θ , which is equivalent to decreasing Su , and increasing the modified Reynolds number which was defined based on the given pressure drop between the inlet and outlet.

Another interesting observation is made from the ice profiles shown in Figure 4.8. For small Su (≤ 1.0), the steady-state ice layer has been obtained only for a short distance from the inlet, and the profile is convex for the whole ice layer. The log-log plot of Figure 4.8 will help to demonstrate this behavior more easily, as shown in

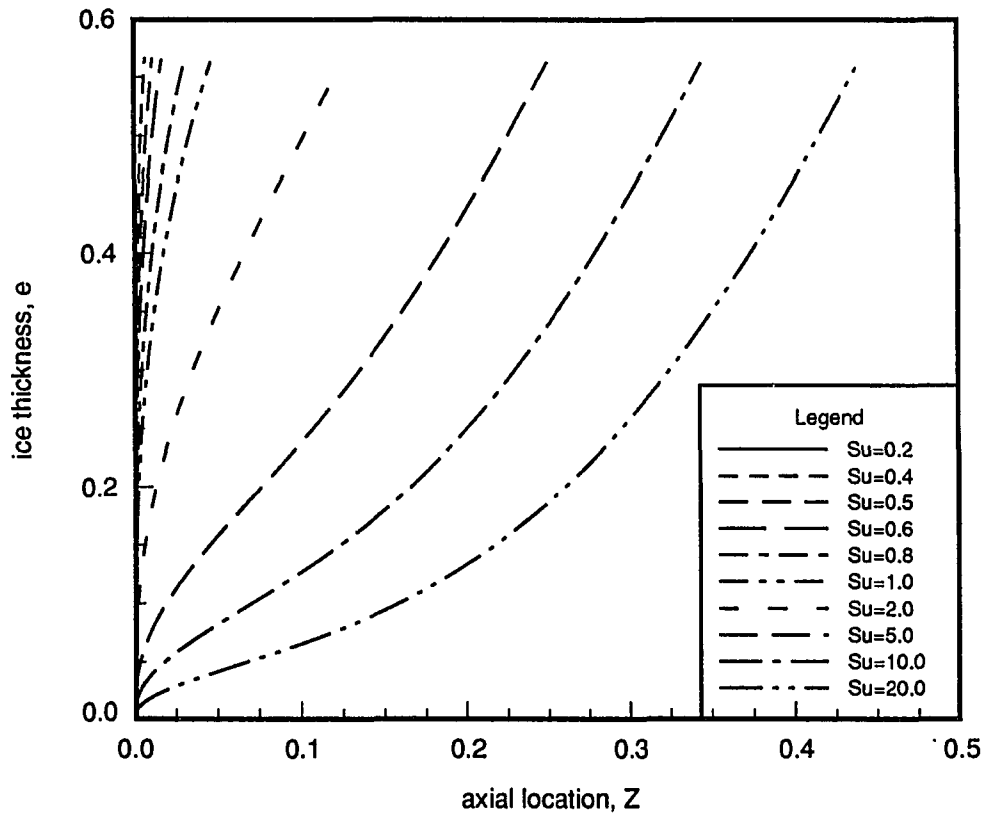


Figure 4.8: Maximum distances for the converged steady-state initial condition and the characteristic change of ice layer profiles

Figure 4.9. The asymptotic ice layer thickness (the line with a slope of $\frac{1}{3}$), which is determined as an asymptotic solution for small z , Equation (A.61), is drawn for comparison. (The asymptotic growth of ice layer and boundary layer thicknesses are shown in Figure A.4.) These lines are useful to determine how far the asymptotic solution is valid. For a thick ice layer ($Su = 0.4$), the numerically calculated ice layer profile deviates significantly from that of the asymptotic solution at $z = 10^{-4}$ whereas for thin ice layer ($Su \geq 5$), the comparison is very good at $z = 10^{-4}$. The reason is that for small Su , ϵ is large at $z = 10^{-4}$, and the validity of the asymptotic solution requires $\epsilon \ll 1$. It is shown from Figure 4.9 that as z increases, the slope of the ice layer for small Su (≤ 1.0) tends to decrease while that of large Su (≥ 2.0) increases. The ice layer profile at large z region for large Su is similar to those of fully developed flow initial condition cases. For a large Su (≥ 5.0), however, the profile is convex up to a certain distance from the inlet and then changes to concave beyond that location. This indicates that when the liquid has sufficient superheat, the ice layer can grow very far from the inlet and that the local amount of ice growth is large near the inlet, followed by gradual decrease and then an increase along the remainder of the ice layer. This may also suggest that the local amount of ice growth is larger when the ice layer is thicker. Similar behavior was observed in the results generated using the fully developed flow initial condition, which predicted a steeper slope for a thicker ice layer. The change of the ice layer profile from convex to concave in such a case is not as clear as in this case, however.

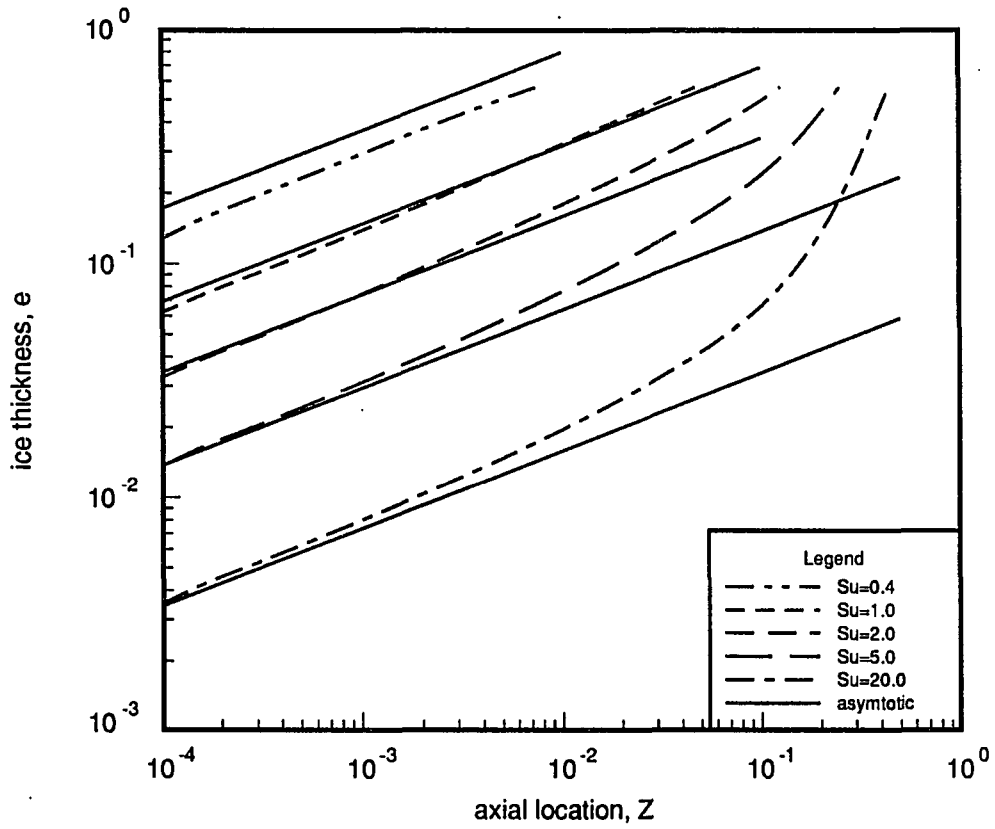


Figure 4.9: Log-log plot of the characteristic change of ice layer profiles

4.2.2 Heat transfer

The effect of ice layer growth on heat transfer for the developing flow is examined by comparing the Nusselt numbers calculated from the steady-state initial condition with those of Graetz solution. The definitions of the local Nusselt numbers are given in the discussion of the fully developed flow case. The local Nusselt number for the Graetz problem is unbounded as $z \rightarrow 0$ because the thickness of the thermal boundary layer approaches zero as the thermal entrance is approached. As the thickness of the thermal boundary layer increases in the flow direction, the local Nusselt number decreases until it reaches an asymptotic value, 3.6568, which is the Nusselt number for the fully developed flow with the isothermal boundary condition. The asymptotic local Nusselt number as $z \rightarrow 0$ has been calculated as

$$Nu_z^+ = 1.356598 z^{-\frac{1}{3}}$$

where the superscript $+$ denotes the asymptotic solution (see Appendix A, Equation (A.58)). The complete solution for the local Nusselt number of the Graetz problem has been numerically calculated using the boundary layer scale (see Appendix A, Section A.3.1 to A.3.3). The local Nusselt numbers for the Graetz problem and a few converging passage flows corresponding to different Su 's are compared in Figure 4.10. The slope of the Graetz solution is exactly $-\frac{1}{3}$ in a log-log plot.

The local Nusselt number increases when there is a reduction in the flow passage due to the ice growth, as shown in Figure 4.10. The maximum increase of Nu due to the internal freezing is 9.4% for $Su = 1.0$. The deviation decreases with increasing Su and Nu in converging flow passages approaches that of Graetz solution as the ice thickness decreases with increasing Su . This results from the increased convection

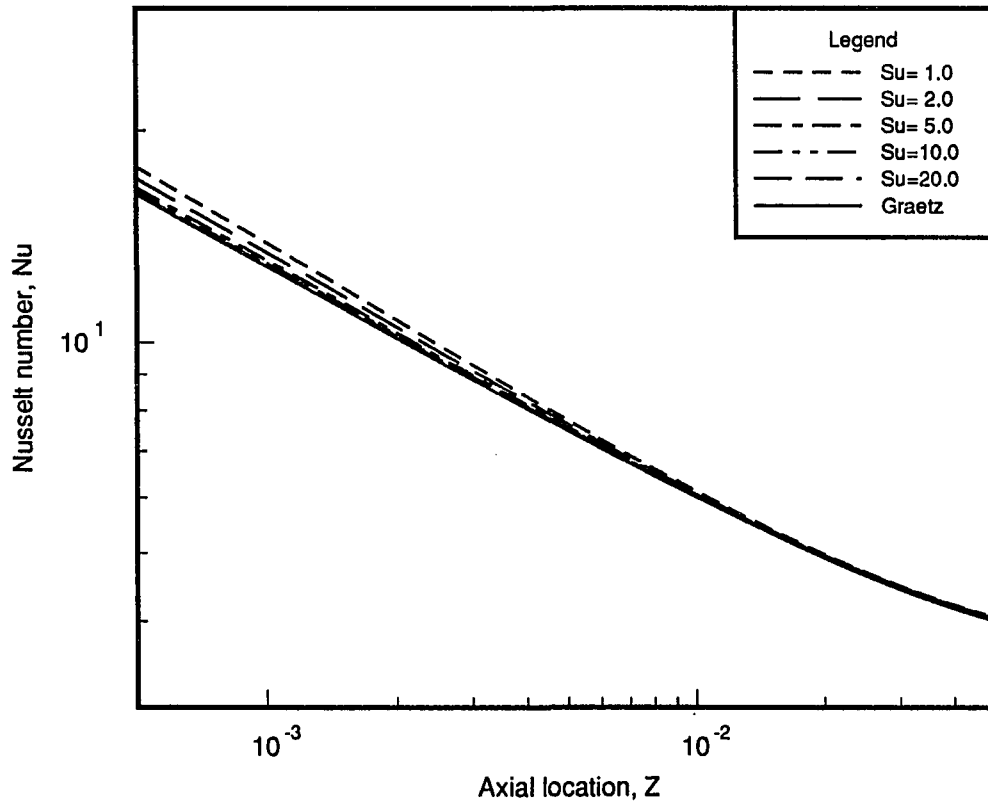


Figure 4.10: Comparison of Nusselt numbers for the developing flow

heat transfer coefficient due to the accelerated flow velocity, according to the constriction of the flow passage. The same result has been obtained for the fully developed initial condition case. The local Nusselt number in this study is calculated from the dimensionless bulk mean temperature and dimensionless temperature gradient, as described in the previous section. In relation to the effect of the ice growth on the heat transfer, the bulk mean temperatures can be compared between the present calculation and the solution to the Graetz problem, as shown in Figure 4.11. The comparison of dimensionless bulk mean temperatures between the present results and Graetz solution shows that T_m of flows with internal freezing is slightly higher than that of Graetz solution at small z (≤ 0.01), and it becomes lower as z increases. The reason for this is that, in general, temperature drop is less when the flow is accelerated due to the internal ice growth (when ice thickness is thin). When the ice layer is thick, however, temperature drop increases due to the narrow flow passage. This seems to offset the reduced temperature drop due to the flow acceleration. The temperature drop is about 40% along the test section ($0 \leq Z \leq 0.05$).

4.2.3 Disturbances and responses

According to Gilpin's experiments [42, 43], the ice first seemingly grew into a steady state with the ice layer profile gradually increasing in the axial direction. Later in time, an expansion of the flow passage at the test section exit was observed, and then it migrated upstream. He conjectured that it occurred because enhanced convective heat transfer due to the flow separation melted away the ice on the downstream of the separation point. This upstream migration is a most interesting phenomenon in freezing in pipe flows as well as the ice-band structure. This sudden expansion is

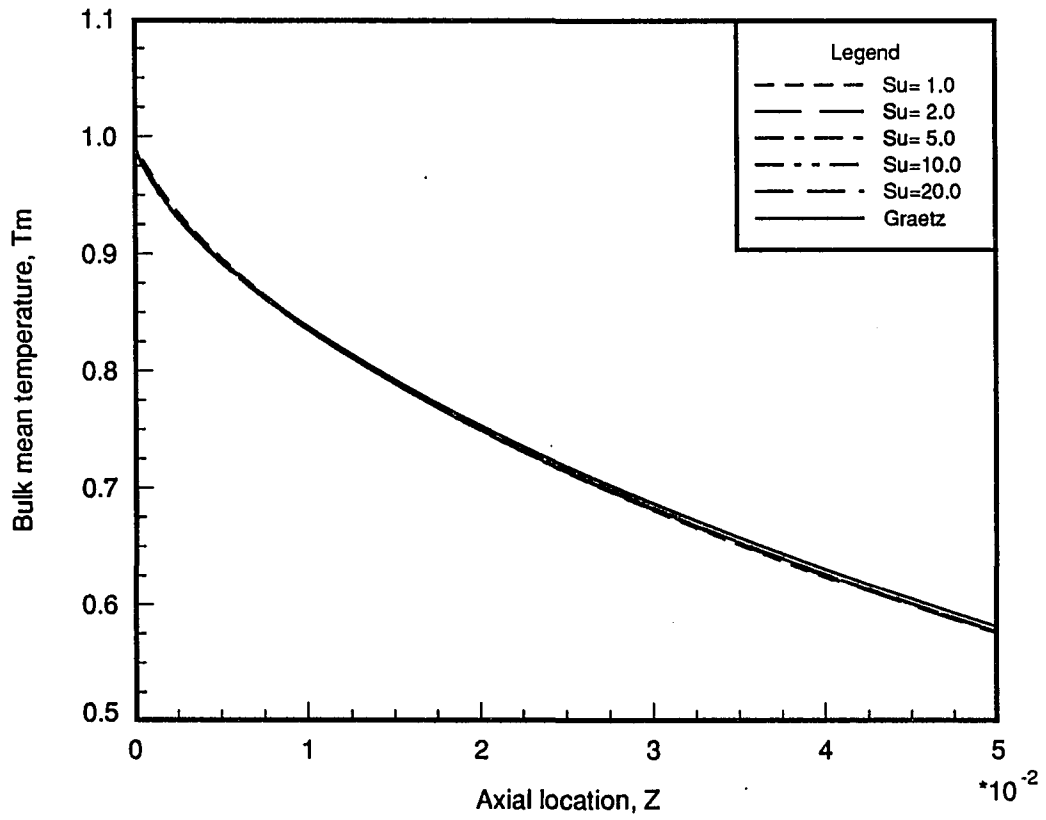
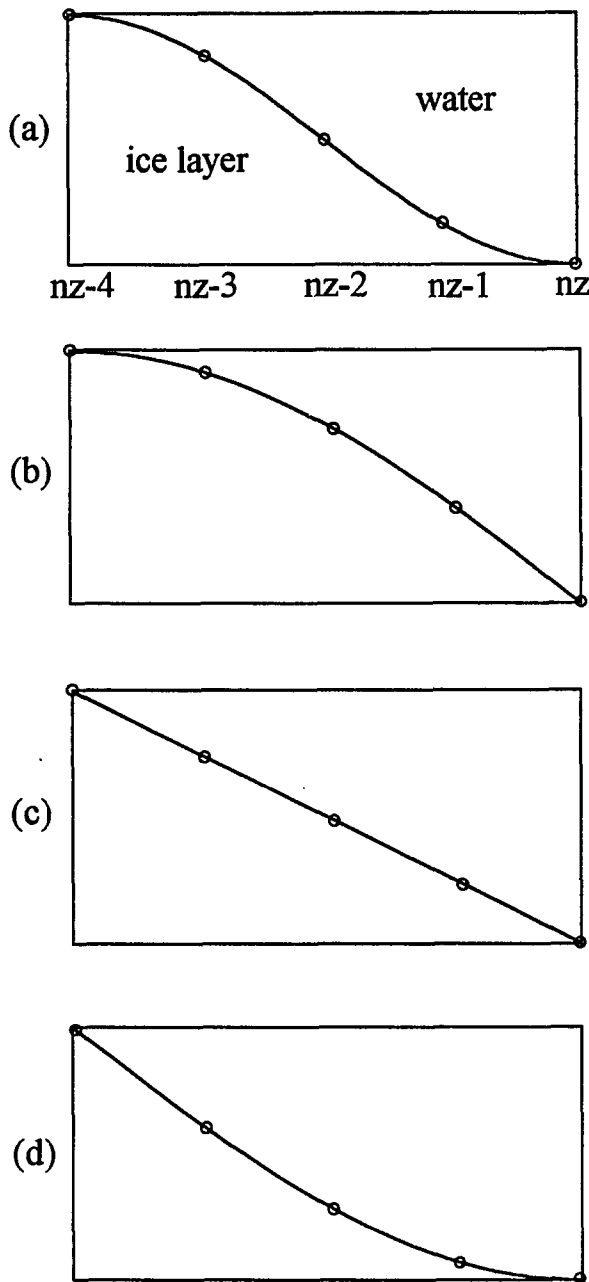


Figure 4.11: Comparison of bulk mean temperatures for the developing flow

simulated in the present study as a disturbance to the initial steady-state ice layer profile. Several forms of disturbances have been tried, as shown in Figure 4.12. When the shape of the expansion was smooth and the reduction in the ice thickness was small, the flow was attached to the solid-liquid interface without any separation, whereas a very tiny region of flow separation with reversed flow was observed to exist downstream of the expanded zone for a very sharp expansion. These disturbances were generated by specifying the ice thickness and its derivative during a ramping time of one or two time steps, during which the thermal and hydrodynamic fields were adjusted to the given shape of the solid-liquid interface by solving the remaining four governing equations (stream function, vorticity, liquid and solid temperatures) with the fixed radius of the solid-liquid interface. When the solid-liquid interface was calculated as part of the solution after the ramping time, in general, the disturbances disappeared, and the ice returned to its initial profile.

Figure 4.13 and Figure 4.14 show the contour plots of vorticity and stream function before, during, and after the ramping time and the final steady state (which is identical to the initial state) for the case of $Ste = 0.03$, $Su = 0.33$, $\lambda = 1.0$, $Pr = 10$. The ramping time was same as one time step, $\Delta t = 0.2$. At $t = 0 (n = 0)$, the ice layer thickness at the exit was 0.426854, and during the ramping, it was decreased to 90% of the initial thickness, 0.042685 (see Figure (b)). After five time steps ($n = 5$), the ice thickness increased to 0.205352 (see Figure (c)), and the transient calculation continued until it reached a final steady state at $n = 75$. This result (for a disturbance type D) represents the general responses of the present model to the four types of disturbances which were simulated in this study. This behavior is similar to the recent numerical results by Albert and Olfe [51], who considered the



All curves are sinusoidal.

Example of disturbance (a)

- During a ramping time, t_c

$$\varepsilon_{nz} = \varepsilon_{nz,IC} (1 - f R_\varepsilon)$$

$$\varepsilon'_{nz} = 0$$

where f varies from 0

to 1 during t_c and

R_ε is the maximum

amount of reduction.

- Other nodes

$$\varepsilon_{nz-4} = \varepsilon_{nz-4,IC}$$

$$\varepsilon'_{nz-4} = 0$$

$$\varepsilon_{nz-3} = \varepsilon_{nz} + \frac{1}{2} \left(1 + \frac{1}{\sqrt{2}}\right) \Delta\varepsilon$$

$$\varepsilon'_{nz-3} = \frac{\pi}{8\sqrt{2}\Delta z} (-\Delta\varepsilon)$$

$$\varepsilon_{nz-2} = \frac{1}{2} (\varepsilon_{nz} + \varepsilon_{nz-4})$$

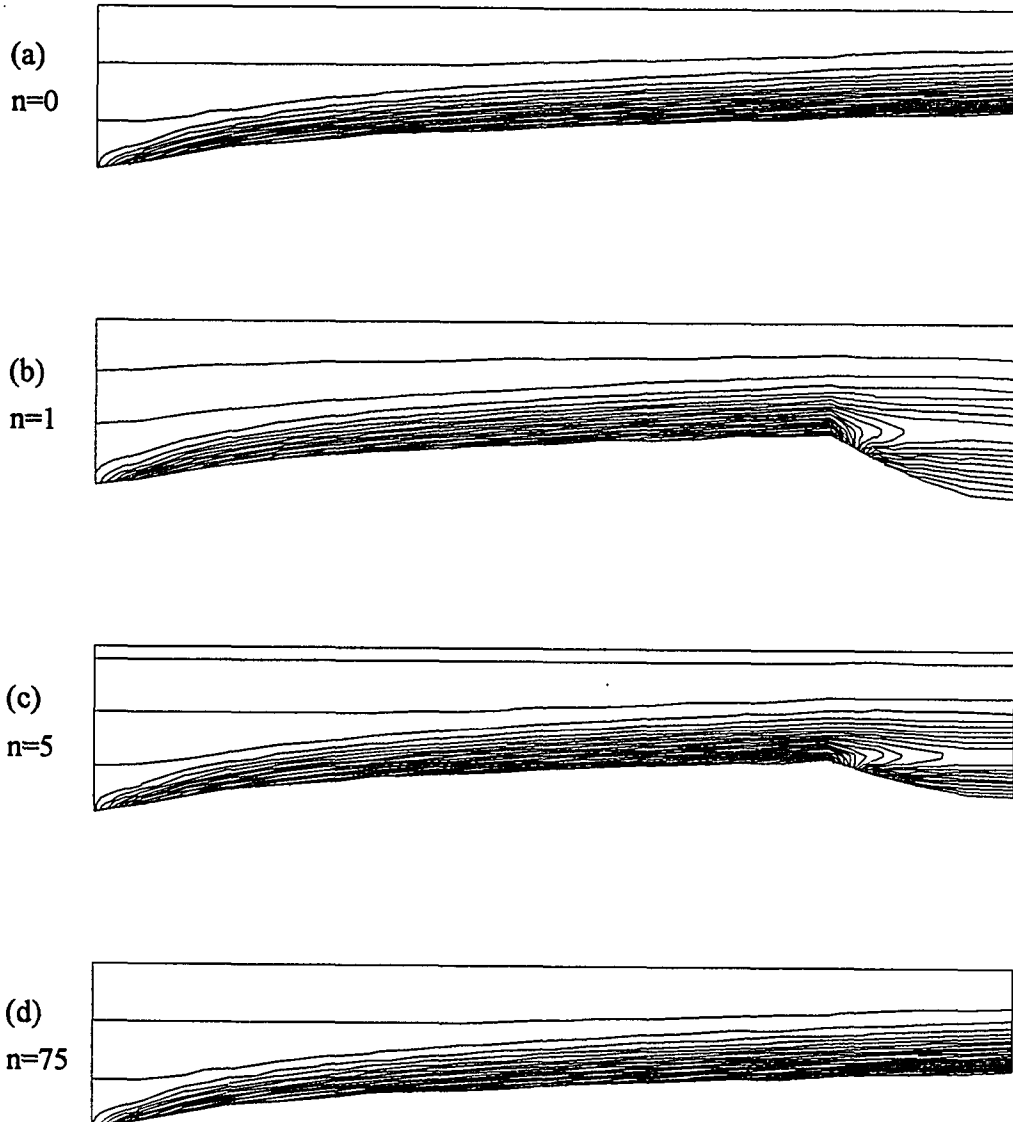
$$\varepsilon'_{nz-2} = \frac{\pi}{8\Delta z} (-\Delta\varepsilon)$$

$$\varepsilon_{nz-1} = \varepsilon_{nz} + \frac{1}{2} \left(1 - \frac{1}{\sqrt{2}}\right) \Delta\varepsilon$$

$$\varepsilon'_{nz-1} = \frac{\pi}{8\sqrt{2}\Delta z} (-\Delta\varepsilon)$$

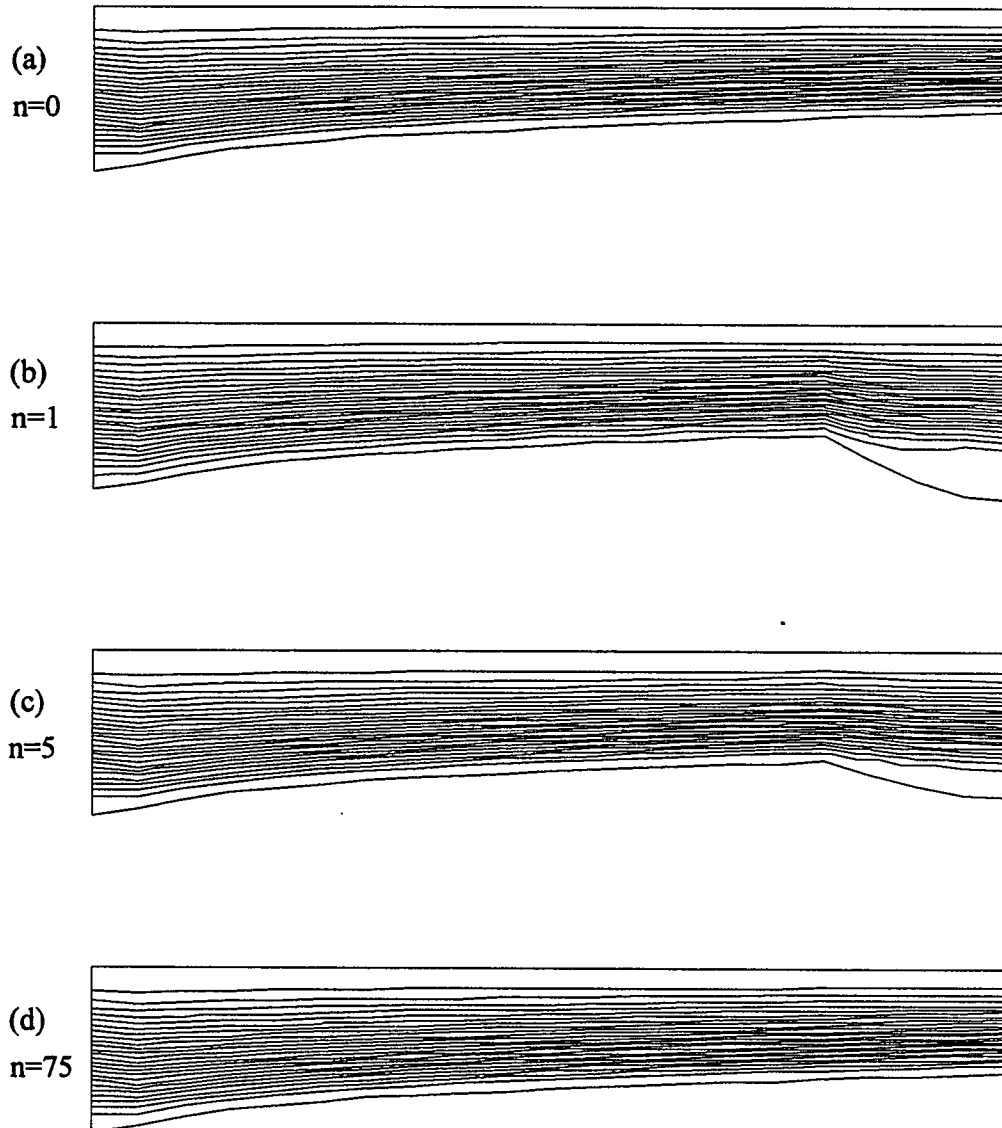
where $\Delta\varepsilon = \varepsilon_{nz-4} - \varepsilon_{nz}$

Figure 4.12: Forms of disturbances and an example of implementation



$Ste = 0.03, Su = 0.33, \lambda = 1.0, Pr = 10, \Delta t = 0.2$

Figure 4.13: Disturbances and responses: vorticity



$$Ste = 0.03, Su = 0.33, \lambda = 1.0, Pr = 10, \Delta t = 0.2$$

Figure 4.14: Disturbances and responses: stream function

freezing in forced laminar flow between parallel plates. Their purpose was also to predict the ice formation in forced flow with the possibility of recirculation.

The ice-band structure was not observed in any of these transient computations. Since only one point in the (Ste, Su) plane was sampled, it is quite possible that the transient solutions which were generated all lie in a stable zone of this parameter space. Another possibility is that some or all of Pe terms in the governing equations should be retained. This is suggested by some of literature [28, 38, 42] which indicate that a flow rate parameter may be important in interfacial stability considerations.

4.3 Effects of Internal Freezing on the Hydrodynamic Field

4.3.1 Pressure drop

The pressure drop along the test section is calculated for the steady-state ice profile. Figure 4.15 shows the relation between the pressure drop, ΔP , and the average radius of the solid-liquid interface, R^* , for $z_{max} = 0.05$. They are nearly linear on a log-log plot. As the average radius decreases, the pressure drop increases. The correlation can be obtained as a functional form of

$$\Delta P = CR^{*n} \quad (4.3)$$

where C and n depend on the length of the pipe. The exponent n is found to be -4.45 for the case shown in Figure 4.15. This result can be compared with the pressure drop without the internal freezing, which can be obtained from Hagen-Poiseuille equation of laminar flow through a pipe [60]:

$$Q = \frac{\pi}{2} a^2 w_{max} = \frac{\pi a^4}{8\mu l} (P_1 - P_2) \quad (4.4)$$

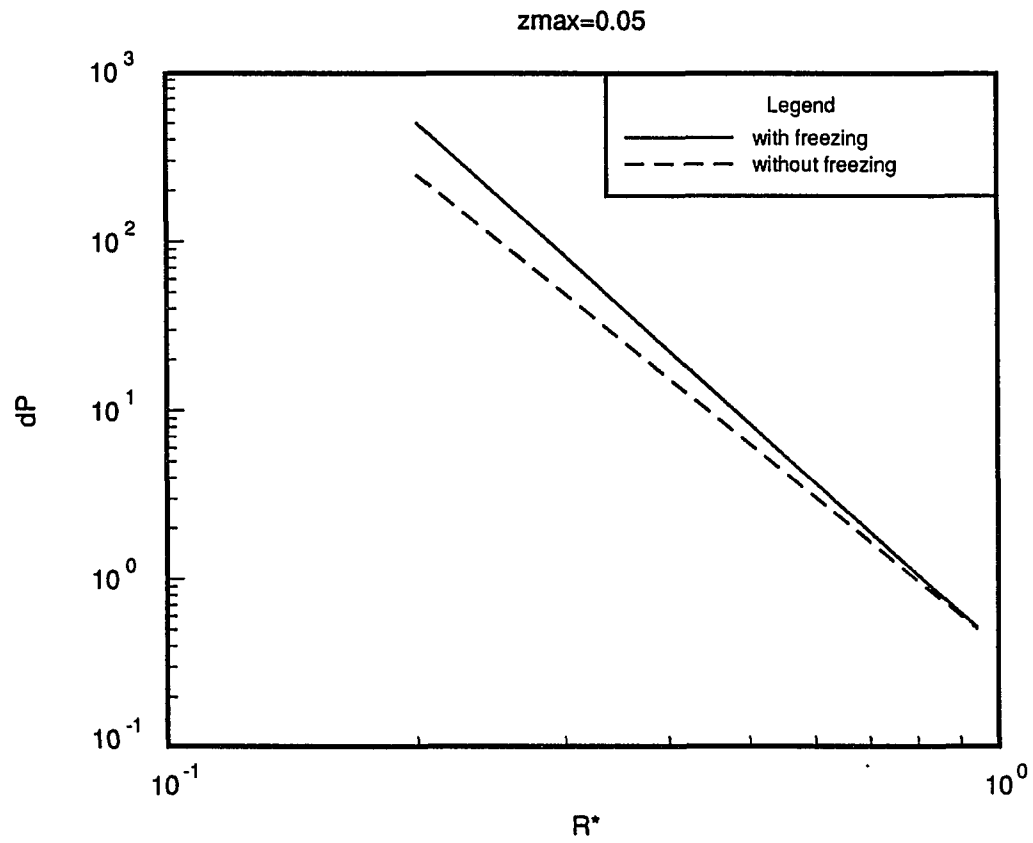


Figure 4.15: Relation between pressure drop and average flow passage radius for short pipe lengths

where Q is the volume flow rate and w_m is the maximum velocity. a and l are the radius and length of the pipe, respectively. These variables are in dimensional quantities. Equation (4.4) states that the volume rate of flow is proportional to the first power of the pressure drop per unit length, $\frac{P_1 - P_2}{l}$, and to the fourth power of the radius of the pipe. For the constant flow rate, which is the case for the present study, the exponent in Equation (4.3) will be -4 . Comparison of two exponents (-4.45 versus -4) indicates that, for the same average radius of the flow passage, a greater pressure drop is predicted when the flow passage converges with an axially increasing ice thickness inside the pipe wall. Figure 4.15 also shows that the pressure drop is larger when there is more reduction in flow passage radius.

In general, more pressure drop is seen for narrower flow passages. This presents another aspect of pipe freeze-off conditions, which will be discussed in the next section. For the flow induced by the given pressure drop between the inlet and the outlet, because of this pressure drop in narrowing flow passages, the flow rate cannot be maintained in a real pipe flow but instead decreases until freeze-off, when the given pressure drop is not enough to overcome the resistance due to the ice growth along the pipe length.

The dimensionless pressure drop and normalized pressure corresponding to Figures 4.2 and 4.3 are shown in Figures 4.16 and 4.17, respectively. Initially fully developed flow condition is used for these cases. For a pipe of $z_{max} = 0.05$ (see Figure 4.16), pressure drop is almost linear in z except for small Su (1 and 2) at large z (> 0.01). The normalized pressure drop for this linear pressure drop is unity, as shown by a horizontal line. As z increases, pressure drop deviates from the line (especially for $Su = 1$ at large z), which make the normalized pressure deviate from

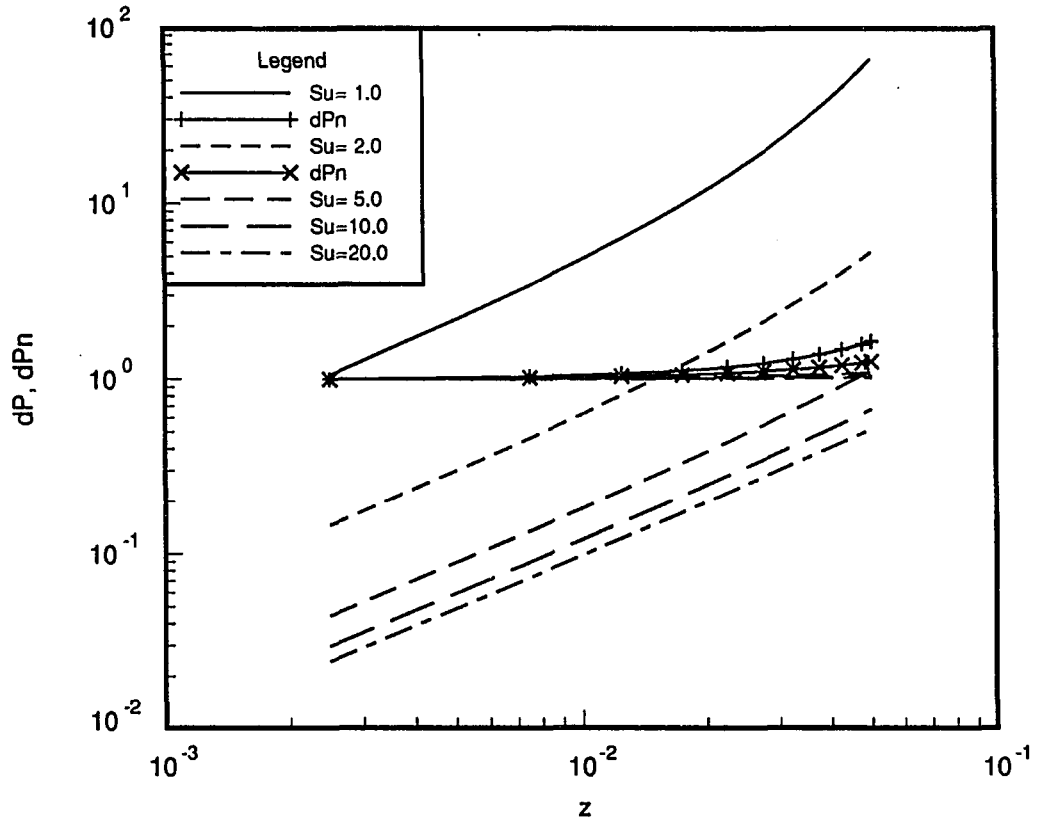


Figure 4.16: Pressure drop through the pipe for the final steady-state ice layer profile ($z_{max} = 0.05$)

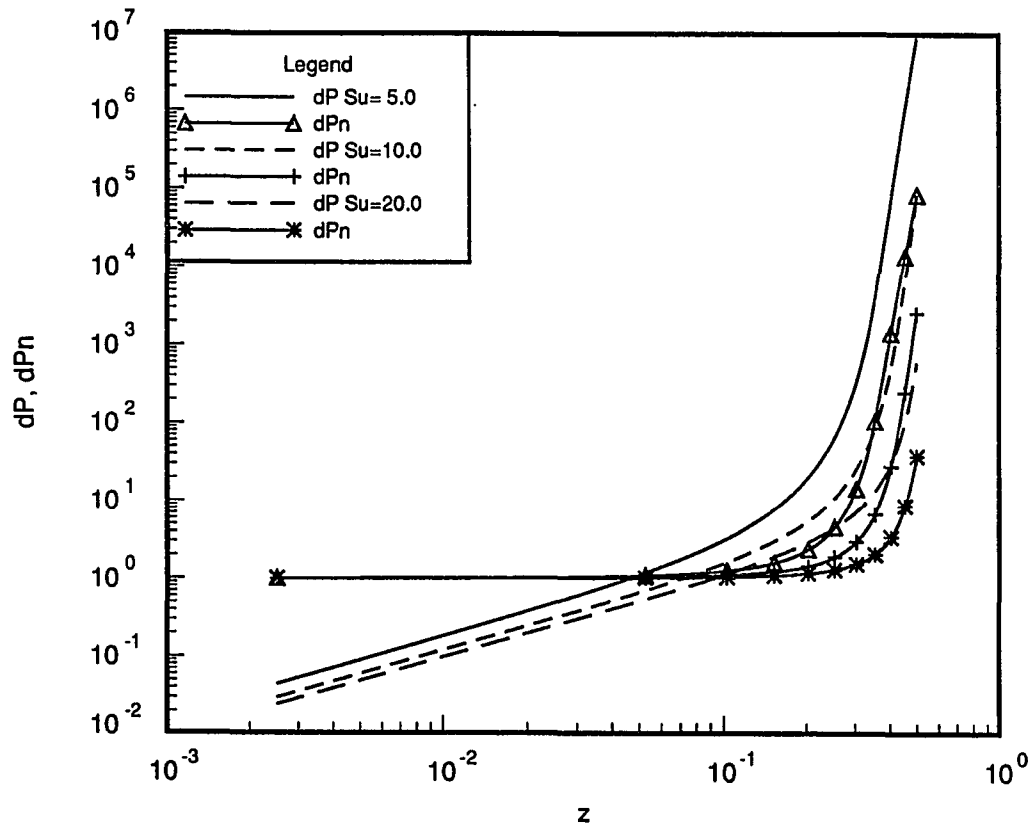


Figure 4.17: Pressure drop through the pipe for the final steady-state ice layer profile ($z_{max} = 0.5$)

the horizontal line. For a longer pipe (see Figure 4.17), pressure drop at $z \leq 0.1$ is almost linear (as shown in Figure 4.16), and it increases significantly at $z \geq 0.2$. The normalized pressure also follows the same trend. Up to $z = 0.1$, it remains almost constant as 1, and thereafter it starts to deviate from unity. ΔP_n for smaller Su starts to deviate from the horizontal line at a shorter distance, which is due to thick ice layer thickness (narrower flow passages).

The normalized pressure drop is plotted versus some measures of departure defined in Section 4.1.2. Figure 4.18 shows how the normalized pressure varies according to ΔR^* , ΔR , and ϕ_R , respectively. They show similar trends to one another. The only difference is that the relative magnitudes of each measure are different. For a given ice layer profile, ΔR^* is the smallest value due to its definition, like a standard deviation. ϕ_R is the greatest because it is obtained by dividing ΔR by R^* (≤ 1). Note that the results for $Su = 5, 10, \text{ and } 20$ appear to show convergence to a limiting profile for the $Su \rightarrow \infty$ limit. This is due to the fully developed flow (similarity solution) observed earlier from ϵ , Nu , and T_m results. The deviation of the normalized pressure from unity indicates the pressure drop is not linear any more. ΔP_n of several orders of magnitude larger than unity suggests that the constant flow rate condition may not be appropriate in such cases. It is because in order to maintain the given flow rate, the pump capacity must be very large to overcome the great pressure drop across the pipe, but the capacity of a pump is generally limited. Using the predicted pressure drop in a pipe with internal freezing, the necessary pressure drop to maintain the flow may be obtained as an application of this study.

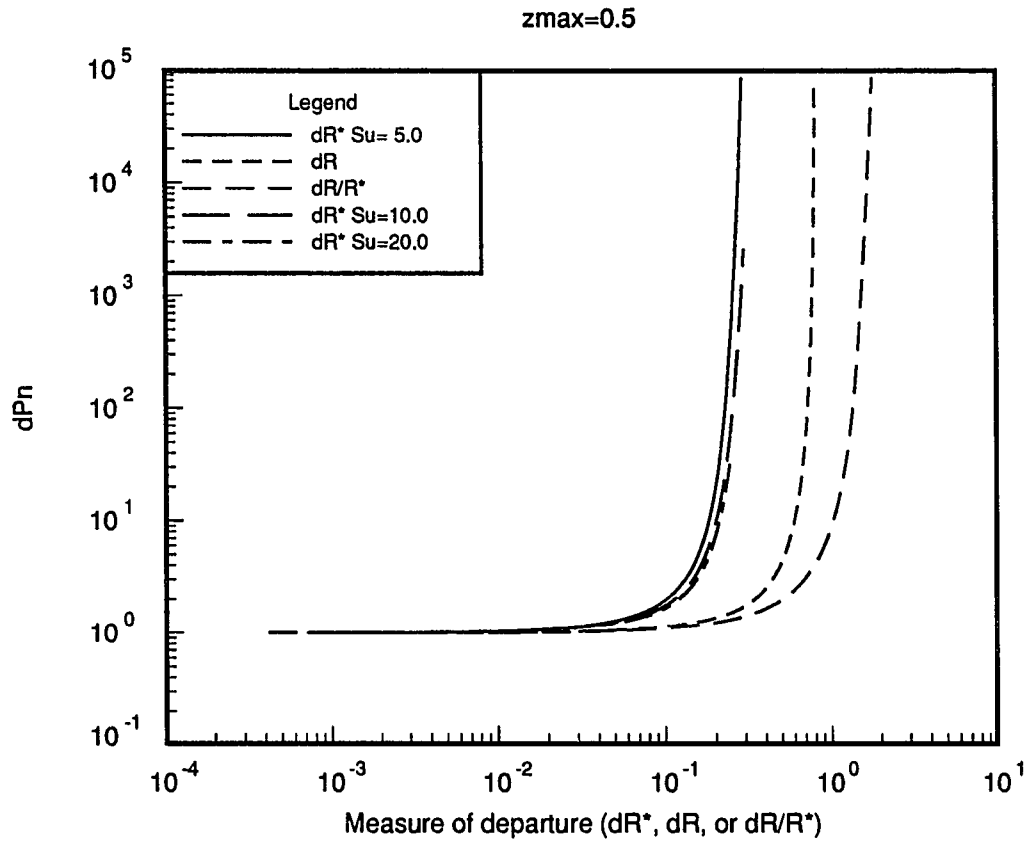


Figure 4.18: Normalized pressure drop versus various measures of departure of the flow passage radius

4.3.2 Velocity profile

As the flow passage narrows with axial ice growth, the fluid flow is accelerated, and the axial velocity component changes its profile along the axial direction. To determine the effects of ice growth on the velocity field, the axial velocity is calculated from the definition of the stream function:

$$\bar{w} = \frac{1}{\bar{r}} \frac{\partial \bar{f}}{\partial \bar{r}}$$

and the boundary conditions

$$\frac{\partial \bar{w}}{\partial \bar{r}} = 0 \quad \text{at } \bar{r} = 0 \quad \text{and} \quad \bar{w} = 0 \quad \text{at } \bar{r} = \bar{R}.$$

Upon nondimensionalization, they become

$$w = \frac{1}{R^2} \frac{1}{r_c} \frac{\partial f}{\partial r_c} \quad (4.5)$$

and

$$\frac{\partial w}{\partial r_c} = 0 \quad \text{at } r_c = 0 \quad \text{and} \quad w = 0 \quad \text{at } r_c = 1. \quad (4.6)$$

Equation (4.5) is numerically solved for interior nodes ($1 \leq i \leq nr - 1$), whereas no-slip and symmetry boundary conditions are used at the solid-liquid interface and the centerline, respectively.

Figure 4.19 (a) shows the accelerated velocity profiles (compared with that of fully developed flow in a pipe without ice growth, which has a maximum velocity of magnitude 1 at the center) at different axial locations. The velocity profile in the pipe generally becomes flatter as the velocity increases. The shape of the velocity profile can be compared more directly when they are normalized by its maximum velocity at the center, shown in Figure 4.19 (b). Even though the axial velocity increases

Table 4.5: Centerline velocity increases and maximum deviations from the parabolic velocity

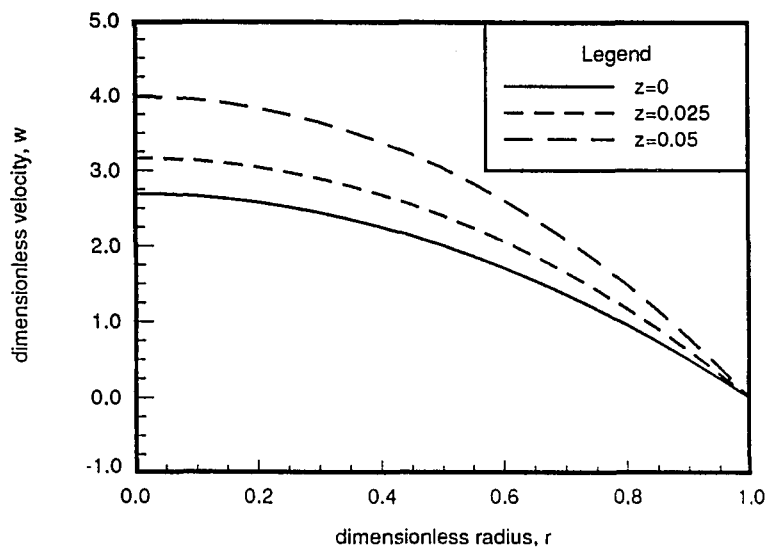
Su	Ice layer thickness			Centerline velocity increase ^a			Deviation ^b	
	$z = 0.0$	0.025	0.05	$z = 0.0$	0.025	0.05	0.025	0.05
1.0	0.6272	0.6857	0.7493	619.50	872.60	1418.15	3.06	3.60
2.0	0.3904	0.4442	0.5055	169.22	216.79	298.66	1.64	1.96
5.0	0.1798	0.2106	0.2470	48.66	59.08	74.49	0.68	0.81
10.0	0.0943	0.1118	0.1325	21.94	26.20	32.17	0.34	0.41
20.0	0.0483	0.0576	0.0687	10.44	12.36	14.99	0.17	0.21

^a $\frac{w_R - w_a}{w_a} \times 100$, percent increase from the fully developed velocity in a pipe of radius a .

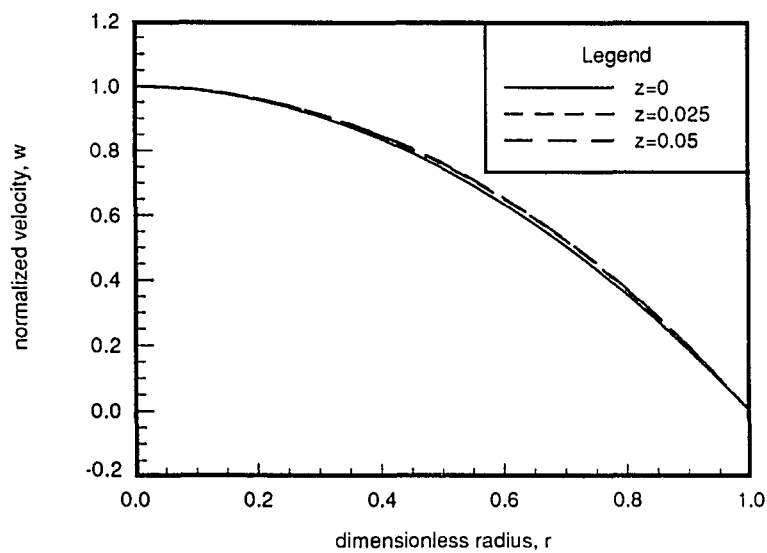
^b $\frac{w_n - w_p}{w_p} \times 100$, maximum deviation from the parabolic velocity profile, %.

significantly with the reduced flow passage, its profile remains relatively similar and close to the parabolic distribution. This validates the commonly used assumption in analytical analyses and numerical models.

The velocity profiles shown in Figure 4.19 are for $Su = 2.0$ case. The other cases show qualitatively similar behavior. The amounts of the axial velocity increase at the centerline due to the reduced flow passage radius from the fully developed flow in the uniform pipe flow without the ice developed and the maximum deviations of the velocity profile from the parabolic distribution are listed in Table 4.5. Ice layer thickness at the inlet, middle, and exit of the test section are included in the table. The numbers in the table except those for ice layer thickness are percent changes or deviations. The maximum deviation of the axial velocity profile from the parabolic distribution occurs near $r = 0.7$.



(a) Accelerated velocity profiles



(b) Normalized velocity profiles

Figure 4.19: Velocity profiles at different axial locations ($Su = 2.0$)

5. CONCLUSIONS

The freezing of a liquid flowing in a pipe has been studied using a numerical model with two types of initial conditions: the fully developed flow and the developing flow. Analytical and asymptotic solutions have been obtained for the fully developed flow initial condition and the developing flow initial condition, respectively. The fully developed flow condition is obtained far downstream from the thermal entrance, where the fluid flow approaches thermally fully developed flow. As a result, the fully developed initial condition is more appropriate for a long pipe, where thermal entrance region is not as important. For a short pipe, where the thermal entrance region is important, the developing initial condition is more appropriate.

For the fully developed flow initial condition, the ice layer is of uniform thickness with fully developed hydrodynamic and thermal fields. The temperature profiles are self-similar and vary exponentially in the axial direction. Transient calculation starts by changing the exponentially increasing wall temperature to the uniform temperature equal to that of inlet pipe wall. This change of boundary condition occurs during a ramping time t_c of a few time steps. The effect of the ramping time has been found to be minor except for the extremely fast freezing cases in which the freezing time required to reach the asymptotic ice layer thickness is affected significantly by the ramping time. A number of combinations of λ , Ste , and Su representing

different freezing conditions have been simulated to predict the ice growth in the pipe. The range of the axial coordinate used in this simulation is $0 \leq z \leq 0.05$ and 0.5 , representing a long pipe. When the liquid has enough superheat at the inlet of the test section, the transient calculation continues until asymptotic steady state is approached (no more ice growth is observed) and then the calculation is terminated.

The freezing time required to reach a final steady state depends on λ , Ste , and Su but most significantly on Ste . Because this final steady state is only approached asymptotically, the time required to reach 95% of the total ice growth is used as the freezing time. The relation between the freezing time (t_{95}) and Ste is almost linear on a log-log plot. The slope has been found to be approximately -1 , which means that t_{95} is inversely proportional to Ste for given λ and Su . A similar trend has been observed between t_{95} and Su . The relation becomes linear on a log-log plot as Su increases and Ste decreases, but the slope is -1.80 in this case. In this result, t_{95} increases as Su decreases, which means that it takes a longer time to reach the final steady state when Su is smaller. This result contrasts with the conduction result in which it takes less time to freeze a liquid with smaller Su . In that case, a non-flowing liquid in a pipe with the isothermal wall below the freezing temperature is completely frozen up to the center.

It is shown that the ice layer profile at the final steady state increases almost linearly along the test section (for small z). This steady-state ice layer thickness is independent of λ and Ste because these parameters affect the freezing rate or freezing time but do not change the steady-state ice layer profile. The ice layer thickness at the final steady state is greater, on average, for smaller Su . Also the amount of ice growth from the initial state to the final state is greater for smaller Su . This suggests

that local rate of ice growth is larger when the ice is thicker, which may indicate that the ice grows more rapidly downstream. It is shown by the larger slope of the solid-liquid interface for the thicker ice layer from the result using $z_{max} = 0.05$, and is confirmed by the simulation in a longer test section ($z_{max} = 0.5$) which revealed that the ice layer profile is convex for small z (thin ice layer) and concave for somewhat larger z (thick ice layer). The same results were obtained with the developing flow initial condition.

The long test section results revealed another interesting behavior of the fully developed flow. The ice layer profiles predicted by the present model showed self-similarity, which indicates that the initially fully developed flow condition was maintained even with the ice layer growth. The self-similarity is better for the larger Su cases, which has a thinner ice layer. As a result, only one ice layer profile can serve to represent the various Su 's. The effect of the ice layer growth on heat transfer was examined by comparing Nusselt numbers between the uniform passage flow and converging passage flow due to the axial ice growth. Nusselt number in converging passages increased initially until it reached a peak, and then it decreased. In all cases, however, Nu never differed by more than 1.2% from the fully developed value. The bulk temperature was found to drop exponentially along the pipe axis and showed negligible dependence upon Su — further demonstrating that the flow was almost thermally fully developed.

One of the most significant effects of the ice growth in a pipe flow is the pressure drop due to the constriction of the flow passage. The pressure drop due to the constriction of the flow passage, ΔP , has been correlated with the average radius of the flow passage, R^* . The correlation was obtained, for small z_{max} , as a functional

form of

$$\Delta P = CR^{*n}$$

where C and n are constants depending on test parameters such as pipe length and flow rate. The exponent n was found to be -4.45 for the test parameters used in this simulation, compared to -4 for a Hagen-Poiseuille flow.

The axial velocity profiles in the converging flow passage due to the ice growth in the pipe have been examined at different axial locations for several different steady-state ice layer profiles. Even though the axial velocity has increased significantly with the reduced flow passage, its profile remains very similar to the parabolic distribution. The maximum deviation from the parabolic distribution is only 3.6% for the velocity profile accelerated to a speed of 14 times more than the pipe flow without ice growth. This deviation consists of a slight flattening of the profile in the core region. This validates the assumption of a parabolic velocity distribution, commonly used in analytical analyses and simplified numerical models.

For the developing flow initial condition, the ice layer thickness rapidly increases from zero at the inlet like $z^{1/3}$ as $z \rightarrow 0$. As mentioned earlier, when the Su is very large, the convex profile of the ice layer changes to a concave profile. The present model with this initial condition predicts the ice growth only up to 50 to 70% of the pipe radius, depending on the axial step size. After that point, no converged solutions were obtained. The reason for this behavior is not clear yet. The maximum values of ice thickness obtained from this initial condition are less than those based upon the fully developed initial condition, which showed no convergence problem even with ice growth up to more than 90% of the pipe radius.

The effects of axially increasing ice layer thickness on the heat transfer have

been examined by comparing Nusselt numbers calculated using the present model with the developing flow initial condition with those for the uniform passage flow, which is well-known as the solution to the Graetz problem. The comparison has shown that Nusselt number in the converging passage flow is higher than that of the Graetz solution and that the increase in Nusselt number is greater for a narrower flow passage. This seems to be the result of the increased convection heat transfer coefficient due to accelerated flow velocity according to the constriction of the flow passage. A comparison for the bulk mean temperatures has shown that the bulk mean temperature for the freezing pipe is also higher than that of the Graetz solution. Thus the temperature drop is less when the flow is accelerated due to the constricted flow passage. As a result, the larger radial temperature gradient in the liquid PCM contributes to enhance heat transfer in a pipe flow with internal freezing.

One of the foremost interests in this study was the possibility of predicting the ice-band structure, as observed in experiments by Gilpin and others. The expansion of the flow passage at the exit, which in experiments was observed to appear first at the exit and then migrate upstream to the point where a new steady-state ice layer profile (in ice bands) was reached, was simulated by changing the ice thickness near the exit from the initial steady state. Various forms of finite disturbances were tried. When the shape of the expansion was smooth and the reduction in the ice thickness was small, the flow remained attached to the solid-liquid interface without any separation, whereas a very tiny region of flow separation with reversed flow was observed to exist in the downstream of the expanded zone for a very sharp expansion. When the deformed solid-liquid interface was subsequently allowed to change freely so as to comply with all governing equations, the disturbance disappeared as the ice

layer returned to its initial profile.

The ice-band structure was not observed in the present results. The cases simulated in this study may belong to the flow regime where the simply increasing ice layer profile is the proper steady state rather than the ice-band structure. Another possibility is that some or all of Pe terms in the governing equations, which were assumed very small and dropped from the present numerical model, should be retained. Nevertheless, the results obtained from the numerical model help to provide a general understanding of the freezing problem in pipe flows.

REFERENCES

- [1] Fukusako, S. and Seki, N. "Fundamental aspects of analytical and numerical methods on freezing and melting heat-transfer problems." *Annual Review of Numerical Fluid Mechanics and Heat Transfer* 1 (1986): 351-402.
- [2] Yao, L. S. and Prusa, J. "Melting and Freezing." *Advances in Heat Transfer* 19 (1989): 1-95.
- [3] Bankoff, S. G. "Heat conduction or diffusion with change of phase." *Advances in Chemical Engineering* 5 (1964): 75-150.
- [4] Muehlbauer J. C. and Sunderland J. E. "Heat conduction with a freezing or melting." *Applied Mechanics Review* 18 (1965): 951-959.
- [5] Crank, J. *Free and Moving Boundary Problems*. London and New York: Oxford University Press (Clarendon), 1984.
- [6] Cheung, F. B. and Epstein, M. "Solidification and melting in fluid flow." *Advances in Transport Processes* 3 (1984): 35-117.
- [7] Rubinstein, L. I. *The Stefan problem*, Translations of Mathematical Monographs (Vol. 27). Providence, R.I.: American Mathematical Society, 1971.
- [8] Beaubouef, R. T. and Chapman, A. J. "Freezing of fluids in forced flow." *Int. J. Heat Mass Transfer* 10 (1967): 1581-1587.
- [9] Pekeris, C. L. and Slichter, L. B. "Problem of ice formation." *J. Applied Physics* 10 (1939): 135-137.
- [10] London, A. L. and Seban, R. A. "Rate of ice formation." *Transactions of the ASME* 65 (1943): 771-778.

- [11] Prusa, J. and Yao, L. S. "Effects of density change and sub-cooling on the melting of a solid around a horizontal heated cylinder." *J. Fluid Mechanics* 155 (1985): 193-212.
- [12] Kassinos, A. and Prusa, J. "Effects of density change and subcooling on the melting of a solid in a rectangular enclosure." *Proc. Int. Heat Transfer Conf.*, 8th, San Francisco, 4 (1986): 1787-1792.
- [13] Shah, R. K. and London, A. L. *Laminar Flow Forced Convection in Ducts*, Supplement 1 to *Advances in Heat transfer*. New York: Academic Press, 1978.
- [14] Shah, R.K. "Thermal entry length solutions for the circular tube and parallel plates." *Proc. Natl. Heat Mass Transfer Conf.*, 3rd, Indian Inst. Technol., Bombay, Vol. I, Pap. No. HMT-11-75 (1975).
- [15] Kays, W. M. "Numerical solutions for laminar flow heat transfer in circular tubes." *Trans. ASME* 77 (1955): 1265-1274.
- [16] Manglik, R. M. and Prusa, J. "An improved solution based on asymptotic analysis and numerical methods for the Graetz problem." Dept. of Mechanical Engineering Report No. ISU-ERI-Ames-88117, Iowa State University, Ames, Iowa, 1987.
- [17] Prusa, J. and Manglik, R. M. "Asymptotic and numerical solutions for thermally developing flows of Newtonian and non-Newtonian fluids in circular tubes with uniform wall temperature." *Fundamentals of Forced Convection Heat Transfer*, ASME HTD-Vol. 210 (1992).
- [18] Zerkle, R. D. and Sunderland, J. E. "The effect of liquid solidification in tube upon laminar-flow heat transfer and pressure drop." *J. Heat Transfer* 90 (1968): 183-190.
- [19] Yang, K. T. "Laminar forced convection of liquids in tubes with variable viscosity." *J. Heat Transfer* 84 (1962): 353-362.
- [20] Sellars, J. R.; Tribus, M.; and Klein, J. S. "Heat transfer to laminar flow in a round tube or flat conduit-The Graetz Problem Extended." *Transactions of the ASME* 78 (1956): 441-448.
- [21] Oliver, D. R. "The effect of natural convection on viscous-flow heat transfer in horizontal tubes." *Chemical Engineering Science* 17 (1962): 335-350.
- [22] Depew, C. A. and Zenter, R. C. "Laminar flow heat transfer and pressure drop with freezing at the wall." *Int. J. Heat Mass Transfer* 12 (1969): 1710-1714.

- [23] Mulligan, J. C. and Jones, D. D. "Experiments on heat transfer and pressure drop in a horizontal tube with internal solidification." *Int. J. Heat Mass Transfer* 19 (1976): 213-219.
- [24] Hwang, G. J. and Sheu, J. P. "Liquid solidification in combined hydrodynamic and thermal entrance region of a circular tube." *Canadian Journal of Chemical Engineering* 54 (1976): 66-71.
- [25] DesRuisseaux, N. and Zerkle, R. D. "Freezing of hydraulic systems." *Canadian Journal of Chemical Engineering* 47 (1969): 233-237.
- [26] Lock, G. S.; Freeborn, R. D. J.; and Nyren, R. H. "Analysis of ice formation in a convectively-cooled pipe." *Proc. Int. Heat Transfer Conf., 4th, Paris-Versailles* (1970): (Cu 2.9).
- [27] Hwang, G. J. and Yih, I. "Correction on the length of ice-free zone in a convectively-cooled pipe" *Int. J. Heat Transfer* 16 (1973): 681-683.
- [28] Arora, A. P. S. and Howell, J. R. "An investigation of the freezing of supercooled liquid in forced turbulent flow inside circular tubes." *Int. J. Heat Mass Transfer* 16 (1973): 2077-2084.
- [29] Thomason, S. B.; Mulligan, J. C.; and Everhart, J. "The effect of internal solidification on turbulent flow heat transfer and pressure drop in a horizontal tube." *J. Heat Transfer* 100 (1978): 387-394.
- [30] Sparrow, E. M.; Hallman, T. M.; and Siegel, R. "Turbulent heat transfer in the thermal entrance region of a pipe with a uniform heat flux." *Applied Science Review* 7 (1959): 37-52.
- [31] Kays, W. M. "Heat transfer: Turbulent flow inside smooth tubes." In *Convective Heat and Mass Transfer*. pp. 173-187. New York: McGraw-Hill, 1966.
- [32] Shibani, A. A. and Ozisik, M. N. "Freezing of liquids in turbulent flow inside tubes." *Canadian Journal of Chemical Engineering* 55 (1977): 672-677.
- [33] Shibani, A. A. and Ozisik, M. N. "A solution of freezing of liquids of low Prandtl number in turbulent flow between parallel plates." *J. Heat Transfer* 99 (1977): 20-24.
- [34] Lee, D. G. and Zerkle, R. D. "The effect of liquid solidification in a parallel plate channel upon laminar-flow heat transfer and pressure drop." *J. Heat Transfer* 91 (1969): 583-585.

- [35] Cheng, K. C. and Wong, S. L. "Liquid solidification in a convectively-cooled parallel-plate channel." *Canadian Journal of Chemical Engineering* 55 (1977): 149-155.
- [36] Ozisik, M. N. and Mulligan, J. C. "Transient freezing of liquids in forced flow inside circular tubes." *J. Heat Transfer* 91 (1969): 385-390.
- [37] Bilenas, J. A. and Jiji, L. M. "Numerical solution of a nonlinear free boundary problem of axisymmetric fluid flow in tubes with surface solidification." *Proc. Int. Heat Transfer Conf., 4th, Paris-Versailles (1970): (Cu 2.1).*
- [38] Martinez, E. P. and Beaubouef, R. T. "Transient freezing in laminar tube-flow." *Canadian Journal of Chemical Engineering* 50 (1972): 445-449.
- [39] Cho, C. and Ozisik, M. N. "Transient freezing of liquids in turbulent flow inside tubes." *J. Heat Transfer* 101 (1979): 465-468.
- [40] Sadeghipour, M. S.; Ozisik, M. N.; and Mulligan, J. C. "Transient freezing of a liquid in a convectively cooled tube." *J. Heat Transfer* 104 (1982): 316-322.
- [41] Stephan, K. "Influence of heat transfer on melting and solidification in forced flow." *Int. J. Heat Mass Transfer* 12 (1969): 199-214.
- [42] Gilpin, R. R. "The morphology of ice structure in a pipe at or near transition Reynolds numbers." *Heat Transfer-San Diego, A.I.Ch.E. Symposium Series* 75 (1979): 89-94.
- [43] Gilpin, R. R. "Ice formation in a pipe containing flows in the transition and turbulent regimes." *J. Heat Transfer* 103 (1981): 363-368.
- [44] Hirata, T.; Gilpin, R. R.; and Cheng, K. C. "The steady state ice layer profile on a constant temperature plat in a forced convection flow - II. The transition and turbulent regimes." *Int. J. Heat Mass Transfer* 22 (1979): 1435-1443.
- [45] Hirata, T.; Gilpin, R. R.; Cheng, K. C.; and Gates, E. M. "The steady state ice layer profile on a constant temperature plat in a forced convection flow - I. Laminar regime." *Int. J. Heat Mass Transfer* 22 (1979): 1425-1433.
- [46] Epstein, M. and Cheung, F. B. "On the prediction of pipe freeze-shut in turbulent flow." *J. Heat Transfer* 104 (1982): 381-384.
- [47] Hirata, T. and Ishihara, M. "Freezing-off conditions of a pipe containing a flow of water" *Int. J. Heat Mass Transfer* 28 (1985): 331-337.

- [48] Sparrow, E. M. and Ohkubo, Y. "Numerical analysis of two-dimensional transient freezing including solid-phase and tube-wall conduction and liquid-phase natural convection." *Numerical Heat Transfer*, 9 (1986): 59-77.
- [49] Sparrow, E. M. and Ohkubo, Y. "Numerical predictions of freezing in a vertical tube." *Numerical Heat Transfer* 9 (1986): 79-95.
- [50] Djilali, N.; Gartshore, I; and Salcudean, M. "Calculation of convective heat transfer in recirculating turbulent flow using various near-wall turbulence models." *Numerical Heat Transfer* 16 (1989): 189-212.
- [51] Albert, M. R. and Olfe, D. B. "A method for predicting freezing in forced flow." Presented at Winter Annual Meeting of ASME, Dallas, Texas, Nov. 25-30, 1990.
- [52] Seki, N.; Fukusako, S.; and Younan G. W. "Ice-formation phenomena for water flow between two cooled parallel plates." *J. Heat Transfer* 106 (1984): 498-505.
- [53] Gilpin, R. R. "A study of factors affecting the ice nucleation temperature in a domestic water supply." *The Canadian Journal of Chemical Engineering*, 56 (1978): 466-471.
- [54] Fant, D. B. "The numerical and analytical study of bifurcation and multicellular flow instability due to natural convection between narrow horizontal isothermal cylindrical annuli at high Rayleigh numbers." Ph.D. Dissertation. Iowa State University, Ames, Iowa, 1987.
- [55] Anderson, D. A., Tannehill, J. C.; and Pletcher, R. H. *Computational Fluid Mechanics and Heat transfer*. New York: McGraw-Hill Book Co., 1984.
- [56] Prusa, J. "A spatial Stefan problem modified by natural convection: Melting around a horizontal cylinder." Ph.D. Dissertation. University of Illinois, Urbana, Illinois, 1983.
- [57] Kassinos, A. K. "Melting in rectangular geometries in the presence of subcooling and density change effects." M.S. Thesis. Iowa State University, Ames, Iowa, 1986.
- [58] Roache, P. J. *Computational Fluid Dynamics*. Albuquerque, New Mexico: Hermosa, 1972.
- [59] Riley, D. S.; Smith, F. T.; and Poots, G. The inward solidification of spheres and circular cylinders. *Int. J. Heat Mass Transfer* 17 (1974): 1507-1515.

- [60] Schlichting, H. *Boundary-Layer Theory*, 7th ed. New York: McGraw-Hill Book Co., 1979.

ACKNOWLEDGMENTS

I wish to express my sincere gratitude to my major professor, Dr. Joseph M. Prusa, for his guidance during my Ph.D. program. I greatly appreciate the invaluable advice and inspiration that he provided throughout this dissertation. I also wish to extend my gratitude to Dr. Richard H. Pletcher, Dr. Gerald M. Colver, Dr. Bruce R. Munson, and Dr. Kenneth A. Heimes for their willingness to be committee members.

I have a list of unforgettable names who have helped me in innumerable ways: Dr. Bremner in Agronomy, Dr. Heimes in Mathematics, Professor Jenison and Dr. Day in Engineering Fundamentals and Multidisciplinary Design, and Dr. Okiishi in Mechanical Engineering, to name a few. Through these people, I had a variety of experiences, through which I learned a lot as a student and as an instructor.

I wish to thank my dear parents for their never-ending love and sacrifices for my family and me. I am also grateful to other families and relatives for their concern and encouragement.

Special thanks to my wife, Hye Jin: I am heartily indebted to her for her unselfish love, sacrifices, and sincere prayers. Her unfailing support and faith helped make this dissertation possible.

Finally, our two sons, John and David, have been the greatest source of happiness for both of us. We wish them to grow in God, to whom we give our thanks.

APPENDIX A. INITIAL STATES

Two cases of initial states are considered here. One is thermally and hydrodynamically fully developed flow and the other is developing flow.

A.1 General Governing Equations

A.1.1 Dimensional formulation

General governing equations for both initial states are the steady form of Equations (2.5) - (2.6) and (2.24) - (2.26). The dimensional governing equations using stream function and vorticity are:

$$\bar{\omega} = -\frac{1}{\bar{r}}\nabla^2\bar{f} + \frac{2}{\bar{r}^2}\frac{\partial\bar{f}}{\partial\bar{r}} \quad (\text{A.1})$$

$$\frac{1}{\bar{r}}J(\bar{f},\bar{\omega}) + \frac{\bar{\omega}}{\bar{r}^2}\frac{\partial\bar{f}}{\partial\bar{z}} = \nu\left(\nabla^2\bar{\omega} - \frac{\bar{\omega}}{\bar{r}^2}\right) \quad (\text{A.2})$$

$$\frac{1}{\bar{r}}J(\bar{f},\bar{T}_l) = \alpha_l\nabla^2\bar{T}_l \quad (\text{A.3})$$

$$0 = \alpha_s\nabla^2\bar{T}_s \quad (\text{A.4})$$

$$0 = -k_l\left(\frac{\partial\bar{T}_l}{\partial\bar{r}} - \bar{R}'\frac{\partial\bar{T}_l}{\partial\bar{z}}\right)\Bigg|_{\bar{r}=\bar{R}} + k_s\left(\frac{\partial\bar{T}_s}{\partial\bar{r}} - \bar{R}'\frac{\partial\bar{T}_s}{\partial\bar{z}}\right)\Bigg|_{\bar{r}=\bar{R}} \quad (\text{A.5})$$

where $J(\bar{f},\phi) = \frac{\partial\bar{f}}{\partial\bar{r}}\frac{\partial\phi}{\partial\bar{z}} - \frac{\partial\bar{f}}{\partial\bar{z}}\frac{\partial\phi}{\partial\bar{r}}$ for $\phi = \bar{\omega}$ or \bar{T}_l and $\nabla^2 = \frac{\partial^2}{\partial\bar{r}^2} + \frac{1}{\bar{r}}\frac{\partial}{\partial\bar{r}} + \frac{\partial^2}{\partial\bar{z}^2}$. Boundary conditions for each initial state are considered separately in the following sections.

A.1.2 Scale analysis

Before the governing equations (A.1) - (A.5) are nondimensionalized, the order of magnitude of each term can be compared using the scale analysis. This is done to simplify the formulation by ignoring relatively small terms in advance.

As an example, Equation (A.1) can be rearranged as:

$$\frac{\partial^2 \bar{f}}{\partial \bar{r}^2} - \frac{1}{\bar{r}} \frac{\partial \bar{f}}{\partial \bar{r}} + \frac{\partial^2 \bar{f}}{\partial \bar{z}^2} + \bar{r} \bar{\omega} = 0.$$

The orders of magnitude of four terms are obtained as:

$$\begin{aligned} \frac{\partial^2 \bar{f}}{\partial \bar{r}^2} &\sim \frac{\Delta \bar{f}}{(\Delta \bar{r})^2} \sim \frac{Ga^4/\mu}{a^2} \sim Ga^2/\mu \\ \frac{1}{\bar{r}} \frac{\partial \bar{f}}{\partial \bar{r}} &\sim \frac{1}{a} \frac{\Delta \bar{f}}{\Delta \bar{r}} \sim \frac{Ga^4/\mu}{a^2} \sim Ga^2/\mu \\ \frac{\partial^2 \bar{f}}{\partial \bar{z}^2} &\sim \frac{\Delta \bar{f}}{\Delta \bar{z}} \sim \frac{Ga^4/\mu}{(aPe)^2} \sim \frac{Ga^2/\mu}{Pe^2} \\ \bar{r} \bar{\omega} &\sim a \cdot \Delta \bar{\omega} \sim a \cdot Ga/\mu \sim Ga^2/\mu. \end{aligned}$$

Comparing these terms, all terms except the axial diffusion term have the same order of magnitude. The axial diffusion term is smaller than the other term by the order of Pe^{-2} . As a result, the axial diffusion term can be dropped from Equation (A.1), without a loss of accuracy. The application of the scale analysis for Equations (A.2) - (A.5) gives the same result.

The magnitude of Pe is considered for a forced flow of water, as an example. Peclet number can be expressed as the product of Reynolds number (Re) and Prandtl number (Pr). For a laminar or weakly turbulent flow, Re can be an order of 100 or 1000. Pr for water depends on the temperature, but it is of the order of 10 at low temperature. Therefore, Pe is an order of 1000 or 10000 for the present study. This allows the axial diffusion terms to be dropped from the governing equations.

A.1.3 Dimensionless formulation

The dimensionless governing equations are obtained by substituting dimensionless variables defined in Chapter 2 into Equations (A.1) - (A.5) after dropping $\frac{\partial^2 \phi}{\partial \bar{z}^2}$ terms. They can also be obtained by dropping the unsteady terms and Pe^{-2} terms from the dimensionless governing equations, (2.31) - (2.35). They are:

$$\frac{\partial^2 f}{\partial r_c^2} - \frac{1}{r_c} \frac{\partial f}{\partial r_c} + R^3 r_c \omega = 0 \quad (\text{A.6})$$

$$\begin{aligned} \frac{\partial^2 \omega}{\partial r_c^2} + \left(\frac{1}{r_c} + \frac{1}{r_c Pr} \frac{\partial f}{\partial z} \right) \frac{\partial \omega}{\partial r_c} - \frac{1}{r_c Pr} \frac{\partial f}{\partial r_c} \frac{\partial \omega}{\partial z} \\ - \frac{\omega}{r_c^2 Pr} \left(\frac{\partial f}{\partial z} - r_c \frac{R'}{R} \frac{\partial f}{\partial r_c} \right) - \frac{\omega}{r_c^2} = 0 \end{aligned} \quad (\text{A.7})$$

$$\frac{\partial^2 T_l}{\partial r_c^2} + \left(\frac{1}{r_c} + \frac{1}{r_c} \frac{\partial f}{\partial z} \right) \frac{\partial T_l}{\partial r_c} - \frac{1}{r_c} \frac{\partial f}{\partial r_c} \frac{\partial T_l}{\partial z} = 0 \quad (\text{A.8})$$

$$\frac{\partial^2 T_s}{\partial r_s^2} - \left(\frac{\epsilon}{1 - \epsilon r_s} \right) \frac{\partial T_s}{\partial r_s} = 0 \quad (\text{A.9})$$

$$\frac{Su}{1 - \epsilon} \frac{\partial T_l}{\partial r_c} \Big|_{r_c=1} + \frac{1}{\epsilon} \frac{\partial T_s}{\partial r_s} \Big|_{r_s=1} = 0 \quad (\text{A.10})$$

where Su is the superheat number as defined in Equation (2.36). Ste and λ do not appear in this steady formulation because they come into play only in transient calculation.

A.2 Fully Developed Flow Initial State

A.2.1 Boundary conditions

A fluid flow which is hydrodynamically and thermally fully developed is consistent with a uniform ice layer. Stream function and vorticity are uniform in the axial

direction, but the solid and liquid temperatures vary with the axial location. The radial boundary conditions are:

$$\bar{f} = 0 \quad \text{at } \bar{r} = 0 \quad \text{and} \quad \bar{f} = \frac{Ga^4}{16\mu} \quad \text{at } \bar{r} = \bar{R}_O \quad (\text{A.11})$$

$$\bar{\omega} = 0 \quad \text{at } \bar{r} = 0 \quad \text{and} \quad \bar{\omega} = -\frac{1}{\bar{R}_O} \left. \frac{\partial^2 \bar{f}}{\partial \bar{r}^2} \right|_{\bar{r}=\bar{R}_O} \quad \text{at } \bar{r} = \bar{R}_O \quad (\text{A.12})$$

$$\frac{\partial \bar{T}_l}{\partial \bar{r}} = 0 \quad \text{at } \bar{r} = 0 \quad \text{and} \quad \bar{T}_l = T_O \quad \text{at } \bar{r} = \bar{R}_O \quad (\text{A.13})$$

$$\frac{\partial \bar{T}_s}{\partial \bar{r}} = \frac{k_l}{k_s} \frac{\partial \bar{T}_l}{\partial \bar{r}} \quad \text{at } \bar{r} = \bar{R}_O \quad \text{and} \quad \bar{T}_s = T_O \quad \text{at } \bar{r} = \bar{R}_O \quad (\text{A.14})$$

where \bar{R}_O is the uniform radius of the solid-liquid interface and it is specified as constant *a priori* for the given flow boundary condition.

Substitution of the dimensionless variables defined in Section 2.3.1 results in the dimensionless radial boundary conditions (for all z):

$$f = 0 \quad \text{at } r_c = 0 \quad \text{and} \quad f = \frac{1}{4} \quad \text{at } r_c = 1 \quad (\text{A.15})$$

$$\omega = 0 \quad \text{at } r_c = 0 \quad \text{and} \quad \omega = -\frac{1}{R_O^3} \left. \frac{\partial^2 f}{\partial r_c^2} \right|_{r_c=1} \quad \text{at } r_c = 1 \quad (\text{A.16})$$

$$\frac{\partial T_l}{\partial r_c} = 0 \quad \text{at } r_c = 0 \quad \text{and} \quad T_l = 0 \quad \text{at } r_c = 1 \quad (\text{A.17})$$

$$\left. \frac{\partial T_s}{\partial r_s} \right|_{r_s=1} = -Su \frac{\epsilon_O}{1 - \epsilon_O} \left. \frac{\partial T_l}{\partial r_c} \right|_{r_c=1} \quad \text{at } r_s = 1 \quad \text{and} \quad T_s = 1 \quad \text{at } r_s = 1 \quad (\text{A.18})$$

where $R_O = \frac{\bar{R}_O}{a}$ and $\epsilon_O = 1 - R_O$. R_O and ϵ_O are the uniform dimensionless radius of solid-liquid interface and ice layer thickness, respectively. Since R_O is specified constant *a priori*, a governing equation for R or ϵ is not needed. The interface equation, Equation (A.10), thus takes on the role of a boundary condition, Equation (A.18).

A.2.2 Reduced form of governing equations

For the fully developed flow with the uniform ice layer, the governing equations (A.6) - (A.9) are reduced to:

$$\frac{\partial^2 f}{\partial r_c^2} - \frac{1}{r_c} \frac{\partial f}{\partial r_c} + R_o^3 r_c \omega = 0 \quad (\text{A.19})$$

$$\frac{\partial^2 \omega}{\partial r_c^2} + \frac{1}{r_c} \frac{\partial \omega}{\partial r_c} - \frac{\omega}{r_c^2} = 0 \quad (\text{A.20})$$

$$\frac{\partial^2 T_l}{\partial r_c^2} + \frac{1}{r_c} \frac{\partial T_l}{\partial r_c} - \frac{1}{r_c} \frac{\partial f}{\partial r_c} \frac{\partial T_l}{\partial z} = 0 \quad (\text{A.21})$$

$$\frac{\partial^2 T_s}{\partial r_s^2} - \left(\frac{\epsilon_o}{1 - \epsilon_o r_s} \right) \frac{\partial T_s}{\partial r_s} = 0 \quad (\text{A.22})$$

Note that the axial derivatives of stream function, vorticity, and solid-liquid interface have all disappeared. R' terms drop from the governing equations because the ice layer thickness is uniform throughout the test section. And stream function and vorticity are independent of z for fully developed flow.

A.2.3 Analytical solution

Analytical solution can be obtained using the governing equations (A.19) - (A.22) and the boundary conditions (A.15) - (A.18). Since the stream function and vorticity equations are decoupled from the energy equations, their analytical solutions are determined separately.

A.2.3.1 Stream function and vorticity Equations (A.19) and (A.20) lead to the following solutions for stream function and vorticity:

$$f_o = \frac{1}{4}(2r_c^2 - r_c^4) \quad (\text{A.23})$$

$$\omega_o = \frac{2r_c}{R_o^3}. \quad (\text{A.24})$$

The subscript o indicates the analytical solution for the fully developed flow initial condition with the uniform ice layer. Note the appearance of R_o^3 in the vorticity solution. This term appears due to the increase in axial velocity which occurs when ice appears compared to the case of no ice. Stream function remains same as the inlet condition with no ice.

A.2.3.2 Liquid temperature The analytical solution for the liquid temperature can be obtained as following. In addition to dimensionless liquid temperature, two more dimensionless temperatures are defined as:

$$T^* = \frac{\bar{T}_l - T_o}{\bar{T}_m - T_o} \quad (\text{dimensionless self-similar temperature})$$

and

$$T_m = \frac{\bar{T}_m - T_o}{T_{io} - T_o} \quad (\text{dimensionless bulk mean temperature})$$

where \bar{T}_m is bulk mean temperature as a function of \bar{z} and T_{io} is the inlet liquid PCM temperature at the center. Using these dimensionless temperatures, the dimensionless liquid temperature can be rewritten as

$$T_{lo} = \frac{\bar{T}_l - T_o}{T_{io} - T_o} = T^* T_m. \quad (\text{A.25})$$

Here T^* is a function of r_c only and T_m^* is a function of z only. The dimensionless bulk mean temperature T_m is calculated from the energy balance for a small cylindrical control volume within the flow passage to be

$$T_m = \exp(-2Nu z) \frac{\bar{T}_{mo} - T_o}{T_{io} - T_o} \quad (\text{A.26})$$

where

$$Nu = \frac{2\bar{R}_o h}{k_l} = -\frac{2}{T_m} \left. \frac{\partial T_l}{\partial r_c} \right|_{r_c=1}$$

h is the convection heat transfer coefficient at the solid-liquid interface. The ratio term appearing in Equation (A.26) is the reciprocal of $T^*(0)$. Substituting these into Equation (A.25), the dimensionless liquid temperature is obtained as:

$$T_{lo} = \exp(-2Nu z) \frac{T^*(r_c)}{T^*(0)} \quad (\text{A.27})$$

where T_{lo} indicates the analytical liquid temperature for the fully developed flow initial condition with the uniform ice layer. T_{lo} ranges between 1 and 0 at $z = 0$ and decreases exponentially with z .

The self-similar temperature T^* must be determined to complete the analytical solution for liquid temperature. For the fully developed flow, the dimensionless liquid energy equation (A.21) is reduced to:

$$\frac{\partial^2 T_{lo}}{\partial r_c^2} + \frac{1}{r_c} \frac{\partial T_{lo}}{\partial r_c} - (1 - r_c^2) \frac{\partial T_{lo}}{\partial z} = 0 \quad (\text{A.28})$$

Here Equation (A.23) has been used to evaluate the velocity coefficient of the convective term. Finally substituting Equation (A.27) into Equation (A.28) results in an ordinary differential equation:

$$\frac{1}{r_c} \frac{d}{dr_c} \left(r_c \frac{dT^*}{dr_c} \right) = -2Nu(1 - r_c^2)T^* \quad (\text{A.29})$$

with the boundary conditions:

$$\frac{dT^*}{dr_c} = 0 \quad \text{at} \quad r_c = 0 \quad \text{and} \quad T^* = 0 \quad \text{at} \quad r_c = 1$$

This equation is solved numerically using fourth-order Runge-Kutta method. This completes the analytical solution for the liquid temperature. Table A.1 lists the

Table A.1: Dimensionless liquid temperature for the thermally fully developed flow

r_c	T^*	$\frac{dT^*}{dr_c}$
0.000	1.8026013	0.0000000
0.050	1.7943909	-0.3283711
0.100	1.7698909	-0.6498993
0.150	1.7296282	-0.9578069
0.200	1.6744404	-1.2459271
0.250	1.6054569	-1.5087934
0.300	1.5240588	-1.7418321
0.350	1.4318304	-1.9415068
0.400	1.3305049	-2.1054138
0.450	1.2219062	-2.2323293
0.500	1.1078899	-2.3222068
0.550	0.9902853	-2.3761296
0.600	0.8708413	-2.3962220
0.650	0.7511766	-2.3855291
0.700	0.6327381	-2.3478727
0.750	0.5167650	-2.2876933
0.800	0.4042627	-2.2098899
0.850	0.2959831	-2.1196663
0.900	0.1924135	-2.0223945
0.950	0.0937706	-1.9235034
1.000	0.0000000	-1.8284008

dimensionless temperature T^* distribution and its derivatives obtained numerically. The step size used for this table is 0.003125. Nu for the thermally fully developed flow can be calculated using the data from Table A.1 as follows:

$$Nu = -\frac{2}{T_m} \left. \frac{\partial T_l}{\partial r_c} \right|_{r_c=1} = -2 \left. \frac{dT^*}{dr_c} \right|_{r_c=1} = -2 \times (-1.8284008) = 3.6568.$$

This matches very well with the analytical solution. Figure A.1 shows the dimensionless liquid temperature profile for the thermally fully developed flow.

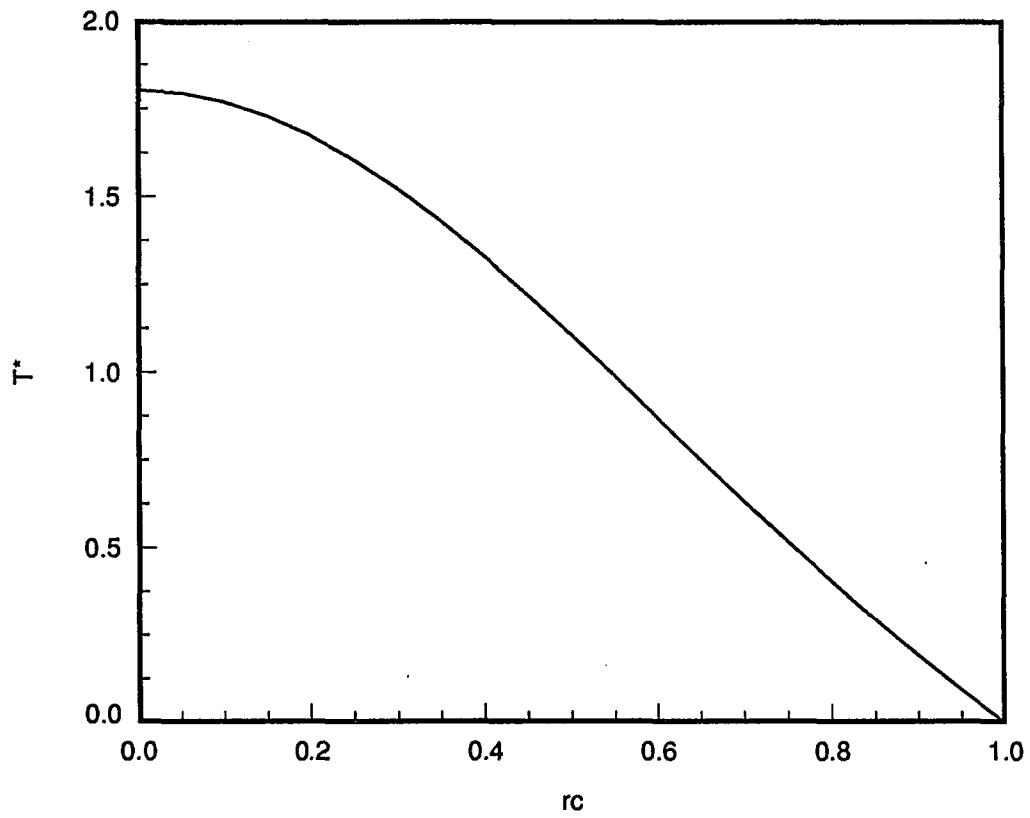


Figure A.1: Dimensionless liquid temperature profile for the thermally fully developed flow

A.2.3.3 Solid temperature and the ice layer thickness For the fully developed flow, Equation (A.22) can be solved using the separation of variables method. Separating variables and integrating twice with two boundary conditions (A.18) and introducing T^* through Equation (A.27), the dimensionless solid temperature is obtained as:

$$T_{s0} = 1 - Su \frac{\exp(-2Nu z)}{T^*(0)} \left. \frac{dT^*}{dr_c} \right|_{r_c=1} \ln \left(\frac{1 - \epsilon_o}{1 - \epsilon_o r_s} \right) \quad (\text{A.30})$$

where T_{s0} indicates the analytical solid temperature for the fully developed flow initial condition with the uniform ice layer. T_{s0} ranges between 1 and 0 at $z = 0$ and its value at the wall increases exponentially with z .

The thickness of the ice layer can be calculated from Equation (A.30) for the given flow boundary condition, which is represented by the Su number. Substituting $T_s = 0$ at $z = 0$ and $r_s = 0$ gives:

$$\epsilon_o = 1 - \exp \left(\frac{1}{Su} \frac{T^*(0)}{\left. \frac{dT^*}{dr_c} \right|_{r_c=1}} \right) \quad (\text{A.31})$$

From Table A.1:

$$T^*(0) = 1.8026013 \quad \text{and} \quad \left. \frac{\partial T^*}{\partial r_s} \right|_{r_c=1} = -1.8284008$$

Substituting these and $R_o = 1 - \epsilon_o$ into Equation (A.31) gives

$$R_o = \exp \left(\frac{-0.9858896}{Su} \right) \quad (\text{A.32})$$

This equation is used to calculate the uniform radius of solid-liquid interface for the given flow boundary condition, Su .

Equations (A.23), (A.24), (A.27), (A.30), and (A.31) give the complete analytical solution for the fully developed flow initial state.

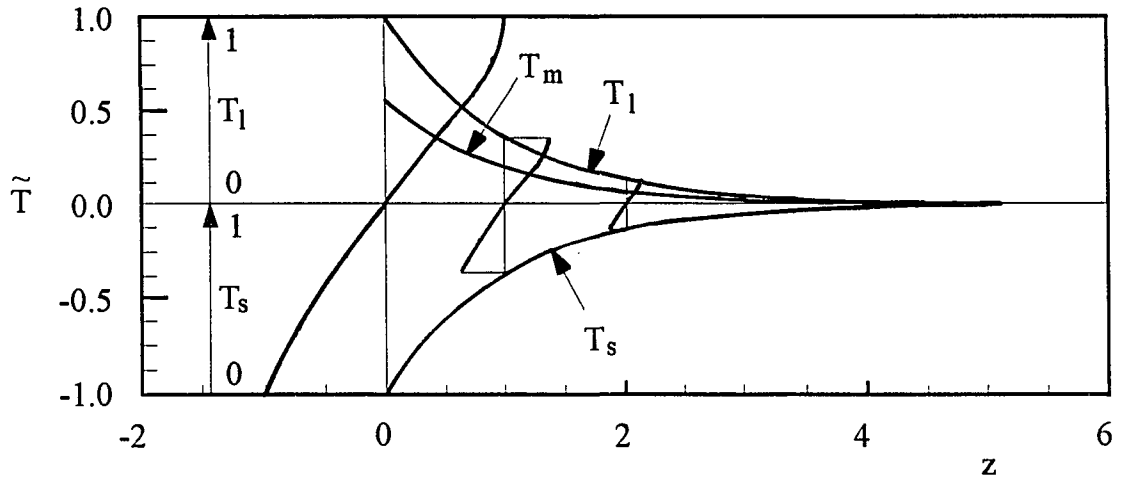
Table A.2 lists the uniform radius of solid-liquid interface calculated using Equation (A.32) for $0.2 \leq Su \leq 20$. As Su increases, which physically means the liquid becomes warmer, the flow passage becomes wider and ice layer thickness becomes thinner. Figure A.2 shows the dimensionless liquid and solid temperature distributions as a function of z for (a) $Su = 2$ and (b) $Su = 20$. The liquid temperature at the center of the pipe (uppermost curve) and the solid temperature at the wall vary exponentially with z , as well as the liquid bulk mean temperature. In order to visualize the temperature variations more physically, vertical axis is defined as

$$\tilde{T} = T_l \text{ or } (T_s - 1)$$

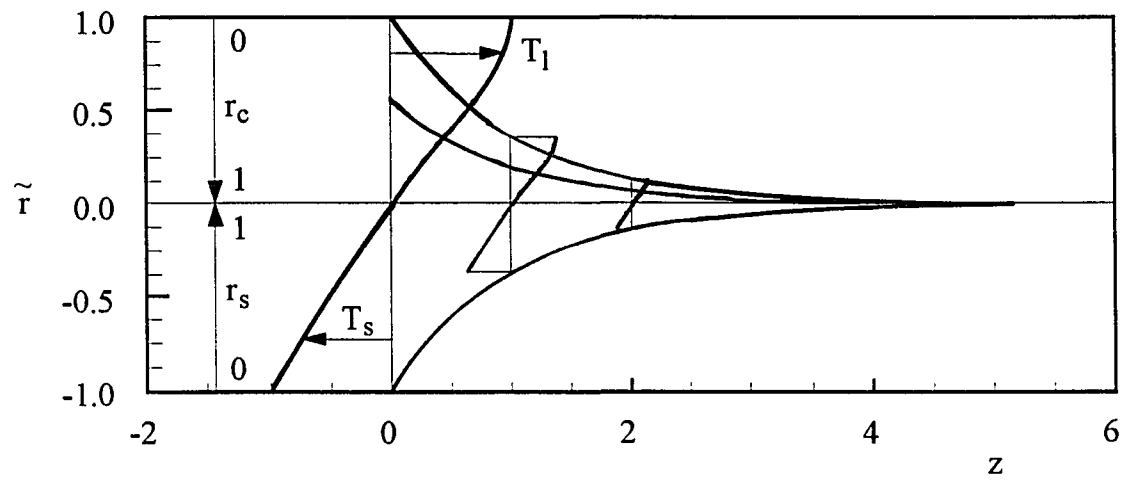
where \tilde{T} varies from -1 (solid temperature at the wall) to 1 (liquid temperature at the centerline) at $z = 0$. As z increases, these boundary values decrease in magnitude and the liquid and solid temperatures are within these limit values. In addition to the axial variation of temperature, Figure A.2 shows the temperature profiles at $z = 0, 1$, and 2 . These radial temperature variations are plotted versus another newly defined vertical axis (see Figure (b)):

$$\tilde{r} = (1 - r_c) \text{ or } (r_s - 1)$$

which varies from -1 at the pipe wall to 1 at the centerline. The scale on the left axis applies to the profile at $z = 0$, and it must be shrunk according to the boundary temperatures. Figure A.2 (a) shows the temperature profiles with thick ice layer ($\epsilon = 0.389$) and Figure A.2 (b) shows those with thin ice layer ($\epsilon = 0.048$). The liquid temperature profile is independent of the radius of the solid-liquid interface, whereas the solid temperature profile becomes linear as the ice becomes thinner.



(a) $Su = 2.0, \epsilon_0 = 0.389$



(b) $Su = 20.0, \epsilon_0 = 0.048$

$$\tilde{T} = T_l \text{ or } T_s - 1, \quad \tilde{r} = 1 - r_c \text{ or } r_s - 1$$

Figure A.2: Initial distributions of solid and liquid temperatures for the thermally fully developed flow

Table A.2: Initial uniform radius of solid-liquid interface

Su	0.2	0.5	1	2	5	10	20
R_0	0.00723	0.13921	0.37311	0.61082	0.82104	0.90612	0.95190

A.2.4 Numerical solution

Even though there exists a closed form analytical solution for fully developed flow initial state, a numerical solution for the initial state is needed. This is because if the analytical initial state is fed into a numerical transient calculation, there will be unsteadiness (due to truncation error) even without a change of boundary conditions. A numerical initial state must be obtained by numerically solving Equations (A.6) - (A.10) so that when it is input into the numerical transient calculation, no change in the solution will occur unless the boundary conditions are changed. The analytical solution is used to give good initial values of dependent variables for the numerically determined initial condition.

First, the dimensionless temperature T^* is calculated by solving the ordinary differential equation (A.29). The method used here is the fourth-order Runge-Kutta method. Once the dimensionless temperature T^* is determined, the initial radius of the solid-liquid interface R_0 is calculated from Equation (A.32). Then, using this R_0 , initial distributions of f , ω , T_l , and T_s are obtained analytically from Equations (A.23), (A.24), (A.27) and (A.30). These analytically obtained values become the initially guessed values for the Gauss-Seidel iterative method to solve Equations (A.19) - (A.22) numerically. The iteration sequence and the general numerical method are same as in Chapter 3.

At the inlet ($z = 0$ or $j = 0$), the axial temperature gradient is given by the

analytical solution: derivative of Equation (A.27):

$$\frac{\partial T_l}{\partial z} = -2Nu T_l$$

For values of $z > 0$ ($j > 0$), $\frac{\partial T}{\partial z}$ is determined numerically. Once the converged inlet condition is obtained, computation marches in axial direction to calculate the numerical solutions for T_l and T_s at each axial node ($j = 1$ to $j = nz$) while ϵ , f , and ω remain the same as the values at the initial axial node ($j = 0$). Although the iterative scheme tests the convergence of the dependent variables, it was found that the heat fluxes (liquid versus solid values) at the solid-liquid interface could be gravely out of balance. In order to balance the heat flux at the solid-liquid interface, an iterative scheme for interface energy balance was added as follows. The objective of this scheme is to satisfy Equation (A.10). Set

$$\Delta = \frac{Su}{1 - \epsilon_o} \left. \frac{\partial T_l}{\partial r_c} \right|_{r_c=1} + \frac{1}{\epsilon_o} \left. \frac{\partial T_s}{\partial r_s} \right|_{r_s=1}$$

where the first term is negative and the second term is positive. When the heat fluxes are unbalanced,

$$\left. \frac{\partial T_l}{\partial r_c} \right|_{r_c=1} = \left(\Delta - \frac{1}{\epsilon_o} \left. \frac{\partial T_s}{\partial r_s} \right|_{r_s=1} \right) \frac{1 - \epsilon_o}{Su}. \quad (\text{A.33})$$

When the heat fluxes are balanced, $\Delta = 0$, therefore

$$\left. \frac{\partial T_l}{\partial r_c} \right|_{r_c=1} = - \frac{1}{\epsilon_o} \left. \frac{\partial T_s}{\partial r_s} \right|_{r_s=1} \frac{1 - \epsilon_o}{Su}. \quad (\text{A.34})$$

Subtracting Equation (A.33) from Equation (A.34),

$$\delta \left(\left. \frac{\partial T_l}{\partial r_c} \right|_{r_c=1} \right) = -\Delta \frac{1 - \epsilon_o}{Su}. \quad (\text{A.35})$$

The solid temperature at the pipe wall can be evaluated from Equation (A.30), with $r_s = 0$ at the wall, as

$$\begin{aligned} T_{s,w} &= 1 - Su \frac{\exp(-2Nu z)}{T^*(0)} \left. \frac{dT^*}{dr_c} \right|_{r_c=1} \ln(1 - \epsilon_o) \\ &= 1 - Su \left. \frac{\partial T_l}{\partial r_c} \right|_{r_c=1} \ln(1 - \epsilon_o) \end{aligned} \quad (\text{A.36})$$

where $T_{s,w}$ denotes the solid temperature at the pipe wall. Taking a finite (but small) differential of Equation (A.36),

$$\begin{aligned} \delta(T_{s,w}) &= -Su \delta \left(\left. \frac{\partial T_l}{\partial r_c} \right|_{r_c=1} \right) \ln(1 - \epsilon_o) \\ &= \Delta(1 - \epsilon_o) \ln(1 - \epsilon_o) \end{aligned} \quad (\text{A.37})$$

Now, the pipe wall temperature is corrected as

$$T_{s,w}^{new} = T_{s,w}^{old} + \delta(T_{s,w}) = T_{s,w}^{old} + \Delta(1 - \epsilon_o) \ln(1 - \epsilon_o) \quad (\text{A.38})$$

Equation (A.38) is used to adjust the pipe wall temperature to balance the heat fluxes at the solid-liquid interface. Convergence was judged upon behavior of T_s . The converged values of dependent variables at all axial nodes become the initial conditions for the transient calculation.

A.3 Developing Flow Initial State

For an isothermal pipe wall boundary condition, the ice layer thickness increases with axial location. When the wall temperature of the test section (originally at uniform superheat) is lowered to T_w , which is uniform in \bar{z} and below the freezing temperature, ice starts to grow inwardly from the pipe wall along the test section.

Provided that the liquid carries sufficient sensible heat, the ice layer grows asymptotically to a steady state, in which ice layer thickness is increasing axially throughout the test section. This steady state is considered as an initial condition.

The ice layer is divided into two intervals. One is for small z , where the ice layer thickness is so thin that it has negligible effect on the hydrodynamic field. The other, for large z , is where the ice layer has significant effect on it. The thin ice layer is assumed up to a certain axial location $\bar{z} = \bar{z}_{tr}$, and after that point ice thickness is not regarded as thin any more.

The governing equations given in Section A.1.3 and the boundary conditions given in Section 2.3.3 apply to both intervals, but two intervals need to be treated differently. For a thin ice layer interval (for small z), a thin thermal boundary layer exists. Therefore the liquid temperature equation is solved in boundary layer scale, which requires a modified formulation. For the thick ice layer interval (for large z), the thermal boundary layer grows to the same order of magnitude as the pipe radius. So the core radial scale is appropriate to be used.

A.3.1 Boundary layer formulation for small z

The dimensionless variables are defined same as in Chapter 2, with the exception of radial scale for liquid PCM.

$$r_b = \frac{\bar{R} - \bar{r}}{\bar{\delta}} \quad \text{and} \quad \delta = \frac{\bar{\delta}}{\bar{R}}$$

where $\bar{\delta}$ is the thickness of the thermal boundary layer. Boundary layer coordinate r_b varies from 0 at the solid-liquid interface to 1 at the thermal boundary layer edge. The dimensionless liquid temperature varies as the same within the boundary

layer and is 1 in the core region, where liquid temperature is at the uniform inlet temperature.

Using the boundary layer coordinates, the dimensionless governing equations are rewritten as:

$$\frac{\partial^2 f}{\partial r_b^2} + \left(\frac{\delta}{1 - \delta r_b} \right) \frac{\partial f}{\partial r_b} + R^3 \delta^2 (1 - \delta r_b) \omega = 0 \quad (\text{A.39})$$

$$\begin{aligned} \frac{\partial^2 \omega}{\partial r_b^2} - \left(\frac{\delta}{1 - \delta r_b} \right) \frac{\partial \omega}{\partial r_b} - \frac{1}{Pr} \left(\frac{\delta}{1 - \delta r_b} \right) J_b(f, \omega) - \frac{\omega}{Pr} \left(\frac{\delta}{1 - \delta r_b} \right)^2 \frac{\partial f}{\partial z} \\ + \frac{\omega}{Pr} \left\{ \frac{r_b \delta \delta'}{(1 - \delta r_b)^2} - \left(\frac{\delta}{1 - \delta r_b} \right) \frac{R'}{R} \right\} \frac{\partial f}{\partial r_b} - \omega \left(\frac{\delta}{1 - \delta r_b} \right)^2 = 0 \end{aligned} \quad (\text{A.40})$$

$$\frac{\partial^2 T_l}{\partial r_b^2} + \left(\frac{\delta}{1 - \delta r_b} \right) J_b(f, T_l) - \left(\frac{\delta}{1 - \delta r_b} \right) \frac{\partial T_l}{\partial r_b} = 0 \quad (\text{A.41})$$

$$\frac{\partial^2 T_s}{\partial r_s^2} - \left(\frac{\epsilon}{1 - \epsilon r_s} \right) \frac{\partial T_s}{\partial r_s} = 0 \quad (\text{A.42})$$

$$\frac{Su}{1 - \epsilon} \frac{\partial T_l}{\partial r_b} \Big|_{r_b=0} - \frac{\delta}{\epsilon} \frac{\partial T_s}{\partial r_s} \Big|_{r_s=1} = 0 \quad (\text{A.43})$$

where $J_b(f, \phi) = \frac{\partial f}{\partial r_b} \frac{\partial \phi}{\partial z} - \frac{\partial f}{\partial z} \frac{\partial \phi}{\partial r_b}$ and $\delta' = \frac{\partial \delta}{\partial z}$. The only assumptions used here are steady flow and high Pe number.

The radial boundary conditions are (for all z):

$$f \longrightarrow 0 \quad \text{as } r_b \longrightarrow \infty \quad \text{and} \quad f = \frac{1}{4} \quad \text{at } r_b = 0 \quad (\text{A.44})$$

$$\omega \longrightarrow 0 \quad \text{as } r_b \longrightarrow \infty \quad \text{and} \quad \omega = - \frac{1}{R^3 \delta^2} \frac{\partial^2 f}{\partial r_b^2} \Big|_{r_b=0} \quad \text{at } r_b = 0 \quad (\text{A.45})$$

$$T_l \longrightarrow 1 \quad \text{as } r_b \longrightarrow \infty \quad \text{and} \quad T_l = 0 \quad \text{at } r_b = 0 \quad (\text{A.46})$$

$$T_s = 0 \quad \text{at } r_s = 0 \quad \text{and} \quad T_s = 1 \quad \text{at } r_s = 1 \quad (\text{A.47})$$

A.3.2 Asymptotic solution for small z

Since $\epsilon \rightarrow 0$ as $z \rightarrow 0$, an asymptotic solution for small z can be obtained by ignoring the effect of the thin ice layer.

A.3.2.1 Stream function and vorticity When the ice layer thickness is ignored, the hydrodynamic field can be assumed to be fully developed and stream function and vorticity for small z can be approximated by the inlet condition. Therefore, the asymptotic solutions for stream function and vorticity are: (in core scale)

$$f_a = \frac{1}{4}(2r_c^2 - r_c^4) \quad (\text{A.48})$$

$$\omega_a = 2r_c \quad (\text{A.49})$$

where the subscript a indicates the asymptotic solution for small z .

These solutions can be rewritten in boundary layer scale using the relation between boundary layer and core radial scales: $r_c = 1 - \delta r_b$. They become

$$f_a(r_b, z) = \frac{1}{4} - \delta^2 r_b^2 \left(1 - \frac{1}{2}\delta r_b\right)^2 \quad (\text{A.50})$$

$$\omega_a(r_b, z) = 2(1 - \delta r_b) \quad (\text{A.51})$$

Here $f_a(r_b, z)$ and $\omega_a(r_b, z)$ indicate that they are functions of r_b and z , whereas f_a and ω_a in core scale are functions of only r_c . The z variation in boundary layer coordinates is implicit in δ , which will be specified in next page, Equation (A.55).

A.3.2.2 Liquid temperature The asymptotic solution for the liquid temperature can be obtained as following using the asymptotic stream function in boundary layer coordinates. Equation (A.41) can be rearranged as:

$$\frac{\partial^2 T_l}{\partial r_b^2} - \left(\frac{\delta}{1 - \delta r_b} - \frac{\delta}{(1 - \delta r_b)} \frac{\partial f}{\partial z} \right) \frac{\partial T_l}{\partial r_b} + \frac{\delta}{(1 - \delta r_b)} \frac{\partial f}{\partial r_b} \frac{\partial T_l}{\partial z} = 0$$

The substitution of $\frac{\partial f_a}{\partial z}$ and $\frac{\partial f_a}{\partial r_b}$ into this equation results in

$$\frac{\partial^2 T_{la}}{\partial r_b^2} - \left(\frac{\delta}{1 - \delta r_b} - r_b^2 \delta^2 \delta' (2 - \delta r_b) \right) \frac{\partial T_{la}}{\partial r_b} - r_b \delta^3 (2 - \delta r_b) \frac{\partial T_{la}}{\partial z} = 0 \quad (\text{A.52})$$

subject to

$$T_{la} = 0 \text{ at } r_b = 0 \quad \text{and} \quad T_{la} \longrightarrow 1 \text{ as } r_b \longrightarrow \infty \quad (\text{A.53})$$

where T_{la} indicates the asymptotic liquid temperature for small z . Now Equation (A.52) is solved for the liquid temperature of the thermally developing flow subject to boundary conditions (A.53). This is the well known Graetz problem.

An initial condition (at $z = 0^+$) for the dimensionless liquid temperature is required to complete the formulation for the Graetz problem. The appropriate initial condition can be obtained from Equation (A.52) by examining its limiting form as the test section inlet is approached. Since $\delta \longrightarrow 0$ as $z \longrightarrow 0$, it follows that as the inlet is approached, the small terms in δ may be dropped. The following limiting form of Equation (A.52) results:

$$\frac{\partial^2 T_{la}^+}{\partial r_b^2} + 2r_b^2 \delta^2 \delta' \frac{\partial T_{la}^+}{\partial r_b} = 0 \quad (\text{A.54})$$

where the superscript $^+$ indicates the limiting solution as $z \longrightarrow 0$. Here, the first term represents radial diffusion and the second term represents axial convection. A balance of these two terms requires $\delta^2 \delta'$ to be a constant independent of z , thereby implying

$$\delta = (Cz)^{\frac{1}{3}} \quad (\text{A.55})$$

where C is a free parameter to be determined experimentally. An immediate result of the required functional form for δ is that T_{la}^+ is a function only of r_b . Substitution

of (A.55) into Equation (A.54) results in:

$$\frac{d^2 T_{la}^+}{dr_b^2} + \frac{2}{3} Cr_b^2 \frac{dT_{la}^+}{dr_b} = 0 \quad (\text{A.56})$$

where the applicable boundary conditions are those given by Equation (A.53). Thus in the limit $\delta \rightarrow 0$ as $z \rightarrow 0$, T_{la}^+ can be readily found to be:

$$T_{la}^+(r_b) = 1.119847 \int_0^{\left(\frac{2}{9}C\right)^{\frac{1}{3}} r_b} \exp(-\zeta^3) d\zeta \quad (\text{A.57})$$

where ζ is the dummy variable of the integration. This is the analytical initial condition to Equation (A.52).

Equations (A.52), (A.53), and (A.57) completely determine the asymptotic liquid temperature for small z .

A.3.2.3 Solid temperature and ice layer thickness The solid temperature and the ice layer thickness for small z are obtained by solving Equations (A.42) and (A.43) simultaneously with the boundary condition (A.47) using the asymptotic liquid temperature determined in the preceding section (A.3.2.2).

The initial condition (at $z = 0^+$) for the solid temperature can be obtained similarly as for the liquid temperature. Since $\epsilon \rightarrow 0$ as $z \rightarrow 0$, Equation (A.42) is reduced to

$$\frac{\partial^2 T_{sa}^+}{\partial r_s^2} = 0 \quad (\text{A.58})$$

where the subscript a and superscript $+$ have the same meaning as for liquid temperature.

Equation (A.58) and the boundary condition (A.47) result in

$$T_{sa}^+ = r_s \quad (\text{A.59})$$

Then, as $z \rightarrow 0$, Equation (A.43) is reduced to

$$Su \frac{\partial T_{la}^+}{\partial r_b} \Big|_{r_b=0} - \frac{\delta}{\epsilon_a^+} \frac{\partial T_{sa}^+}{\partial r_s} \Big|_{r_s=1} = 0$$

where $\frac{\delta}{\epsilon_a^+}$ remains because it is of order 1. This equation can be rearranged to solve for the ϵ_a^+ as:

$$\epsilon_a^+ = \frac{\delta \frac{\partial T_{sa}^+}{\partial r_s} \Big|_{r_s=1}}{Su \frac{\partial T_{la}^+}{\partial r_b} \Big|_{r_b=0}} \quad (\text{A.60})$$

The derivatives are obtained from Equations (A.57) and (A.59) as:

$$\frac{\partial T_{la}^+}{\partial r_b} \Big|_{r_b=0} = 1.119847 \left(\frac{2}{9} C \right)^{\frac{1}{3}} \quad \text{and} \quad \frac{\partial T_{sa}^+}{\partial r_s} \Big|_{r_s=1} = 1$$

Substitution of these derivatives and Equation (A.55) into Equation (A.60) results in

$$\epsilon_a^+ = \frac{1.474276}{Su} z^{\frac{1}{3}} \quad (\text{A.61})$$

Equations (A.59) and (A.61) are asymptotic solutions for solid temperature and ice layer thickness as $z \rightarrow 0$. Note that solid temperature and ice layer thickness are independent of the free parameter C .

A.3.2.4 The role of free parameter C The initial liquid temperature given by Equation (A.57) depends on the free parameter C . This seems to indicate that the whole solution will be dependent on C . Such a dependency violates the physics of the problem, however. Consequently, if the formulation is to be of any use, the solutions which are generated must be relatively insensitive to the precise values of C over some broad interval of reasonable values. From Equation (A.55), it is seen

that C is a stretching or growth parameter for the boundary layer. Physically small values of C correspond to thin boundary layers while large values of C correspond to thick ones.

The choice of reasonable C values can be considered by examining the temperature profiles obtained using the parameter C . The temperature should satisfy the boundary conditions (A.53). The first boundary condition is obviously satisfied. In the present numerical solution, the second boundary condition is modified to $T_{la} = 1$ at $r_b = 1$ (the edge of the boundary layer). Thus C must be chosen sufficiently large so that $T_{la}^+(1)$ as predicted by Equation (A.57) lies very close to 1. However, if C is chosen too big, liquid temperature approaches 1 too fast and the temperature is not properly distributed within the boundary layer. $T_{la}^+(1)$ can be calculated by setting $r_b = 1$ in Equation (A.57) and the numerical results are given in Table A.3. Table A.3 shows that $T_{la}^+(1) \geq 0.995$ for $C \geq 15$ and $\frac{\partial T_{la}^+}{\partial r_b}(1) \leq 0.008$ for $C \geq 25$.

Figure A.3 shows the liquid temperature distributions in the boundary layer, which were calculated numerically using $C = 25$. The solid line is the temperature profile at $z = 0$, which matches the asymptotic solution exactly. The dashed line is the profile at $z_{tr} = 10^{-5}$, where small z solution is switched to large z solution. The figure shows that the liquid temperature profile does not change much within small z interval. Figure A.4 shows the numerically calculated thicknesses of thermal boundary layer and ice layer, which increase with axial coordinate as a function of $z^{1/3}$. Su used for this calculation is 1.0. The plot also indicates that the thermal boundary layer and the ice layer thicknesses are about 6% and 3% of the pipe radius at $z = z_{tr}$, respectively.

Table A.3: Effect of free parameter C upon the asymptotic liquid temperature

C	$\int_0^{\left(\frac{2}{9}C\right)^{\frac{1}{3}}r_b} \exp(-\zeta^3) d\zeta$	$T_{la}^+(1)$	$\frac{dT_{la}^+}{dr_b}(1)$
1.0	0.5740841	0.6428864	0.5431394
2.0	0.6880835	0.7705483	0.5479548
3.0	0.7518933	0.8420055	0.5022639
4.0	0.7925112	0.8874913	0.4426580
5.0	0.8199551	0.9182243	0.3818227
6.0	0.8391548	0.9397250	0.3248969
7.0	0.8528979	0.9551152	0.2738743
8.0	0.8628962	0.9663118	0.2292831
9.0	0.8702588	0.9745568	0.1909471
10.0	0.8757317	0.9806855	0.1583637
15.0	0.8883962	0.9948678	0.0596765
20.0	0.8916932	0.9985599	0.0216222
25.0	0.8926067	0.9995829	0.0076675
30.0	0.8928691	0.9998768	0.0026822
35.0	0.8929463	0.9999633	0.0009295
40.0	0.8929694	0.9999891	0.0003199
45.0	0.8929764	0.9999970	0.0001095
50.0	0.8929786	0.9999994	0.0000373

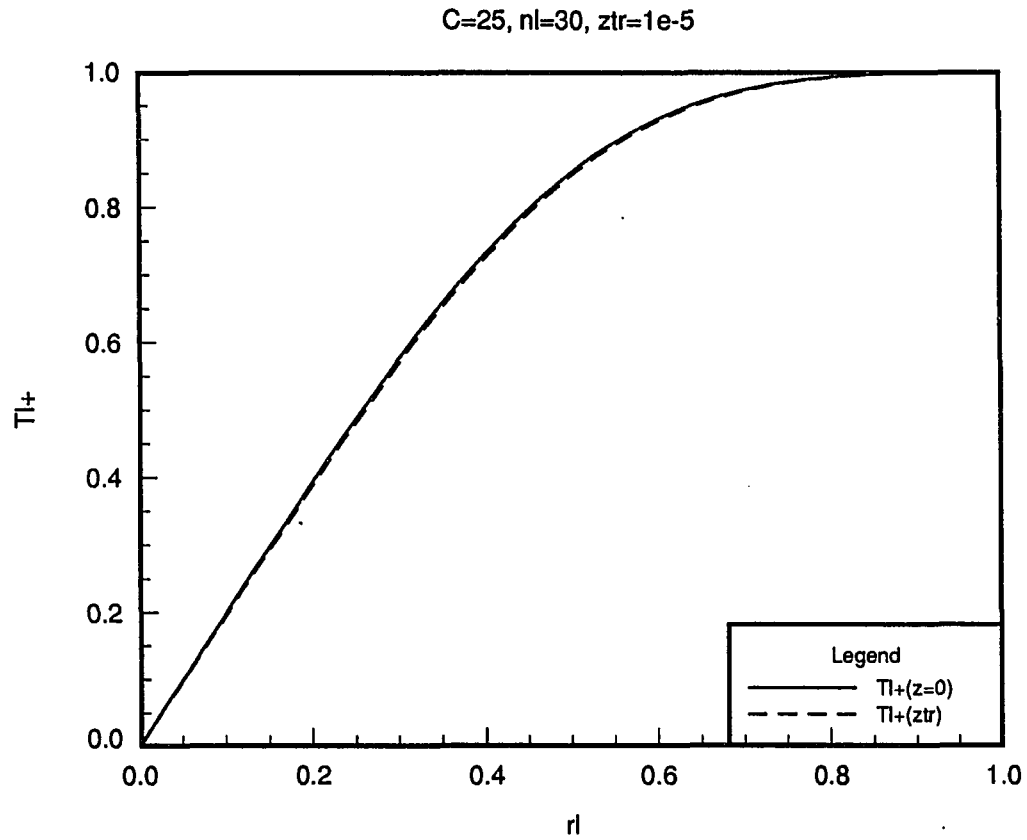


Figure A.3: Dimensionless liquid temperature profile in the boundary layer as $z \rightarrow 0$

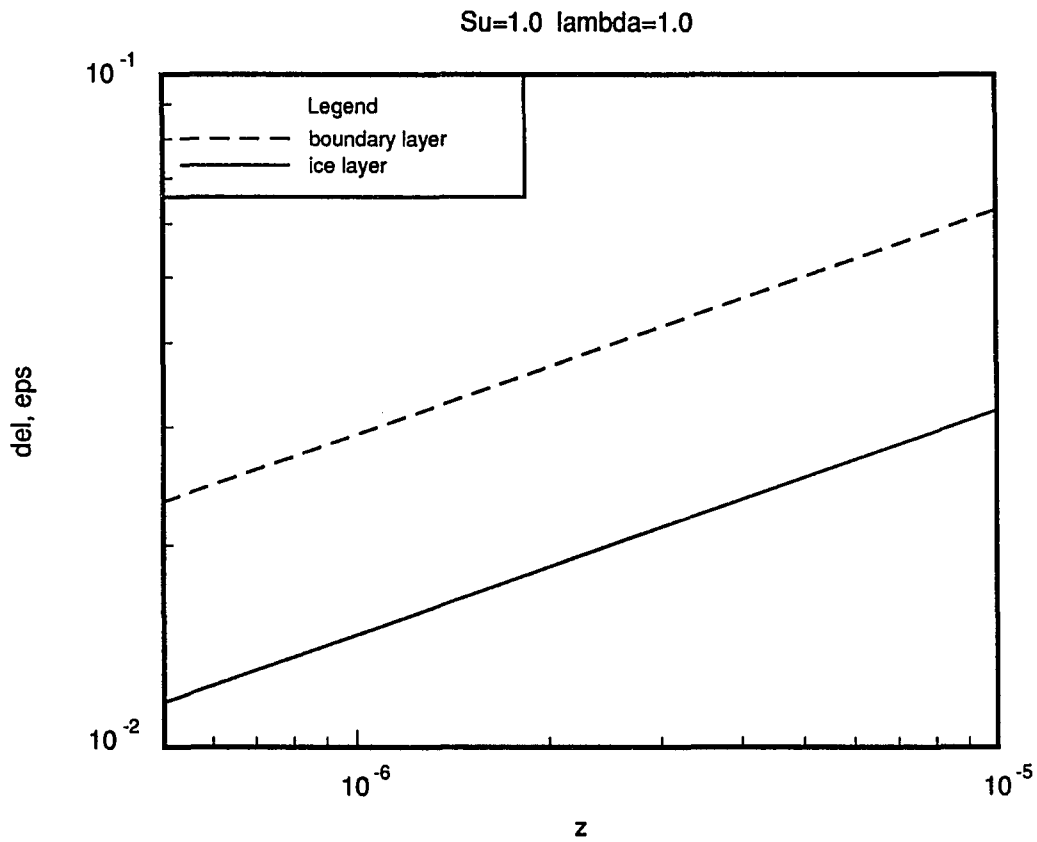


Figure A.4: Asymptotic growth of the thermal boundary layer and ice layer in the axial direction for small z

A.3.2.5 Nusselt number The local Nusselt number can be given as

$$Nu_z = \frac{h_z (2\bar{R})}{k_l} \quad (\text{A.62})$$

The local heat convection coefficient h_z is defined by

$$q_z = h_z (\bar{T}_m - T_o) = -k \left. \frac{\partial \bar{T}_l}{\partial \bar{r}} \right|_{\bar{r}=\bar{R}} \quad (\text{A.63})$$

where q_z is the local heat flux at the solid-liquid interface. Combining Equations (A.62) and (A.63) yields

$$Nu_z = \frac{-2\bar{R}}{(\bar{T}_m - T_o)} \left. \frac{\partial \bar{T}_l}{\partial \bar{r}} \right|_{\bar{r}=\bar{R}}$$

Nondimensionalization results in

$$Nu_z = \frac{2}{\delta T_m} \left. \frac{\partial T_l}{\partial r_b} \right|_{r_b=0} \quad (\text{A.64})$$

where T_m is the dimensionless bulk mean temperature and is given by

$$T_m = \frac{\bar{T}_m - T_o}{T_{io} - T_o}$$

Here the bulk mean temperature is defined as

$$\bar{T}_m = \frac{1}{Q} \int_A \bar{w} \bar{T}_l dA = \frac{1}{Q_{bl}} \int_{bl} \bar{w} \bar{T}_l dA + \frac{1}{Q_{co}} \int_{co} \bar{w} \bar{T}_l dA$$

where Q is the volume flow rate. The subscripts bl and co represent boundary layer and core regions, respectively. Introducing the dimensionless bulk mean temperature and evaluating the integrals, by using the parabolic velocity distribution and $T_l = 1$ in the core, gives

$$\frac{1}{Q_{bl}} \int_{bl} \bar{w} \bar{T}_l dA = 4\delta^2 \int_0^1 T(2 - \delta r_b)(1 - \delta r_b) r_b dr_b$$

and

$$\frac{1}{Q_{co}} \int_{co} \bar{w} \bar{T}_l dA = (1 - \delta)^2 (1 + 2\delta - \delta^2).$$

As $z \rightarrow 0$, the boundary layer thickness shrinks to zero and the integral for the boundary layer region vanishes. The integral for the core region becomes 1 as $\delta \rightarrow 0$. Physically the liquid temperature within the core region is at the uniform inlet temperature, T_{i0} . Then $T_m \rightarrow 1$ as $z \rightarrow 0$.

The analytical asymptotic Nusselt number at $z = 0^+$ becomes

$$Nu_z^+ = \lim_{z \rightarrow 0} Nu_z = \frac{2}{\delta} \left. \frac{\partial T_{la}^+}{\partial r_b} \right|_{r_b=0} = 2(0.678299 z^{-\frac{1}{3}})$$

or

$$Nu_z^+ = 1.356598 z^{-\frac{1}{3}} \quad (\text{A.65})$$

The mean Nusselt number is expressed as

$$Nu_m = \frac{1}{z} \int_0^z Nu_x dx \quad (\text{A.66})$$

and

$$Nu_m^+ = \lim_{z \rightarrow 0} Nu_m = \frac{3}{2} Nu_z^+$$

or

$$Nu_m^+ = 2.034897 z^{-\frac{1}{3}} \quad (\text{A.67})$$

Equations (A.65) and (A.67) give asymptotic results for local Nusselt number and mean Nusselt number as $z \rightarrow 0$.

A.3.3 Numerical solution

A.3.3.1 For small z Despite the existence of the analytical asymptotic solution for small z (determined in Section A.3.2), what is really needed in the transient

calculation is a numerical solution of the initial condition. Otherwise truncation errors will cause spurious transients, as discussed in the fully developed flow initial condition. For small z , a numerical solution is computed by first solving the Graetz problem, given by Equations (A.52), (A.53) and (A.57), for the liquid temperature distribution. Then the solid temperature and ice layer thickness are obtained by solving Equations (A.42), (A.43) and (A.47) using the previously calculated liquid temperature. Stream function and vorticity equations are solved in core scale coordinates to give the initial conditions to the large z solution. The small z solution is obtained for a number of axial nodes by marching up to $z = z_{tr}$, at which point the solution becomes the initial condition to large z solution.

A.3.3.2 For large z Liquid temperature for small z has been solved in boundary layer coordinates and the initial condition to large z solution is required in core coordinates. Therefore interpolation of liquid temperature is necessary at the new grid points, for which Lagrangian interpolation scheme is used. Up to $z = z_{tr}$, thermal boundary layer has grown up to the same order of magnitude as the radius of the pipe, but it is still relatively thin. In order to resolve high liquid temperature gradient near the solid-liquid interface, the stretching of the core radial coordinate is favored. The radial stretching transformation has been discussed in Chapter 3.

The large z solution starts from the initial condition at $z = z_{tr}$, given by small z solution. Because of the effect of the growing ice layer on the hydrodynamic and thermal fields, all five governing equations, Equations (A.6) - (A.10), must be solved simultaneously. The numerical method presented in Chapter 3 is used to solve these equations for the initial conditions of the dependent variables for the developing flow.

Figure A.5 shows the interpolation of liquid temperature from boundary layer scale to core scale coordinate using the Lagrangian interpolation scheme. $nr = 40$ and $\beta = 1.5$ have been used for this plot. Symbols x and o indicate the grid points for the core scale and boundary layer scale coordinates, respectively. The Lagrangian method gives very good interpolation in general, however, the derivative at the solid-liquid interface does not match very well with that in boundary scale. This discrepancy affects the energy balance at $z = z_{tr}$, which can cause spurious transients. Therefore, an adjustment is made at the node (core scale) next to the interface. The liquid temperature value at that node is assigned to match the energy balance exactly, and only the boundary layer scale nodes excluding those within the first core node are used in the interpolation. It was also found that because of the stretching near the interface the first-order accurate derivative was better than the second-order one. This is similar to the fact that the first-order accurate derivative gave better result for the vorticity at the interface (see Section 3.3).

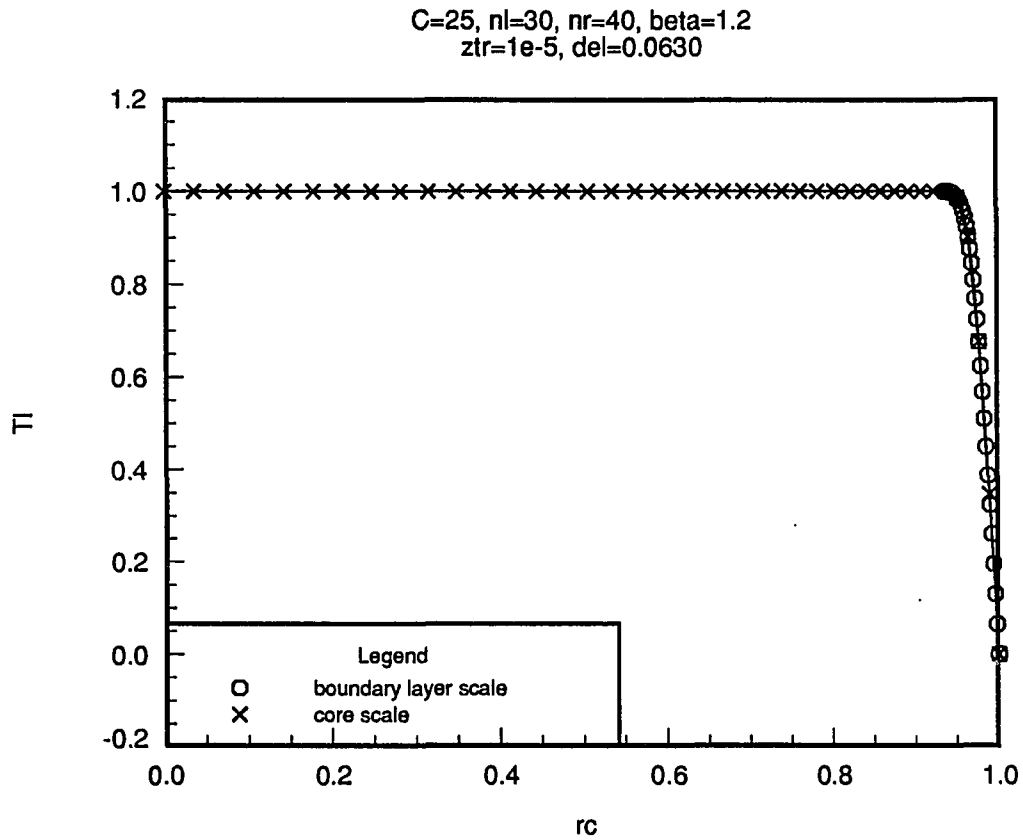


Figure A.5: Lagrangian interpolation of the liquid temperature from boundary layer scale to core scale

APPENDIX B. TRANSFORMATION OF COORDINATES

In general, when a physical space $(\bar{x}_1, \bar{x}_2, \bar{x}_3)$ is mapped into a transformed space (x_1, x_2, x_3) , any partial derivative of the dependent variable $\phi (= \bar{f}, \bar{\omega}, \bar{T}_l, \bar{T}_s, \bar{R})$ in physical coordinates can be determined in terms of transformed coordinates by using the chain rule. Assuming that $\phi = \phi(x_1, x_2, x_3)$, the application of the chain rule results in:

$$\frac{\partial \phi}{\partial \bar{x}_k} = \frac{\partial \phi}{\partial x_1} \frac{\partial x_1}{\partial \bar{x}_k} + \frac{\partial \phi}{\partial x_2} \frac{\partial x_2}{\partial \bar{x}_k} + \frac{\partial \phi}{\partial x_3} \frac{\partial x_3}{\partial \bar{x}_k} \quad (\text{B.1})$$

where $k = 1, 2$ or 3 .

The Jacobian of the transformation is defined as:

$$J = \frac{\partial x_l}{\partial \bar{x}_k} = \begin{bmatrix} \frac{\partial x_1}{\partial \bar{x}_1} & \frac{\partial x_1}{\partial \bar{x}_2} & \frac{\partial x_1}{\partial \bar{x}_3} \\ \frac{\partial x_2}{\partial \bar{x}_1} & \frac{\partial x_2}{\partial \bar{x}_2} & \frac{\partial x_2}{\partial \bar{x}_3} \\ \frac{\partial x_3}{\partial \bar{x}_1} & \frac{\partial x_3}{\partial \bar{x}_2} & \frac{\partial x_3}{\partial \bar{x}_3} \end{bmatrix}$$

With the derivatives in the above Jacobian determined, the transformation of any derivative is readily computed using Equation (B.1). The transformed derivative is in general a combination of partial derivatives in transformed coordinates. Higher order and combined partial derivatives are determined by repeated applications of the chain rule.

In the present study, the physical domain is divided into two regions: solid phase domain and liquid phase domain. Each domain has radial (\bar{r}), axial (\bar{z}), and time (\bar{t})

coordinates. The transformation of the axial and time coordinates are common and they are:

$$z = \frac{\bar{z}}{aPe} \quad \text{and} \quad t = \frac{\bar{t}}{a^2/\alpha_s}$$

where aPe and a^2/α_s are the characteristic length and time scales, respectively. They are denoted by z_c and t_c respectively in the following sections, for convenience.

The radial coordinate of the liquid phase is transformed in three different ways, whereas that of solid phase is transformed in a single way. They are treated separately in the following sections.

B.1 Coordinates for Solid Phase Domain

The physical space is $(\bar{r}, \bar{z}, \bar{t})$ and the transformed space is (r_s, z, t) , where

$$r_s = \frac{a - \bar{r}}{\bar{\epsilon}} \quad \text{and} \quad \bar{\epsilon} = a - \bar{R} = a\epsilon$$

The Jacobian of the transformation is:

$$J_s = \begin{bmatrix} -\frac{1}{a\epsilon} & -\frac{r_s \epsilon'}{z_c \epsilon} & -\frac{r_s \dot{\epsilon}}{t_c \epsilon} \\ 0 & \frac{1}{z_c} & 0 \\ 0 & 0 & \frac{1}{t_c} \end{bmatrix}$$

The partial derivatives are transformed as:

$$\frac{\partial}{\partial \bar{r}} = -\frac{1}{a\epsilon} \frac{\partial}{\partial r_s}$$

$$\frac{\partial}{\partial \bar{z}} = \frac{1}{z_c} \left(\frac{\partial}{\partial z} - r_s \frac{\epsilon'}{\epsilon} \frac{\partial}{\partial r_s} \right)$$

$$\frac{\partial}{\partial \bar{t}} = \frac{1}{t_c} \left(\frac{\partial}{\partial t} - r_s \frac{\dot{\epsilon}}{\epsilon} \frac{\partial}{\partial r_s} \right)$$

$$\frac{\partial^2}{\partial \bar{r}^2} = \frac{1}{a^2 \epsilon^2} \frac{\partial^2}{\partial r_s^2}$$

$$\begin{aligned} \frac{\partial^2}{\partial \bar{z}^2} &= \frac{\partial}{\partial \bar{z}} \left(\frac{\partial}{\partial \bar{z}} \right) = \frac{1}{z_c} \left(\frac{\partial}{\partial z} - r_s \frac{\epsilon'}{\epsilon} \frac{\partial}{\partial r_s} \right) \left\{ \frac{1}{z_c} \left(\frac{\partial}{\partial z} - r_s \frac{\epsilon'}{\epsilon} \frac{\partial}{\partial r_s} \right) \right\} \\ &= \frac{1}{z_c^2} \left\{ \frac{\partial}{\partial z} \left(\frac{\partial}{\partial z} - r_s \frac{\epsilon'}{\epsilon} \frac{\partial}{\partial r_s} \right) - r_s \frac{\epsilon'}{\epsilon} \frac{\partial}{\partial r_s} \left(\frac{\partial}{\partial z} - r_s \frac{\epsilon'}{\epsilon} \frac{\partial}{\partial r_s} \right) \right\} \\ &= \frac{1}{z_c^2} \left\{ \left(\frac{\partial^2}{\partial z^2} - r_s \frac{\epsilon''}{\epsilon} \frac{\partial}{\partial r_s} + r_s \frac{\epsilon'^2}{\epsilon^2} \frac{\partial}{\partial r_s} - r_s \frac{\epsilon'}{\epsilon} \frac{\partial^2}{\partial z \partial r_s} \right) \right. \\ &\quad \left. - r_s \frac{\epsilon'}{\epsilon} \left(\frac{\partial^2}{\partial r_s \partial z} - \frac{\epsilon'}{\epsilon} \frac{\partial}{\partial r_s} - r_s \frac{\epsilon'}{\epsilon} \frac{\partial^2}{\partial r_s^2} \right) \right\} \\ &= \frac{1}{z_c^2} \left\{ \frac{\partial^2}{\partial z^2} + \left(r_s \frac{\epsilon'}{\epsilon} \right)^2 \frac{\partial^2}{\partial r_s^2} - 2r_s \frac{\epsilon'}{\epsilon} \frac{\partial^2}{\partial r_s \partial z} + 2r_s \left(\frac{\epsilon'}{\epsilon} \right)^2 \frac{\partial}{\partial r_s} - r_s \frac{\epsilon''}{\epsilon} \frac{\partial}{\partial r_s} \right\} \\ &= \frac{1}{z_c^2} \left\{ \frac{\partial^2}{\partial z^2} - \frac{N}{\epsilon^2} \right\} \end{aligned}$$

where

$$-N = (r_s \epsilon')^2 \frac{\partial^2}{\partial r_s^2} - 2r_s \epsilon \epsilon' \frac{\partial^2}{\partial r_s \partial z} + (2\epsilon'^2 - \epsilon \epsilon'') r_s \frac{\partial}{\partial r_s}$$

B.2 Core Scale Coordinates for Liquid Phase Domain

The physical space is $(\bar{r}, \bar{z}, \bar{t})$ and the transformed space is (r_c, z, t) , where

$$r_c = \frac{\bar{r}}{\bar{R}} \quad \text{and} \quad \bar{R} = aR$$

The Jacobian of the transformation is:

$$J_c = \begin{bmatrix} \frac{1}{aR} & \frac{r_c R'}{z_c R} & \frac{r_c \dot{R}}{t_c R} \\ 0 & \frac{1}{z_c} & 0 \\ 0 & 0 & \frac{1}{t_c} \end{bmatrix}$$

The partial derivatives are transformed as:

$$\frac{\partial}{\partial \bar{r}} = \frac{1}{aR} \frac{\partial}{\partial r_c}$$

$$\frac{\partial}{\partial \bar{z}} = \frac{1}{z_c} \left(\frac{\partial}{\partial z} - r_c \frac{R'}{R} \frac{\partial}{\partial r_c} \right)$$

$$\frac{\partial}{\partial \bar{t}} = \frac{1}{t_c} \left(\frac{\partial}{\partial t} - r_c \frac{R'}{R} \frac{\partial}{\partial r_c} \right)$$

$$\frac{\partial^2}{\partial \bar{r}^2} = \frac{1}{a^2 R^2} \frac{\partial^2}{\partial r_c^2}$$

$$\begin{aligned} \frac{\partial^2}{\partial \bar{z}^2} &= \frac{\partial}{\partial \bar{z}} \left(\frac{\partial}{\partial \bar{z}} \right) = \frac{1}{z_c} \left(\frac{\partial}{\partial z} - r_c \frac{R'}{R} \frac{\partial}{\partial r_c} \right) \left\{ \frac{1}{z_c} \left(\frac{\partial}{\partial z} - r_c \frac{R'}{R} \frac{\partial}{\partial r_c} \right) \right\} \\ &= \frac{1}{z_c^2} \left\{ \frac{\partial}{\partial z} \left(\frac{\partial}{\partial z} - r_c \frac{R'}{R} \frac{\partial}{\partial r_c} \right) - r_c \frac{R'}{R} \frac{\partial}{\partial r_c} \left(\frac{\partial}{\partial z} - r_c \frac{R'}{R} \frac{\partial}{\partial r_c} \right) \right\} \\ &= \frac{1}{z_c^2} \left\{ \left(\frac{\partial^2}{\partial z^2} - r_c \frac{R''}{R} \frac{\partial}{\partial r_c} + r_c \frac{R'^2}{R^2} \frac{\partial}{\partial r_c} - r_c \frac{R'}{R} \frac{\partial^2}{\partial z \partial r_c} \right) \right. \\ &\quad \left. - r_c \frac{R'}{R} \left(\frac{\partial^2}{\partial r_c \partial z} - \frac{R'}{R} \frac{\partial}{\partial r_c} - r_c \frac{R'}{R} \frac{\partial^2}{\partial r_c^2} \right) \right\} \\ &= \frac{1}{z_c^2} \left\{ \frac{\partial^2}{\partial z^2} + \left(r_c \frac{R'}{R} \right)^2 \frac{\partial^2}{\partial r_c^2} - 2r_c \frac{R'}{R} \frac{\partial^2}{\partial z \partial r_c} + 2r_c \left(\frac{R'}{R} \right)^2 \frac{\partial}{\partial r_c} - r_c \frac{R''}{R} \frac{\partial}{\partial r_c} \right\} \\ &= \frac{1}{z_c^2} \left\{ \frac{\partial^2}{\partial z^2} - \frac{M}{R^2} \right\} \end{aligned}$$

where

$$-M = (r_c R')^2 \frac{\partial^2}{\partial r_c^2} - 2r_c R R' \frac{\partial^2}{\partial r_c \partial z} + (2R'^2 - R R'') r_c \frac{\partial}{\partial r_c}$$

B.3 Boundary Layer Scale Coordinates for Liquid Phase Domain

The physical space is $(\bar{r}, \bar{z}, \bar{t})$ and the transformed space is (r_b, z, t) , where

$$r_b = \frac{\bar{R} - \bar{r}}{\bar{\delta}} \quad \text{and} \quad \bar{\delta} = \bar{R} \delta = a R \delta = a B$$

Here $(R\delta)$ is defined as $B(z)$ for convenience.

The Jacobian of the transformation is:

$$J_b = \begin{bmatrix} -\frac{1}{aR\delta} & \frac{1}{z_c} \left(\frac{R'}{B} - r_b \frac{B'}{B} \right) & \frac{1}{t_c} \left(\frac{\dot{R}}{B} - r_b \frac{\dot{B}}{B} \right) \\ 0 & \frac{1}{z_c} & 0 \\ 0 & 0 & \frac{1}{t_c} \end{bmatrix}$$

The partial derivatives are transformed, using $S = r_b B - R$, as:

$$\frac{\partial}{\partial \bar{r}} = -\frac{1}{aR\delta} \frac{\partial}{\partial r_b}$$

$$\frac{\partial}{\partial \bar{z}} = \frac{1}{z_c} \left(\frac{\partial}{\partial z} - \frac{S'}{B} \frac{\partial}{\partial r_b} \right)$$

$$\frac{\partial}{\partial t} = \frac{1}{t_c} \left(\frac{\partial}{\partial t} - \frac{\dot{S}}{B} \frac{\partial}{\partial r_b} \right)$$

$$\frac{\partial^2}{\partial \bar{r}^2} = \frac{1}{a^2 R^2 \delta^2} \frac{\partial^2}{\partial r_b^2}$$

$$\begin{aligned} \frac{\partial^2}{\partial \bar{z}^2} &= \frac{\partial}{\partial \bar{z}} \left(\frac{\partial}{\partial \bar{z}} \right) = \frac{\partial}{\partial \bar{z}} \left\{ \frac{1}{z_c} \left(\frac{\partial}{\partial z} - \frac{S'}{B} \frac{\partial}{\partial r_b} \right) \right\} \\ &= \frac{1}{z_c} \left\{ \frac{\partial}{\partial z} \left[\frac{1}{z_c} \left(\frac{\partial}{\partial z} - \frac{S'}{B} \frac{\partial}{\partial r_b} \right) \right] - \frac{S'}{B} \frac{\partial}{\partial r_b} \left[\frac{1}{z_c} \left(\frac{\partial}{\partial z} - \frac{S'}{B} \frac{\partial}{\partial r_b} \right) \right] \right\} \\ &= \frac{1}{z_c^2} \left\{ \frac{\partial^2}{\partial z^2} - \frac{\partial}{\partial z} \left(\frac{S'}{B} \frac{\partial}{\partial r_b} \right) - \frac{S'}{B} \frac{\partial^2}{\partial r_b \partial z} + \frac{S'}{B} \frac{\partial}{\partial r_b} \left(\frac{S'}{B} \frac{\partial}{\partial r_b} \right) \right\} \\ &= \frac{1}{z_c^2} \left\{ \frac{\partial^2}{\partial z^2} - \frac{S''}{B} \frac{\partial}{\partial r_b} + \frac{S' B'}{B^2} \frac{\partial}{\partial r_b} - \frac{S'}{B} \frac{\partial^2}{\partial z \partial r_b} \right. \\ &\quad \left. - \frac{S'}{B} \frac{\partial^2}{\partial r_b \partial z} + \frac{S' B'}{B B} \frac{\partial}{\partial r_b} + \left(\frac{S'}{B} \right)^2 \frac{\partial^2}{\partial r_b^2} \right\} \\ &= \frac{1}{z_c^2} \left\{ \frac{\partial^2}{\partial z^2} + \left(\frac{S'}{B} \right)^2 \frac{\partial^2}{\partial r_b^2} - 2 \frac{S'}{B} \frac{\partial^2}{\partial z \partial r_b} + \left(2 \frac{S' B'}{B^2} - \frac{S''}{B} \right) \frac{\partial}{\partial r_b} \right\} \\ &= \frac{1}{z_c^2} \left\{ \frac{\partial^2}{\partial z^2} - \frac{L}{B^2} \right\} \end{aligned}$$

where

$$-L = (S')^2 \frac{\partial^2}{\partial r_b^2} - 2BS' \frac{\partial^2}{\partial r_b \partial z} + (2B'S' - BS'') \frac{\partial}{\partial r_b}.$$

B.4 Stretched Coordinates for Computational Liquid Domain

This transformation is different from others in that it is from dimensionless core scale coordinates (r_c, z, t) to dimensionless stretched coordinates (r, z, t) for computation. It transforms only the radial coordinate, therefore only radial derivatives are considered here. The axial and temporal derivatives remain unchanged.

The radial transformation and its inverse are:

$$r = \frac{\ln\left(\frac{\beta+r_c}{\beta-r_c}\right)}{\ln\left(\frac{\beta+1}{\beta-1}\right)} \quad \text{and} \quad r_c = \frac{\beta\left(\frac{\beta+1}{\beta-1}\right)^r - \beta}{1 + \left(\frac{\beta+1}{\beta-1}\right)^r}$$

where r is the new stretched radial coordinate and β is the stretching parameter.

The first-order derivative in core scale coordinate is transformed into stretched coordinate, as usual:

$$\frac{\partial}{\partial r_c} = \frac{\partial r}{\partial r_c} \frac{\partial}{\partial r}$$

The second-order derivative is expanded using the chain rule as the following:

$$\begin{aligned} \frac{\partial^2}{\partial r_c^2} &= \frac{\partial}{\partial r_c} \left(\frac{\partial}{\partial r_c} \right) = \frac{\partial r}{\partial r_c} \frac{\partial}{\partial r} \left(\frac{\partial r}{\partial r_c} \frac{\partial}{\partial r} \right) \\ &= \frac{\partial r}{\partial r_c} \cdot \frac{\partial r}{\partial r_c} \cdot \frac{\partial}{\partial r} \left(\frac{\partial}{\partial r} \right) + \frac{\partial r}{\partial r_c} \cdot \frac{\partial}{\partial r} \left(\frac{\partial r}{\partial r_c} \right) \cdot \frac{\partial}{\partial r} \\ &= \left(\frac{\partial r}{\partial r_c} \right)^2 \frac{\partial^2}{\partial r^2} + \frac{\partial}{\partial r_c} \left(\frac{\partial r}{\partial r_c} \right) \cdot \frac{\partial}{\partial r} \\ &= \left(\frac{\partial r}{\partial r_c} \right)^2 \frac{\partial^2}{\partial r^2} + \left(\frac{\partial^2 r}{\partial r_c^2} \right) \frac{\partial}{\partial r} \end{aligned}$$

Here the coefficients $\frac{\partial r}{\partial r_c}$ and $\frac{\partial^2 r}{\partial r_c^2}$ can be calculated as:

$$\frac{\partial r}{\partial r_c} = \frac{2\beta}{(\beta^2 - r_c^2) \ln\left(\frac{\beta+1}{\beta-1}\right)} \quad \text{and} \quad \frac{\partial^2 r}{\partial r_c^2} = \frac{4\beta r_c}{(\beta^2 - r_c^2)^2 \ln\left(\frac{\beta+1}{\beta-1}\right)}$$

Then the radial partial derivatives are transformed as:

$$\frac{\partial}{\partial r_c} = X \frac{\partial}{\partial r} \quad \text{and} \quad \frac{\partial^2}{\partial r_c^2} = X^2 \frac{\partial^2}{\partial r^2} + XY \frac{\partial}{\partial r}$$

where

$$X = \frac{2\beta}{(\beta^2 - r_c^2) \ln\left(\frac{\beta+1}{\beta-1}\right)} \quad \text{and} \quad Y = \frac{2r_c}{(\beta^2 - r_c^2)}$$

APPENDIX C. PRESSURE DROP

Pressure does not appear in the governing equations solved in this study, because stream function and vorticity formulation is employed instead of primitive variables. Nevertheless, the effect of internal freezing in a pipe flow upon pressure drop is of considerable interest in the freezing problem at hand. Therefore, pressure drop is treated separately in this Appendix.

C.1 Dimensional Formulation

The governing equations for pressure, \bar{P} , are the radial and axial momentum equations, Equations (2.2) and (2.3). The pressure drop at steady state is of interest in this study. Therefore, the time derivative terms are dropped and the governing equations are given as:

$$\bar{u} \frac{\partial \bar{u}}{\partial \bar{r}} + \bar{w} \frac{\partial \bar{u}}{\partial \bar{z}} = -\frac{1}{\rho} \frac{\partial \bar{P}}{\partial \bar{r}} + \nu \left(\frac{\partial^2 \bar{u}}{\partial \bar{r}^2} + \frac{1}{\bar{r}} \frac{\partial \bar{u}}{\partial \bar{r}} + \frac{\partial^2 \bar{u}}{\partial \bar{z}^2} - \frac{\bar{u}}{\bar{r}^2} \right) \quad (\text{C.1})$$

$$\bar{u} \frac{\partial \bar{w}}{\partial \bar{r}} + \bar{w} \frac{\partial \bar{w}}{\partial \bar{z}} = -\frac{1}{\rho} \frac{\partial \bar{P}}{\partial \bar{z}} + \nu \left(\frac{\partial^2 \bar{w}}{\partial \bar{r}^2} + \frac{1}{\bar{r}} \frac{\partial \bar{w}}{\partial \bar{r}} + \frac{\partial^2 \bar{w}}{\partial \bar{z}^2} \right) \quad (\text{C.2})$$

where \bar{P} is a function of \bar{r} and \bar{z} . The magnitude of the radial and axial variation can be compared using a scale analysis, as used in Appendix A (see section A.1.2). The scale analysis shows that the radial variation is much smaller than the axial variation

in that

$$\frac{\frac{\partial \bar{P}}{\partial \bar{r}}}{\frac{\partial \bar{P}}{\partial \bar{z}}} \sim \frac{1}{Pe} \ll 0.$$

Therefore, the radial variation is neglected and the pressure is regarded as a function of only the axial location, that is,

$$\bar{P} = \bar{P}(\bar{z}).$$

The pressure at the centerline of the pipe can be chosen as a representative pressure at \bar{z} , for convenience.

C.1.1 Pressure gradient

Equation (C.2) governs the pressure variation in the axial direction. Along the centerline of the pipe, $\bar{r} = 0$;

$$\bar{u} = 0 \quad \text{and} \quad \frac{\partial \bar{w}}{\partial \bar{r}} = 0.$$

Accordingly, Equation (C.2) can be rearranged as

$$\frac{\partial \bar{P}}{\partial \bar{z}} = \mu \left(\frac{\partial^2 \bar{w}}{\partial \bar{r}^2} + \frac{1}{\bar{r}} \frac{\partial \bar{w}}{\partial \bar{r}} + \frac{\partial^2 \bar{w}}{\partial \bar{z}^2} \right) - \rho \bar{w} \frac{\partial \bar{w}}{\partial \bar{z}} \quad (\text{C.3})$$

where the last term in the parenthesis can be shown to be negligible compared to the other two terms by a scale analysis, which gives

$$\frac{\frac{\partial^2 \bar{w}}{\partial \bar{z}^2}}{\frac{\partial^2 \bar{w}}{\partial \bar{r}^2}} \sim \frac{1}{Pe^2} \ll 0.$$

Therefore, Equation (C.3) is reduced to

$$\frac{\partial \bar{P}}{\partial \bar{z}} = \mu \left(\frac{\partial^2 \bar{w}}{\partial \bar{r}^2} + \frac{1}{\bar{r}} \frac{\partial \bar{w}}{\partial \bar{r}} \right) - \rho \bar{w} \frac{\partial \bar{w}}{\partial \bar{z}}. \quad (\text{C.4})$$

Now, the axial velocity can be replaced by a stream function term. From the definition of the stream function, .

$$\bar{w} = \frac{1}{\bar{r}} \frac{\partial \bar{f}}{\partial \bar{r}}. \quad (\text{C.5})$$

Substitution of Equation (C.5) into Equation (C.4) and the use of chain rule results in

$$\frac{\partial \bar{P}}{\partial \bar{z}} = \mu \left\{ \frac{1}{\bar{r}} \frac{\partial^3 \bar{f}}{\partial \bar{r}^3} - \frac{1}{\bar{r}^2} \frac{\partial^2 \bar{f}}{\partial \bar{r}^2} + \frac{1}{\bar{r}^3} \frac{\partial \bar{f}}{\partial \bar{r}} \right\} - \frac{1}{2} \rho \frac{\partial}{\partial \bar{z}} \left[\left(\frac{1}{\bar{r}} \frac{\partial \bar{f}}{\partial \bar{r}} \right)^2 \right]. \quad (\text{C.6})$$

As $\bar{r} \rightarrow 0$, the second term in braces becomes unbounded. Therefore, all three terms in braces must be combined to be evaluated at $\bar{r} = 0$. Upon the successive use of L'Hopital's rule, they are simplified as:

$$\begin{aligned} & \lim_{\bar{r} \rightarrow 0} \left\{ \frac{1}{\bar{r}} \frac{\partial^3 \bar{f}}{\partial \bar{r}^3} - \frac{1}{\bar{r}^2} \frac{\partial^2 \bar{f}}{\partial \bar{r}^2} + \frac{1}{\bar{r}^3} \frac{\partial \bar{f}}{\partial \bar{r}} \right\} \\ &= \lim_{\bar{r} \rightarrow 0} \frac{1}{\bar{r}^3} \left\{ \bar{r}^2 \frac{\partial^3 \bar{f}}{\partial \bar{r}^3} - \bar{r} \frac{\partial^2 \bar{f}}{\partial \bar{r}^2} + \frac{\partial \bar{f}}{\partial \bar{r}} \right\} \\ &= \lim_{\bar{r} \rightarrow 0} \frac{1}{3\bar{r}^2} \left\{ 2\bar{r} \frac{\partial^3 \bar{f}}{\partial \bar{r}^3} + \bar{r}^2 \frac{\partial^4 \bar{f}}{\partial \bar{r}^4} - \frac{\partial^2 \bar{f}}{\partial \bar{r}^2} - \bar{r} \frac{\partial^3 \bar{f}}{\partial \bar{r}^3} + \frac{\partial^2 \bar{f}}{\partial \bar{r}^2} \right\} \\ &= \lim_{\bar{r} \rightarrow 0} \frac{1}{3\bar{r}} \left\{ \frac{\partial^3 \bar{f}}{\partial \bar{r}^3} + \bar{r} \frac{\partial^4 \bar{f}}{\partial \bar{r}^4} \right\} \\ &= \lim_{\bar{r} \rightarrow 0} \frac{1}{3} \left\{ \frac{\partial^4 \bar{f}}{\partial \bar{r}^4} + \frac{\partial^4 \bar{f}}{\partial \bar{r}^4} + \bar{r} \frac{\partial^5 \bar{f}}{\partial \bar{r}^5} \right\} \\ &= \frac{2}{3} \frac{\partial^4 \bar{f}}{\partial \bar{r}^4}. \end{aligned}$$

The axial derivative in Equation (C.6) is also converted, upon the use of L'Hopital's rule, into

$$\lim_{\bar{r} \rightarrow 0} \left\{ \frac{\partial}{\partial \bar{z}} \left[\left(\frac{1}{\bar{r}} \frac{\partial \bar{f}}{\partial \bar{r}} \right)^2 \right] \right\} = \frac{\partial}{\partial \bar{z}} \left\{ \left[\lim_{\bar{r} \rightarrow 0} \left(\frac{1}{\bar{r}} \frac{\partial \bar{f}}{\partial \bar{r}} \right) \right]^2 \right\} = \frac{\partial}{\partial \bar{z}} \left[\left(\frac{\partial^2 \bar{f}}{\partial \bar{r}^2} \right)^2 \right].$$

Finally, Equation (C.6) can be evaluated at $\bar{r} = 0$ as

$$\left. \frac{\partial \bar{P}}{\partial \bar{z}} \right|_{\bar{r}=0} = \mu \left(\frac{2}{3} \frac{\partial^4 \bar{f}}{\partial \bar{r}^4} \right) - \frac{1}{2} \rho \frac{\partial}{\partial \bar{z}} \left[\left(\frac{\partial^2 \bar{f}}{\partial \bar{r}^2} \right)^2 \right]. \quad (\text{C.7})$$

In order to simplify the formulation, the second-order term in parentheses are defined as

$$\bar{F} = \frac{\partial^2 \bar{f}}{\partial \bar{r}^2}. \quad (\text{C.8})$$

Using Equation (C.8), Equation (C.7) can be rewritten as

$$\left. \frac{\partial \bar{P}}{\partial \bar{z}} \right|_{\bar{r}=0} = \frac{2}{3} \mu \frac{\partial^2 \bar{F}}{\partial \bar{r}^2} - \frac{1}{2} \rho \frac{\partial \bar{F}^2}{\partial \bar{z}}. \quad (\text{C.9})$$

Equation (C.9) gives the dimensional pressure gradient and this equation can be integrated to give the dimensional pressure drop.

C.1.2 Pressure drop

Pressure drop between the inlet and arbitrary axial location downstream can be calculated by integrating Equation (C.9) from 0 to \bar{z} . Let $\Delta \bar{P}$ be the pressure drop along the pipe length, $0 \leq \bar{z} \leq \bar{z}_{max}$, then upon integration,

$$\Delta \bar{P} = \bar{P}(0) - \bar{P}(\bar{z}_{max}) = - \int_0^{\bar{z}_{max}} \left\{ \frac{2}{3} \mu \frac{\partial^2 \bar{F}}{\partial \bar{r}^2} - \frac{1}{2} \rho \frac{\partial \bar{F}^2}{\partial \bar{z}} \right\} d\bar{z} \quad (\text{C.10})$$

where $\Delta \bar{P}$ is positive whereas the integral is negative. Equation (C.10) describes the dimensional pressure drop from the inlet to the exit of the pipe. In the present study, all the dependent variables have been nondimensionalized. Accordingly, pressure drop also needs to be nondimensionalized.

C.2 Dimensionless Formulation

The newly defined variable \bar{F} can be nondimensionalized first. From its definition,

$$\bar{F} = \frac{\partial^2 \bar{f}}{\partial \bar{r}^2} = \frac{Ga^4/4\mu}{a^2 R^2} \frac{\partial^2 f}{\partial r_c^2} = \frac{Ga^2}{4\mu} \left(\frac{1}{R^2} \frac{\partial^2 f}{\partial r_c^2} \right). \quad (\text{C.11})$$

Therefore, a dimensionless variable F is defined as

$$F = \frac{\bar{F}}{\frac{Ga^2}{4\mu}} = \frac{1}{R^2} \frac{\partial^2 f}{\partial r_c^2}. \quad (\text{C.12})$$

C.2.1 Pressure gradient

In order to nondimensionalize the pressure drop, let's evaluate the right hand side of Equation (C.9). Using Equation (C.12) and the result of coordinate transformation (see Appendix B), the right hand side of Equation (C.9) can be rewritten as

$$\left. \frac{\partial \bar{P}}{\partial \bar{z}} \right|_{\bar{r}=0} = \frac{2}{3} \mu \frac{Ga^2/4\mu}{a^2 R^2} \frac{\partial^2 F}{\partial r_c^2} - \frac{1}{2} \rho \frac{(Ga^2/4\mu)^2}{aPe} \left(\frac{\partial F^2}{\partial z} - r_c \frac{R'}{R} \frac{\partial F^2}{\partial r_c} \right). \quad (\text{C.13})$$

This equation can be simplified in a few steps using the definitions of dimensionless parameters to become

$$\left. \frac{\partial \bar{P}}{\partial \bar{z}} \right|_{\bar{r}=0} = \frac{1}{8} G \left\{ \left(\frac{4}{3R^2} \frac{\partial^2 F}{\partial r_c^2} + \frac{r_c R'}{Pr R} \frac{\partial F^2}{\partial r_c} \right) - \frac{1}{Pr} \frac{\partial F^2}{\partial z} \right\}. \quad (\text{C.14})$$

The second term in parentheses is zero along the centerline, therefore Equation (C.14) is simplified to

$$\left. \frac{\partial \bar{P}}{\partial \bar{z}} \right|_{\bar{r}=0} = \frac{1}{8} G \left(\frac{4}{3R^2} \frac{\partial^2 F}{\partial r_c^2} - \frac{1}{Pr} \frac{\partial F^2}{\partial z} \right). \quad (\text{C.15})$$

C.2.2 Pressure drop

The dimensional pressure drop is obtained by integrating Equation (C.15) as

$$\Delta\bar{P} = - \int_0^{\bar{z}_{max}} \left\{ \frac{1}{8}G \left(\frac{4}{3R^2} \frac{\partial^2 F}{\partial r_c^2} - \frac{1}{Pr} \frac{\partial F^2}{\partial z} \right) \right\} d\bar{z}. \quad (C.16)$$

Using $\bar{z}_{max} = aPe z_{max}$ and $d\bar{z} = aPe dz$, the right hand side of Equation (C.16) can be written in terms of dimensionless variables as

$$\Delta\bar{P} = - \int_0^{z_{max}} \left\{ \frac{1}{8}G \left(\frac{4}{3R^2} \frac{\partial^2 F}{\partial r_c^2} - \frac{1}{Pr} \frac{\partial F^2}{\partial z} \right) \right\} aPe dz. \quad (C.17)$$

Two terms in parentheses can be integrated separately and the second term is directly integrated to result in

$$\Delta\bar{P} = -\frac{1}{8}GaPe \left\{ \frac{4}{3} \int_0^{z_{max}} \Gamma dz - \frac{1}{Pr} (F^2(z_{max}) - F^2(z=0)) \right\} \quad (C.18)$$

where Γ is defined for convenience as

$$\Gamma = \frac{1}{R^2} \frac{\partial^2 F}{\partial r_c^2}. \quad (C.19)$$

This definition is similar to the form of F in Equation (C.12).

Now, the dimensionless pressure drop may be defined from Equation (C.18) and it is given as

$$\Delta P = \frac{\Delta\bar{P}}{\frac{1}{8}GaPe} = - \left\{ \frac{4}{3} \int_0^{z_{max}} \Gamma dz - \frac{1}{Pr} (F^2(z_{max}) - F^2(z=0)) \right\}. \quad (C.20)$$

C.2.3 Normalized pressure drop

In order to compare the pressure drop in a converging flow passage due to internal freezing directly with that of a Hagen-Poiseuille flow, the pressure drop can

be normalized based on the latter. For a Hagen-Poiseuille flow, pressure gradient is uniform in the axial direction and the pressure drop is calculated simply from

$$\Delta\bar{P} = G \cdot \bar{z}_{max}$$

where G is the uniform pressure gradient when the radius of the flow passage is a . For a *given* mass flow rate, the uniform pressure gradient has been derived as:

$$G = -\frac{\partial\bar{P}}{\partial\bar{z}} = \frac{8\nu\dot{m}}{\pi a^4}.$$

For a proper comparison of two pressure drops, they must be based on the same flow passage radius. When the flow passage radius is \bar{R}^* , which is the average radius of flow passage of the pipe with internal freezing, the uniform pressure gradient of a Hagen-Poiseuille flow is given by

$$G_R = \frac{8\nu\dot{m}}{\pi(\bar{R}^*)^4}$$

where the subscript R denotes that the flow passage radius is \bar{R}^* . Therefore, the pressure drop of a Hagen-Poiseuille flow in a pipe of radius \bar{R}^* is

$$\Delta\bar{P}_{HP} = G_R \cdot \bar{z}_{max} = \frac{G}{R^{*4}} \cdot aPe z_{max} \quad (C.21)$$

where the subscript HP denotes the Hagen-Poiseuille flow.

Now the normalized pressure drop is defined as

$$\Delta P_n = \frac{\Delta\bar{P}}{\Delta\bar{P}_{HP}} = \frac{\Delta P}{\Delta P_{HP}}. \quad (C.22)$$

Substituting $\Delta\bar{P}$ and $\Delta\bar{P}_{HP}$ from Equation (C.18) and (C.21) into Equation (C.22), the normalized pressure drop is given by

$$\Delta P_n = -\frac{1}{8} \frac{R^{*4}}{z_{max}} \left\{ \frac{4}{3} \int_0^{z_{max}} \Gamma dz - \frac{1}{Pr} \left(F^2(z_{max}) - F^2(z=0) \right) \right\}. \quad (C.23)$$

The dimensionless and normalized pressure drops are related by

$$\Delta P_n = \frac{1}{8} \frac{R^{*4}}{z_{max}} \Delta P. \quad (\text{C.24})$$

Equation (C.23) gives the normalized pressure drop upon the integration of Γ . However, Γ has been found to be very sensitive to the truncation error. For the results presented in Chapter 4, therefore, ΔP_n is calculated using Equation (C.20) to determine both ΔP and ΔP_{HP} . This has the effect of eliminating the truncation error in the limit $Su \rightarrow \infty$ (Hagen-Poiseuille flow). Then, the dimensionless pressure drop is inversely calculated from Equation (C.24).

C.2.4 Numerical evaluations

In the evaluations of dimensionless pressure drop or normalized pressure drop, there are only two variables to be calculated: F and Γ . Second-order central differencing is used to calculate the second-order derivatives of both variables. F is evaluated at the centerline using the symmetry as

$$F_0 = \frac{1}{R^2} \frac{\partial^2 f}{\partial r_c^2} = \frac{f_1 - 2f_0 + f_{-1}}{R^2(\Delta r_c)^2} = \frac{2f_1}{R^2(\Delta r_c)^2} \quad (\text{C.25})$$

where f_{-1} is equal to f_1 and f_0 is zero.

Γ can be calculated similarly as

$$\Gamma = \frac{1}{R^2} \frac{\partial^2 F}{\partial r_c^2} = \frac{1}{R^2} \frac{F_1 - 2F_0 + F_{-1}}{(\Delta r_c)^2} = \frac{2(F_1 - F_0)}{R^2(\Delta r_c)^2} \quad (\text{C.26})$$

where F_1 is evaluated using second-order central differencing with $f_0 = 0$ as

$$F_1 = \frac{f_2 - 2f_1}{R^2(\Delta r_c)^2}.$$

The integral appearing in Equations (C.18) and (C.23) is numerically calculated using the trapezoidal rule as

$$\int_0^{z_{max}} \Gamma dz = \frac{\Delta z}{2} \left(\Gamma_0 + 2 \sum_{j=1}^{nz-1} \Gamma_j + \Gamma_{nz} \right)$$

where the subscript j is the index for axial nodes and $nz + 1$ is the number of nodes in the axial direction.